Structure-property Relationships of Dyes as Applied to Dye-Sensitized Solar Cells

Yun Gong

Queens' College, Cambridge

Department of Physics

A dissertation is submitted for the degree of

Doctor of Philosophy at the University of Cambridge

September 2017

ABSTRACT

This work investigates the correlation of structural and photovoltaic properties of dyes used in dye-sensitized solar cells. Experimental methods, including ultraviolet-visible spectroscopy, fluorescence spectroscopy, cyclic voltammetry and electrochemical impedance spectroscopy are employed to study optical and electrochemical properties of dye molecules. Computational methods, including density functional theory and time-dependent density functional theory, are used to validate and predict the optical and electronic properties of dye molecules, in their isolated state and once embedded into a working electrode device environment that comprises a dye···TiO_2 interface.

The results chapters begin with the presentation of a series of quinodimethane dyes that are experimentally validated for their photovoltaic application, and associated computational studies reveal that an inner structural factor - a phenyl ring rotation occurring during the optical excitation process - leads to the competitive photovoltaic device performance of these dyes. Carbazole-based dyes are then systematically studied by computation, especially considering charge transfer paths and binding modes of these dyes on a titania surface. The theoretical models for the basic building block of this chemical family of dyes, known as MK-44, successfully support and

explain structural discoveries from X-ray diffraction and reflectometry that impact of their function. A benzothiadiazole-based dye, RK-1, is then systematically studied by both experimental and computational methods, and the results show that the π-bridge composed of thiophene, benzothiadiazole and benzene rings leads to excellent charge separation; and the rotation of these rings during the optical excitation process may well be consistent with the fluorescence spectrum. Finally, the well-known ruthenium-based dyes are theoretically studied to determine the properties of different ligands connected to the metal core of the complex. Conformations with different NCS ligands are calculated in terms of energy and explain well the corresponding results from X-ray diffraction. Acid-base properties of carboxyl groups connected to pyridine ligands in N3 and N749 are theoretically calculated based on thermodynamics and density functional theory. Implicit and explicit models are both adopted to predict these acid dissociative constant values, which are generally in a good agreement with the reported experimental data. The thesis concludes with conclusions and a future outlook.

DECLARATION

This dissertation is the result of my own work and includes nothing that is the outcome of work done in collaboration, except where specifically indicated in the text. It does not exceed the prescribed limit of 60 000 words.

Yun Gong
September 2017

PUBLICATIONS

1. **Yun Gong**, Jacqueline M. Cole, Hiroaki Ozoe and Takeshi Kawase. Phenyl ring twisting upon excited state formation of quinodimethane dyes enhances their photovoltaic performance in dye-sensitized solar cells. Accepted by ACS Appl. Energy Mater.

2. Jacqueline M. Cole, Kian Sing Low and **Yun Gong**; Discovery of Black Dye Crystal Structure Polymorphs: Implication for Dye Conformational Variation in Dye-Sensitized Solar Cells. *ACS Appl. Mater. Interfaces*, 2015, 7(50), pp 27646-27653.

3. Jacqueline M. Cole, Martin A. Blood-Forsythe, Tze-Chia Lin, Philip Pattison, **Yun Gong,** Álvaro Vázquez-Mayagoitia, Paul G. Waddell, Lei Zhang, Nagatoshi Koumura, and Shogo Mori. Discovery of S···C≡N Intramolecular Bonding in a Thiophenylcyanoacrylate-Based Dye: Realizing Charge Transfer Pathways and Dye···TiO_2 Anchoring Characteristics for Dye-Sensitized Solar Cells. *ACS Appl. Mater. Interfaces*, 2017, 9(31), pp 25952-25961.

4. Jonathan McCree-Grey, Jacqueline M. Cole, Stephen A. Holt, Peter J. Evans and

Yun Gong, Dye···TiO_2 interfacial structure of dye-sensitised solar cell working electrodes buried under a solution of I^-/I_3^- redox electrolyte. *Nanoscale*, 2017, 9, 11793-11805.

ACKNOWLEDGEMENTS

First and foremost, I would like to express my gratitude to my supervisor Prof. Jacqui Cole for her careful guidance and helpful discussion throughout this PhD project. My gratitude to Dr Ulrich Mayer for his responsible revision on this thesis and English writing skills.

Thanks to members of the Molecular Engineering group: Dr Liu Xiaogang and Dr Zhang Lei, who gave me lots of advices on research experiences at the first year, helping me get used to the new environment; Dr Jonathan McCree-Grey, for his corporation on carbazole-based dyes project; Dr Giulio Pepe, for his helpful discussion on calculations; Chen Hao, for his help on experiments and discussion on dye aggregation. And also I would like to say thanks to other members, Tan Yizhou, Zhao Teng, Christopher Ashcroft, Alisha Cramer, Ke Deng, Karim T. Mukaddem, Apoorv Jain, Dr Yang Zhenqing, for all the excellent scientific discussion and providing an enjoyable working environment.

In terms of computation, I would like to acknowledge Dr Alexandra Simperler and Dr Alvaro Vazquez-Mayagoitia for valuable technique support, and the computational resources from UK National Service for Computational Chemistry Software (NSCCS)

for the Gaussian09 and Argonne Leadership Computing Facility (ALCF) for the NWChem 6.6. Thanks also goes to Professor Chu Daping and Chang Xin for their help on the access to the electrochemical impedance spectroscopy. I also thanks Cambridge Oversee Trust for financial support.

Finally, I would like to thank my parents who spare no effort to constantly provide material and emotional support, without whom I cannot finish my PhD project in these four years.

CONTENT

CHAPTER 1

Introduction

1.1 Background

Fossil fuels, such as petroleum, coal, and natural gas, have dominated the energy resource sector for many years. However, these traditional sources of energy encompass drawbacks that cannot be avoided, such as a limited availability and pollution arising from their combustion. Therefore, new resources, preferably clean and renewable, are in high demand in order to reduce the current global dependence on fossil fuels. Among many new energy resources, solar energy is outstanding due to its renewable nature as well as the clean and safe use. However, solar energy is relatively difficult to use directly, and accordingly it is often converted into forms of energy via (i) light-thermal, (ii) light-chemical, and (iii) light-electricity conversion. In the context of light-electricity or 'photovoltaic' conversion, solar cells are the most commonly used and efficient devices.

Silicon-based solar cells, which were initially proposed in the 1950s,[1] represent the most developed and widely used cells, especially for commercial applications. Silicon-based solar cells exhibit meanwhile conversion efficiencies larger than 25%

for monocrystalline silicon, and even some commercial panels show efficiencies larger than 20%.[2] However, due to the high costs that are associated with the preparation of monocrystalline silicon, and the high pollution caused during the process of refining silicon, monocrystalline silicon is a less than perfect choice for a large-scale use, and it is, unless the aforementioned issues are resolved, not a suitable substitute for fossil fuels. Therefore, other silicon materials have been developed for photovoltaic applications, such as polycrystalline silicon solar cells or microcrystalline and amorphous silicon thin film solar cells, which have reached conversion efficiencies of 21.9%, 11.9% and 10.2%, respectively.[3] Simultaneously, new types and structures of solar cells have been developed, including e.g. polyhydric compound thin film solar cells (CdTe, CIGS), multi-junction solar cells, organic solar cells (OSCs), dye-sensitized solar cells (DSSCs), quantum dot solar cells, and perovskite solar cells. All of these exhibit specific advantages, and further research should lead to an improvement of their efficiency and ultimately commercialization.[3]

1.2 Dye-sensitized solar cells (DSSCs): an overview

1.2.1 The development of DSSCs

The earliest research on DSSCs dates back to the 1880s, when the response of dye molecules to light of certain wavelength and other dye-sensitized photo-electrochemical phenomena were gradually discovered.[4] However, until the 1960s, the nature of the dye molecules did not attract much attention. Then, Terenina and Putzeiko reported the sensitization of organic dyes on wide-band-gap semiconductors.[5] In the early 1970s, Tributsch discovered that electrons in dye-sensitized semiconductors could be generated and transferred by light.[6] In an early

study on dye-sensitized semiconductors, the semiconductor electrode used in the experiment was dense and flat, which limited the adsorption of dye molecules, and resulted in photoelectric conversion efficiencies of such cells that were usually < 1%.[7] In the 1990s, Grätzel and co-workers used porous titanium dioxide films, which endowed the sensitized electrodes with a large surface area, a ruthenium-based dye as a sensitizer, and I^-/I^{3-} as the redox pair, to prepare DSSCs. Their device achieved a remarkable conversion efficiency larger than 7%.[8]

In the following decades, research on DSSCs has included synthesizing new materials for every constituent component, optimizing preparation conditions, and establishing theoretical models. Recently, DSSCs conversion efficiencies greater than 13% have been accomplished.[9] Taking their relatively low production costs and their low environmental impact into account, DSSCs may represent a viable alternative to replace both fossil fuels and silicon-based solar cells on a large commercial scale.

1.2.2 The working principles of DSSCs

DSSCs consist of the following components (Figure 1.3a): a photoanode (the dye-sensitized porous films of the semiconductor), the electrolyte (solvent with a redox couple), and a counter electrode (thin films with different catalyst materials).
The working principles of DSSCs include the following physical and chemical processes: (i) absorption of photons, (ii) photo-generation of carriers, (iii) separation of photo-induced electron-hole pairs, (iv) transportation and recombination of carriers, and (v) collection of carriers from the external circuit.

In contrast to traditional P-N junction solar cells, the photo-generation and transmission of carriers may occur in different places within the DSSCs. Photo-generated carriers are obtained from the initial absorption of light by the dye molecules, and populate the excited energy levels of the dye molecules, before they are transferred to the conduction band (CB) of the semiconductor.

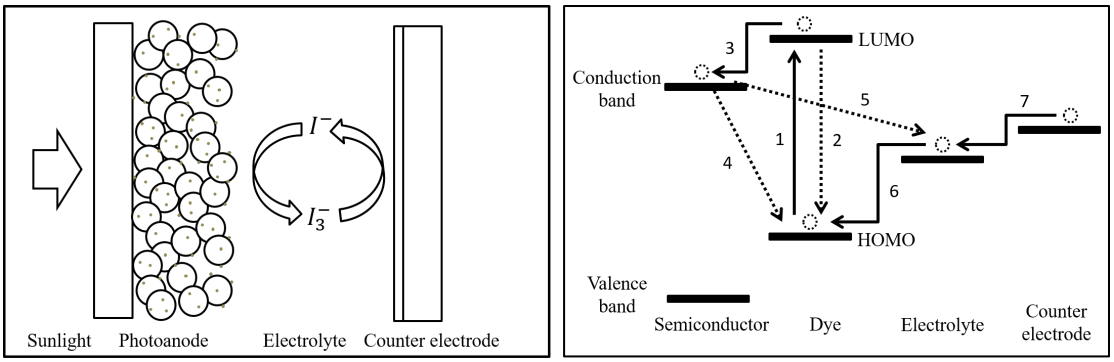

(a) **(b)**

Figure 1.1. (a) Schematic structure of DSSCs. **(b)** Schematic working principle of DSSCs.

Figure 1.1(b) shows the working process in DSSCs in terms of the energy levels of electrons in all components of the DSSC, as well as the complete working cycle in a DSSC. Initially, the electrons in the highest occupied molecular orbital (HOMO) of the dye molecules absorb a dye-specific range of wavelengths of the sunlight spectrum. Sufficient energy provided, the electrons are promoted into the lowest unoccupied molecular orbital (LUMO) (process 1). Subsequently, these excited electrons are injected into the CB of the semiconductor, a process that probably occurs on the femtosecond time scale (process 3).[13] Electrons in the LUMO may also return to the ground state (process 2), but this process occurs on the nanosecond time scale (20-60 ns).[10] As process 2 is several orders of magnitude slower than process 3,

it is feasible to assume a virtually quantitative injection of excited electrons from the LUMO of the dye molecules to the CB of the semiconductor. The electrons that are injected from the LUMO of the dye to the CB of the semiconductor are collected by the conductive glass and subsequently fed into the external circuit by diffusion. Some electrons in the CB may return to the ground state (process 4), or change the oxidation state of redox electrolyte (process 5), whereby the time scale of both processes is comparable to the rate of transmitting electrons to the external circuit. The efficiency of the exportation of electrons is therefore decreased by processes 4 and 5.[10-11] The return of the excited electrons to the HOMO of the dye molecules (process 4), generates holes in the LUMO, which leads to an oxidation of the redox electrolyte (process 6). The redox electrolyte can also be reduced by electrons from the external circuit (process 7) at the interface of the counter electrode, which catalyzes the reduction.

The following reaction equations describe the aforementioned processes and indicate their individual time scales (I^-/I^{3-} is treated as a redox pair):[10-11]

Process 1: Light-induced excitation of electrons (HOMO→LUMO).

$$TiO_2|dye^o + h\nu \rightarrow TiO_2|dye^* \qquad (10^{-15}\ s)$$

Process 2: De-excitation of dye molecules.

$$dye^* \rightarrow dye^o \qquad (10^{-8}\ s)$$

Process 3: Injection of electrons into the CB of the semiconductor.

$$TiO_2|dye^* \rightarrow TiO_2|dye^+ + e^- \qquad (10^{-13}\text{-}10^{-11}\ s)$$

Process 4: Recombination of electrons from the CB of TiO_2 to the HOMO of the dye.

$$TiO_2|dye^+ + e^- \rightarrow TiO_2|dye^o \qquad (10^{-4}\ s)$$

Process 5: Recombination of electrons from the CB of TiO_2 to the electrolyte (I^{3-}).

$$I_3^- + 2\ e^- \rightarrow 3\ I^- \qquad (10^{-2}\ s)$$

Process 6: Reduction of the dye molecules by the electrolyte (I^-).

$$TiO_2|dye^+ + 3\ I^- \rightarrow TiO_2|dye^o + I_3^- \qquad (10^{-6}\text{-}10^{-5}\ s)$$

Process 7: Reduction of the electrolyte (I^{3-}) by electrons from the external circuit.[12]

$$I_3^- + 2\ e^- \rightarrow 3\ I^- \qquad (10^{-10}\ s)$$

1.2.3 Evaluation parameters for the performance of DSSCs

In order to compare and evaluate performances of different solar cells, all parameters should be measured under identical test conditions. Therefore, international standard test conditions have been defined as air mass (AM) 1.5, i.e., 100 mW/cm^2 at 25 °C.

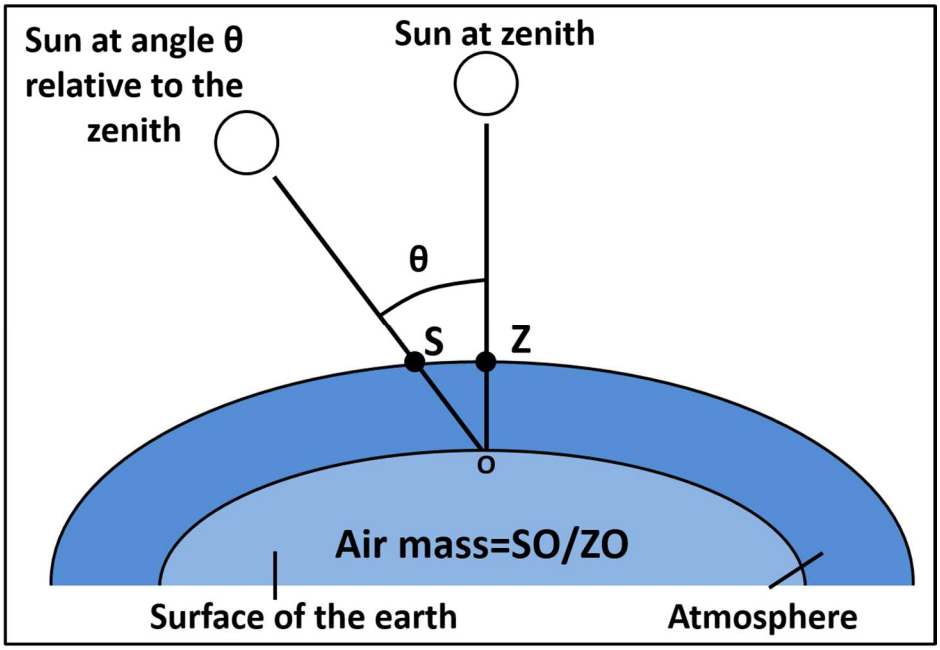

Figure 1.2. Geometric scheme to calculate the air mass (AM).

In Figure 1.2 illustrates the geometric basis for AM1.5: the line ZO, which is perpendicular to sea level, is defined as AM1.0. When the incident angle of the sunlight includes an angle θ relative to ZO (line SO), the corresponding AM equals SO / ZO. For example, AM = 1.5 for θ = 48.2°, which is written as AM1.5. According to the *American Society for Testing and Materials*, in the solar irradiation spectrum under AM1.5, the energy density of the sunlight in the wavelength range 280-4000 nm is 1000.4 W/m^2. To facilitate the calculations and unity, AM1.5 irradiation intensity is defined as 1000 W/m^2 or 100 mW/cm^2, and used as the standard for solar light intensity measurements.

The photovoltaic performance of solar cells is generally characterized by five main parameters: (1) the short-circuit photocurrent density (J_{SC}), (2) the open-circuit photovoltage (V_{OC},), (3) the fill factor (FF), (4) the photoelectric conversion efficiency (PCE; η), and (5) the incident-photon-to-current conversion efficiency (IPCE).

(1) The J_{SC} (mA/cm^2) refers to the current when the solar cell is in the short-circuit state under sun light.

(2) The V_{OC} (mV) refers to the voltage when the solar cell is in the open-circuit state under sun light.

(3) The FF is defined by:

$$FF = \frac{P_m}{J_{SC} \times V_{OC}} \qquad \text{(eq 1.1)}$$

wherein P_m is the maximum working power of the solar cell.

(4) The PCE is defined by:

$$\eta = \frac{P_m}{P_n} = \frac{J_{SC} \times V_{OC} \times FF}{P_n} \quad \text{(eq 1.2)}$$

wherein P_n is the incident power.

(5) The IPCE refers to the ratio between the electron output of the external circuit and the photons that the incident monochromatic light (wavelength λ) radiates to the cell surface. This ratio is sometimes also defined as the external quantum efficiency.

$$IPCE = \frac{N_e(\lambda)}{N_p(\lambda)} = \frac{1.25 \times J_{SC}(mA/cm2)}{\lambda(nm) \times P_{in}(mW/cm2)} \quad \text{(eq 1.3)}$$

wherein N_e is the number of electrons for the output of the external circuit, N_p the number of photons that the incident light radiates, and P_{in} the incident light intensity.

In DSSCs, the IPCE can be understood as a product of the light-harvesting efficiency (LHE; λ), i.e., the efficiency of the absorption of photons by sensitizer, the electron-injection efficiency (Φ_{inj}), i.e., the efficiency of injection of electrons from the sensitizer to the CB of the semiconductor, and the electron-collection efficiency (η_{EC}), i.e., the efficiency of the collection of electrons by the conductive substrate. Furthermore, the product of Φ_{inj} and η_{EC} can be defined as the electron-transfer rate ($\Phi(\lambda)_{ET}$):

$$IPCE = LHE(\lambda) \times \Phi_{inj} \times \eta_{EC} = LHE(\lambda) \times \Phi(\lambda)_{ET} \quad \text{(eq 1.4)}$$

1.3 Metal-free dyes

1.3.1 Principal properties required for DSSC dyes

As the engine of the DSSCs, the dye molecules are required to exhibit several properties that should facilitate a good device performance for practical usage: (1) the absorption spectrum of the dye should be similar to the solar spectrum, and as broad as possible to cover at least the UV-visible region and part of the near-infrared region

(NIR); (2) the electronic energy level of the LUMO of the dye molecule should be higher than that of the CB of the n-type semiconductor so that the photon-excited electron can be injected into the semiconductor; (3) the electronic energy level of the HOMO of the dye molecule should be lower than that of the redox potential of the electrolyte so that the oxidized dye molecule can be regenerated; (4) the injection rate of electrons from the LUMO to the n-type semiconductor must be greater than the sum of the recombination rate of the electrons from the n-type semiconductor to the HOMO and the dye molecule de-excitation rate; (5) the structure of the dye molecule should contain anchoring groups, e.g. carboxyl (-COOH), sulfonate ($-SO_3H$), phosphonate ($-PO_3H_2$), or pyridyl ($-C_5H_4N$) groups in order to promote strong adsorption and efficient electron injection between the dye molecule and the surface of the n-type semiconductor; (6) the structure of the dye molecule should contain a bulky molecular fragment, such as a phenyl or a long alkyl group in order to avoid aggregation on the surface of the n-type semiconductors; (7) the dye should exhibit good photochemical, electrochemical, and thermal stability to retain the performance of the DSSC devices under testing and working conditions.

1.3.2 Structures of metal-free dyes in DSSCs

Currently, the most widely employed dyes in DSSCs contain metals, and especially Ru-based chromophores, such as **N719**, **N3**, and **N749** (Black Dye) can easily obtain conversion efficiency values of 7-11%.[13] In this context, it should be noted that **N719** is currently regarded as the industry standard[9a, 14] and as a benchmark for conversion efficiency ($\eta_{\mathbf{N719}}$ = 10%).[13b] However, a recent study has demonstrated that Zn-based porphyrin sensitizers (Figure 1.5) exhibit conversion efficiency values of up to 13%.[9a]

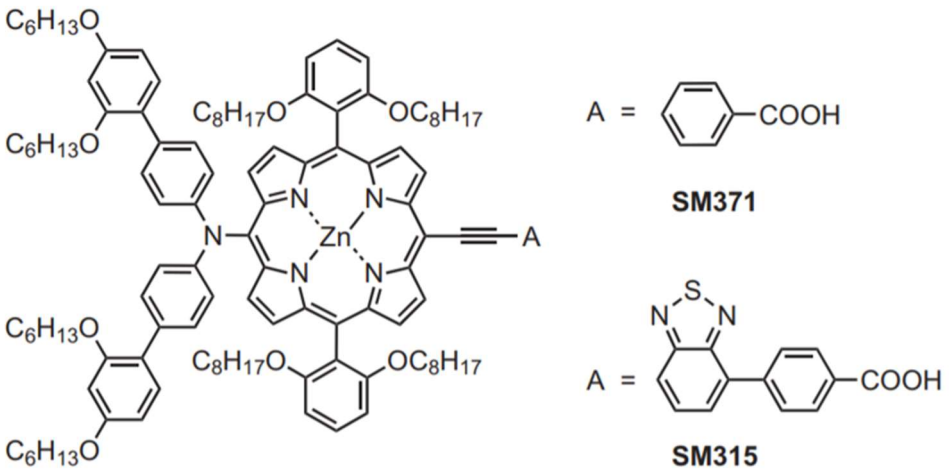

Figure 1.3. Chemical structures of the porphyrin sensitizers **SM371** (η = 12%) and **SM315** (η = 13%).[9a]

An intrinsic drawback of sensitizers based on late transition metals such as ruthenium is that they usually are expensive and that their availability is limited. In general, metal-based dyes are also limited by their complex purification and synthesis, as well as their relatively low molar extinction coefficients. Therefore, organic metal-free dyes have recently received increased attention.

Metal-free dyes are especially attractive with respect to their low cost, structural flexibility, and high molar extinction coefficients.[15] The typical structure of metal-free DSSC dyes contains three constituent components: an electron donor (D), a π-conjugated bridge, and an electron acceptor (A). Under illumination, electrons are excited and transferred from the donor (D) to the acceptor (A) via the π-conjugated bridge (D-π-A-type dyes). Subsequently, the electrons are injected into the n-type semiconductor film as a result of the coupling between the Ti-based 3d orbitals and

the LUMO of the dye molecules.

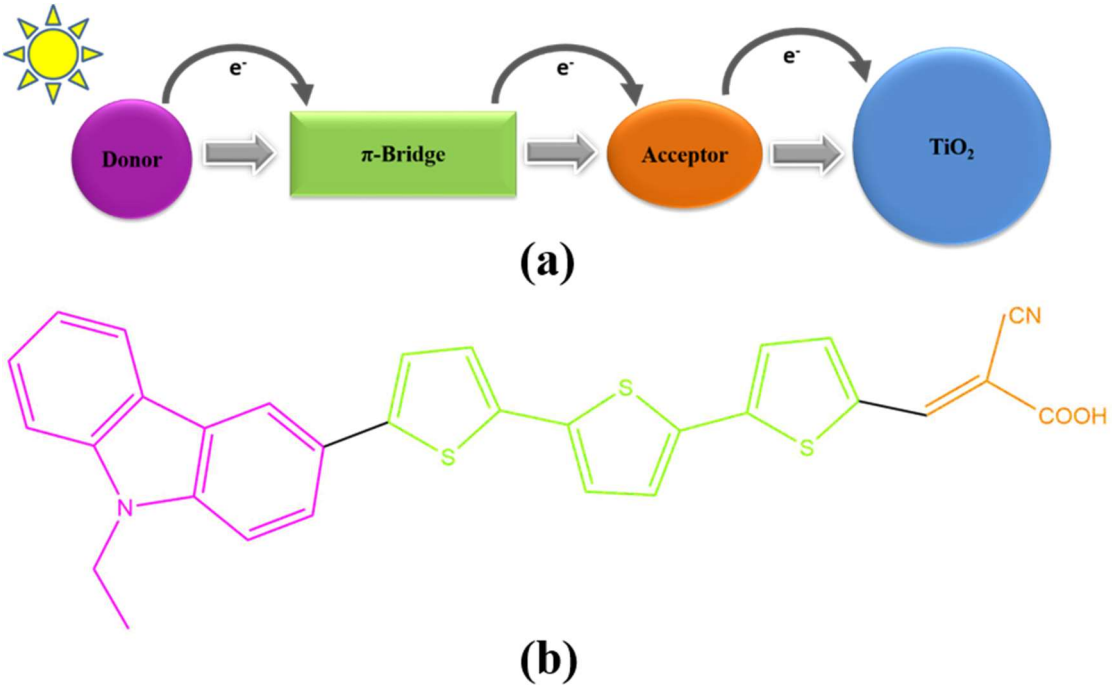

Figure 1.4. (a) Schematic illustration of a generic D-π-A-type dye. **(b)** Chemical structure of carbazole-based dye **MK-3**.[16]

1.3.3 Typical examples of donors, π-conjugated bridges, and acceptors in DSSC dyes

Electron donors (D) not only affect the molecular absorption, but are also responsible for suppressing charge recombination, adjusting energy levels, avoiding aggregation, and maintaining long-term stability.[17] Various organic groups have been used as donors, e.g. fluorine,[18] coumarin,[19] indoline,[20] cyanine,[21] merocyanine,[21] hemicyanine,[22] carbazole,[16] perylene,[23] triarylamine,[24] and xanthene.[25] Among these donor groups, the most commonly employed is triphenylamine (TPA). Dye **Y123**,

which contains a phenyldihexyloxy-substituted TPA (DHO-TPA) as a donor, has been reported by Grätzel *et al.*[24b] and exhibits an device efficiency of 10.3%. This value is so far the highest reported for a metal-free DSSC dye when using a cobalt-based redox pair. Wang *et al.* have reported the substituted TPA dye **C219**, which obtained an efficiency of 10.3% using an iodine/iodide redox shuttle.[24a] The excellent performance of such TPA-based dyes is caused not only by the strong electron-donating properties, but also by the steric demand of the skeleton that successfully suppresses charge-carrier recombination and aggregation.

The π-conjugated bridge should effectively transfer electrons from the donor to the acceptor and facilitate charge separation upon excitation.[26] To further improve the performance of such π-bridges, they can be modified to tune the energy levels of the HOMO and LUMO,[27] enhance the light harvesting,[13a] and comprise both electron-rich (e.g. benzene,[28] fluorene,[29] thiophene,[16] furan,[30] and pyrrole[31]) and electron-deficient (e.g. benzothiadiazole,[32] quinoxaline,[33] benzotriazole,[34] diketopyrrolopyrrole,[35] and 2-thiazole[36]) moieties. One of the most commonly used π-bridge components is thiophene. Hagfeldt *et al.*[27c] have discovered that increasing the number of π-conjugated thiophene units can enhance the spectral response. A systematic study of the light-absorption properties, energy levels, and photovoltaic performance of varying thiophene linkers has been reported by Wang *et al.*[37] Several studies have investigated electron-deficient benzoselenadiazoles,[32, 38] while Lin *et al.* have developed the first example of a benzothiadiazole-containing sensitizer that reached a conversion efficiency of 71% relative to that of a standard DSSC based on **N3**.[38a]

In most cases, the electron acceptor (A) also acts as the anchor, which guarantees a high injection rate and a strong binding between the sensitizer and the semiconductor.[39] Compared to the donor and the π-conjugated bridge, fewer groups are employed as acceptors/anchors. Commonly used acceptors are cyanoacrylic, carboxylic, phosphonic, or sulfonic acid, as well as pyridine.[40] Among these, cyanoacrylic acid is most frequently used, as systematic theoretical and experimental studies on this moiety have demonstrated its excellent injection and low propensity to facilitate recombination.[41]

1.4 Other DSSC components

1.4.1 Photoanode

The photoanode comprises a transparent conductive glass substrate and a dye-sensitized semiconductor film, on which electrons are transferred to the external circuit. Metal oxides, such TiO_2, ZnO, ZrO_2, Al_2O_3, and Nb_2O_5 have been used as materials for such semiconducting films,[42] with TiO_2 being the most commonly used material in this area due to its low cost and environmental compatibility.

Initially, single layers of TiO_2 were used,[7b] but mesoporous films afford significantly improved DSSC conversion efficiencies.[8] As the morphology of the TiO_2 layer does affect the device performance, different dimensional nanostructures have been tested (e.g. nanotubes,[43] nanowires,[44] nanorods,[45] or hierarchical beads[46]) in order to maximize the surface area and increase the conductivity in the direction ofelectron transport.

1.4.2 Electrolyte

The DSSC electrolyte is usually composed of a redox couple, organic solvent, and conductive additive(s). The redox couple plays an important role in transferring electrons from the counter electrode, and in reducing oxidized dye molecules for dye regeneration. The iodide/triiodide (I^-/I_3^-) pair is the most commonly used redox couple in DSSCs, due to its suitable redox potential, rapid dye regeneration, and slow electron recombination properties,[47] and this couple has therefore also been chosen for the experimental work conducted in this thesis. Nevertheless, new redox couples are also constantly investigated in order to match specific dyes. One example for the success of this approach is the previously mentioned cobalt(II/III) redox shuttle, with which a Zn-porphyrin-based DSSC device accomplished a conversion efficiency of 13%.[9a]

1.4.3 Counter electrode (CE)

The counter electrode consists of a catalytic layer on a conductive substrate, such as a transparent conductive oxide glass or a Ti sheet. The function of the counter electrode is to collect the electrons from the external circuit and to catalyze the reduction of the redox pair in the electrolyte. Platinum is the most commonly used and efficient material for this purpose; however, to decrease the device costs, carbon materials have been widely investigated.[48] As the CE is not the focus of the thesis, thermally deposited Pt CEs have been used for all experiments.

1.5 Outline of this thesis

In this thesis, the structure-property relationships of several classes of dyes have

been investigated by experimental and computational means.

Chapter 2 describes the research methods used in this thesis, which include cyclic voltammetry, UV-vis, emission, and electrochemical impedance spectroscopy (experimental), as well as density functional theory (DFT; theoretical).

Chapter 3 discusses a new class of quinodimethene-based dyes, which was investigated by UV-vis and fluorescence spectroscopy, as well as cyclic voltammetry in order to characterize its optical and electrochemical properties. Subsequently, these dyes were used in DSSC devices to validate their potential in photovoltaic applications. DFT calculations were used to theoretically examine the electronic structures of the dyes in different states. The final results showed that in the quinodimethene structure, a rotation of a phenyl ring in the excited state suppresses the electron recombination, which leads to an improved photovoltaic performance.

Chapter 4 is centered on the well-known organic carbazole-based dye **MK-2** and its simpler analogue **MK-44**, which were studied by UV-vis spectroscopy to compare the different binding modes. The results revealed that both **MK-2** and **MK-44** are deprotonated after anchoring onto the TiO_2 surface. Moreover, a change of binding mode for **MK-44** in the presence of lithium ions was investigated by constructing different models to support the results from an X-ray reflectometry study. Furthermore, an additional intramolecular charge-transfer path including an S···CN interaction was experimentally discovered by an X-ray diffraction study, and theoretically supported by DFT calculations.

Chapter 5 is concerned with the highly efficient organic dye **RK1** (η = 10.20%), which was investigated by means of UV-vis and fluorescence spectroscopy to characterize its optical properties in solution and upon adsorption onto TiO_2 films. The binding mode of **RK1** was theoretically examined by DFT calculations, which showed a desirable hypsochromic shift of its excitation, and that the bidentate bridging mode is most stable in terms of adsorption energy.

Chapter 6 discusses computational work performed on **N749** (Black Dye) to compare the energies of varying conformations that differ with respect to the deviation of the NCS ligands from linearity. Subsequently, pK_a values in solution were calculated for **N749** and **N3** by DFT methods using an implicit method. Compared to the experimental results, the implicit method showed good agreement for deprotonated species with low levels of charges, but an increasing discrepancy for charged species that carry high levels of negative charge. Therefore, an explicit-assist method was used for **N3**, and the thus obtained pK_a values exhibited an even smaller deviation from the experimental values for charged species with low levels of charges, albeit that the discrepancy of charged species that carry high levels of negative charge remained.

Chapter 7 contains the conclusions of this thesis and offers an outlook on future work based on the results of this thesis.

Chapter 2

Research Methods

In this chapter, most research methods used in this thesis, including experimental methods such as UV/vis and fluorescence spectroscopy, cyclic voltammetry, and electrochemical impedance spectroscopy, as well as computational methods such as density functional theory (DFT) are introduced, and their background, basic principles, and applications are discussed. The introduction of the quantum theory of atoms in molecules (QTAIM) is introduced in Chapter 4. The theory of computationally calculating and experimentally measuring acid dissociation constants (pK_a) are discussed in Chapter 5. The device fabrication of dye-sensitized solar cells is described in Appendix A.

2.1 UV/vis spectroscopy

UV/vis spectroscopy refers to absorption or reflectance spectroscopy in the UV/vis spectral region (250 – 750 nm), which includes light in the visible, near-UV, and near-IR regions. All UV/vis absorption spectra in this thesis were recorded in absorption mode on a Cary 100 UV-Vis spectrophotometer with 10 nm slits. In this mode, a

monochromatic beam passes through the sample and is then measured by the detector opposite the source of the beam. The absorption spectra are obtained from the recorded initial intensity (I_0), the final intensity (I), and a reference background. The absorbance of the sample is quantitatively described by the Beer-Lambert law:[49]

$$A = \log_{10} \frac{I_0}{I} = \varepsilon \cdot c \cdot L \qquad \text{(eq. 2.1)}$$

where A is the measured absorbance, c the concentration of the absorbing substance, L the path length through the sample, and the ε the molar absorptivity(L mol^{-1} cm^{-1}). The molar absorptivity or extinction coefficient is an important parameter to evaluate absorption properties under specific conditions.

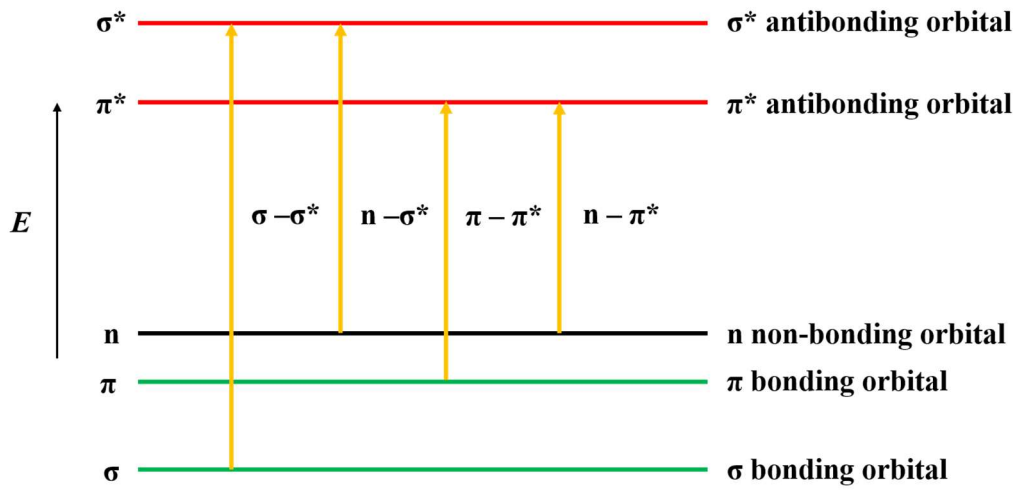

Figure 2.1 Schematic illustration of common types of electronic transitions.

In general, four types of electron transitions can be investigated for organic dyes by UV/vis spectroscopy: σ-σ*, n-σ*, π-π*, and n-π* transitions. Among these, σ-σ* transitions exhibit the highest excitation energy, and their maximum absorption wavelength usually appears at λ_{max} ~ 150 nm, which is at the far end of the UV region and thus almost outside the reach of the UV/vis spectrophotometer. Accordingly, chemicals that exhibit only σ-σ* transitions such as such as *n*-hexane and *n*-heptane

can be used as solvents in UV/vis measurements. Organic molecules that contain heteroatoms such as N, O, S, or halogen atoms often exhibit n-σ* transitions. The excitation energy of the n-σ* transitions is smaller (λ_{max} < 200 nm) than that of the σ-σ* transitions, and these values can be hypsochromically shifted depending on the electronegativity of the heteroatom. Generally, the molar extinction coefficient of this transition is relatively weak (ε ~ 100-300 L mol^{-1} cm^{-1}). Chromophores that contain multiple bonds usually exhibit π-π* transitions (λ_{max} ~ 200 nm; ε ~ 10^4 L mol^{-1} cm^{-1}). In structures with conjugated multiple bonds, the π-π* transition is also called K-band. Due to the conjugation, the π* orbital exhibits increased bonding character, which is commensurate with a lower orbital energy and a bathochromic shift of λ_{max}. The conjugation of multiple bonds also increases the absorption cross section, which in turn increases ε. Organic molecules that contain heteroatoms usually also exhibit n-π* transitions (λ_{max} ~ 200-300 nm). Compared to the transitional probability of π-π* transition, that of n-π* transitions is relatively low, which is reflected in the ε values (~10-100 L mol^{-1} cm^{-1}).

In terms of charge transfer, excitation can be classified by local excitation (LE) and charge-transfer excitation (CT). LE is characterized by the absence of an obvious change of charge distribution after the electron is excited. Given its name, one might easily assume that LE is locally confined; however, that is not the case: for example, if the charge distribution remains almost unchangedover the entire molecular structure before and after the electron excitation, this can also be regarded as LE. In contrast, CT refers to the charge transfer between either different entities in a single molecule (intramolecular charge transfer) or different molecules (intermolecular charge

transfer). For some systems, e.g., transition-metal complexes, LE and CT can be furthermore subdivided, i.e., LE can be classified as a metal-centered transition (MC) or as a ligand-centered transition (LC). Conversely, CT can be classified into metal-to-metal charge transfer (MMCT), ligand-to-ligand charge transfer (LLCT), metal-to-ligand charge transfer (MLCT), and ligand-to-metal charge transfer (LMCT).

In this thesis, UV/vis absorption spectra of various dyes were obtained either in solution or in the solid state upon adsorption onto TiO_2 films on fluorine-doped transparent oxide (FTO) glass. The absorbance data of the solution spectra were normalized using the Beer-Lambert law (*cf.* eq 2.1). For the dyes investigated in this thesis that exhibit π-conjugation, special attention was focused on their π-π* transitions and intramolecular charge transfer (ICT).

2.2 Fluorescence spectroscopy

All fluorescence spectra in this thesis were recorded in emission mode on a Cary Eclipse fluorescence spectrophotometer with a slit width of 20 nm. In this working mode, a monochromatic beam illuminates the sample, which excites the electrons in the sample and causes them to emit light (fluorescence); the intensity of the emitted light is recorded by a detector in all directions. While the excitation light remains at a constant wavelength, the different wavelengths of fluorescent light emitted by the sample are measured (emission spectrum). Fluorescence spectroscopy can furthermore be conducted in two additional modes that are not presented in this thesis: (i) excitation spectra are recorded with a constant emission light by scanning different wavelengths; (ii) emission maps are obtained from recording the emission spectra

caused by a range of excitation wavelengths and combining them with a 3D data set, i.e., the emission intensity as a function of excitation and emission wavelengths.

For the fluorescence, a photon ($h\upsilon_{ex}$) from an external source is absorbed by the sample, forming an excited singlet state (S'_1) that exists for a finite time. During its relaxation time, a conformational change is accompanied by the formation of a new singlet state (S_1) at lower energy. Other processes such as collisional quenching, fluorescence resonance energy transfer (FRET), and intersystem crossing (ISC) may also occur during relaxation. Finally, a photon ($h\upsilon_{em}$) with lower energy than that of the absorbed photon is emitted from S_1 to S_0, and the energy difference $h\upsilon_{ex} - h\upsilon_{em}$ is called the Stokes shift.

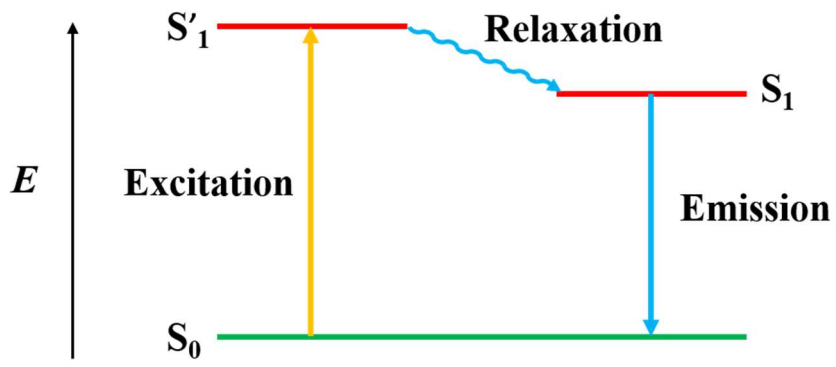

Figure 2.2 Jablonski diagram for the processes involved in the creation of an excited electronic singlet state (S'_1) by optical absorption and the subsequent emission (fluorescence).

In this thesis, the emission spectra of various dyes in solution were recorded. Excitation wavelengths were chosen based on their respective first absorption

wavelength in their UV/vis spectra. All emission data were normalized relative to their respective charge-transfer bands. Combined with the UV/vis spectra, the Stokes shift is an important analytic tool for the examination of the optoelectronic properties of chromophores, given that the Stokes shift is related to the relaxation time, as well as to the reorganization of the geometry of the excited state and the solvent.

2.3 Cyclic voltammetry (CV)

In a typical cyclic voltammetry experiment, the intensity of the working electrode current is recorded by scanning a range of voltages. In this thesis, all cyclic voltammograms were recorded using an Autolab chemical workstation.

The experimental setup is based on the so-called three-electrode setup, which includes a reference electrode [Ag/AgCl; 0.197V vs standard hydrogen electrode (SHE)], working electrode (glassy carbon electrode), counter electrode (platinum sheet), and the electrolyte. The latter consists of the sample to be tested in the solvent of choice ([sample] = 0.05 mM) and 0.1 M [*n*-Bu_4N][ClO_4] as the supporting electrolyte.

The analyte has to be redox active within the experimental potential window in order to record reversible or irreversible wave plots during the voltage scan. Upon increasing the voltage from the starting point (0 V), one electron of the analyte is removed from the highest occupied molecular orbital (HOMO), which is commensurate with an oxidation. Upon reversion the voltage (backward scan), the analyte is reduced again, provided that the oxidized form of the analyte is stable on

the CV time scale. When the initial scan occurs in negative direction, the analyte is reduced, i.e. one electron is deposited into the lowest unoccupied molecular orbital (LUMO) before the thus reduced form of the analyte is oxidized upon reversing the scan.

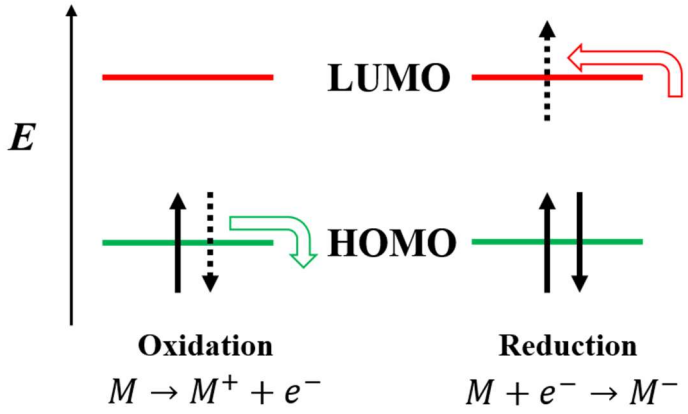

Figure 2.3 Schematic illustration of the oxidation and reduction during CV measurements.

The energy levels of the HOMO and LUMO can be calculated using the following equations:

$$E_{HOMO} = -(E_{ox\ vsAg/AgCl} - E_{Ag/AgCl\ vs\ SHE} - E_{SHE\ vs\ vacuum})\ eV \quad \text{(eq 2.2)}$$

$$E_{LUMO} = -(E_{red\ vsAg/AgCl} - E_{Ag/AgCl\ vs\ SHE} - E_{SHE\ vs\ vacuum})\ eV \quad \text{(eq 2.3)}$$

Where $E_{ox\ vs\ Ag/AgCl}$/$E_{red\ vs\ Ag/AgCl}$ is the onset of the oxidation/reduction peak in the CV curves, and $E_{SHE\ vs\ vacuum}$ = 4.5 V. To get a more precise CV result, the ferrocenium/ferrocene (Fc/Fc^+) redox couple is commonly used as an internal or external standard to calibrate the measurement system, as the oxidation and reduction of Fc/Fc^+ involves a stable single-electron process.[50] In this thesis, Fc/Fc^+ is used as

an external standard and the thus obtained calibration term Δcorrection is introduced into the equations:

$$\Delta\text{correction} = E^{exp}_{Fc/Fc^+} - E^{ref}_{Fc/Fc^+} \quad \text{(eq 2.4)}$$

$$E_{HOMO} = -(E_{ox\ vs.Ag/AgCl} - E_{Ag/AgCl\ vs\ SHE} - E_{SHE\ vs\ vacuum} - \Delta\text{correction})eV \quad \text{(eq 2.5)}$$

$$E_{LUMO} = -(E_{red\ vs.Ag/AgCl} - E_{Ag/AgCl\ vs\ SHE} - E_{SHE\ vs\ vacuum} - \Delta\text{correction})eV \quad \text{(eq 2.6)}$$

where E^{exp}_{Fc/Fc^+} is the average experimentally measured oxidation/reduction potential, while E^{ref}_{Fc/Fc^+} refers to the commonly used reference values of Fc/Fc^+ under specific conditions.

2.4 Electrochemical impedance spectroscopy (EIS)

Electrochemical impedance spectroscopy (EIS) is a powerful electrochemical tool that uses a small alternating current (ac) as a perturbation. For a stable linear system S, an input ac voltage $\hat{V}(\omega)$ is applied at an angular frequency, ω, and the ac response current of the system, $\hat{I}(\omega)$, is recorded by a chemical work station. The impedance is defined by:

$$Z(\omega) = \frac{\hat{V}(\omega)}{\hat{I}(\omega)} \quad \text{(eq 2.7)}$$

where all quantities are complex amplitudes of ac perturbations and the symbol 'hat' refers to a very small perturbation. As Z (ω) is a complex quantity, it can also be expressed by:

$$Z(\omega) = Z'(\omega) + jZ''(\omega) \quad \text{(eq 2.8)}$$

The Nyquist plot, in which the impedance is a vector with its real and imaginary parts chosen as the x- and y-axes, respectively[51], is a predominant method to illustrate impedance. During an impedance measurement, the system is kept at a fixed steady state by imposing stationary constraints such as a specific dc voltage and illumination density, before a small ac voltage is imposed onto the system. *Z(ω)* is then measured by scanning the frequency at a multitude of values, typically ranging from 10 mHz to 100 MHz.

The EIS spectrum of a DSSC may offer information on several important processes including charge transfer, transport, and accumulation:[52]

(i) charge transport may occur by electron diffusion in the TiO_2 film and ionic diffusion in the electrolyte;

(ii) charge transfer may occur by electron recombination at the FTO/electrolyte interface and by recombination at the TiO_2-adsorbed dye/electrolyte interface, and by regeneration of the redox species at the TCO-Pt/electrolyte interface;

(iii) charging of the capacitive elements in the cells including the interfaces, the conduction band, and surface states of the porous TiO_2 film.

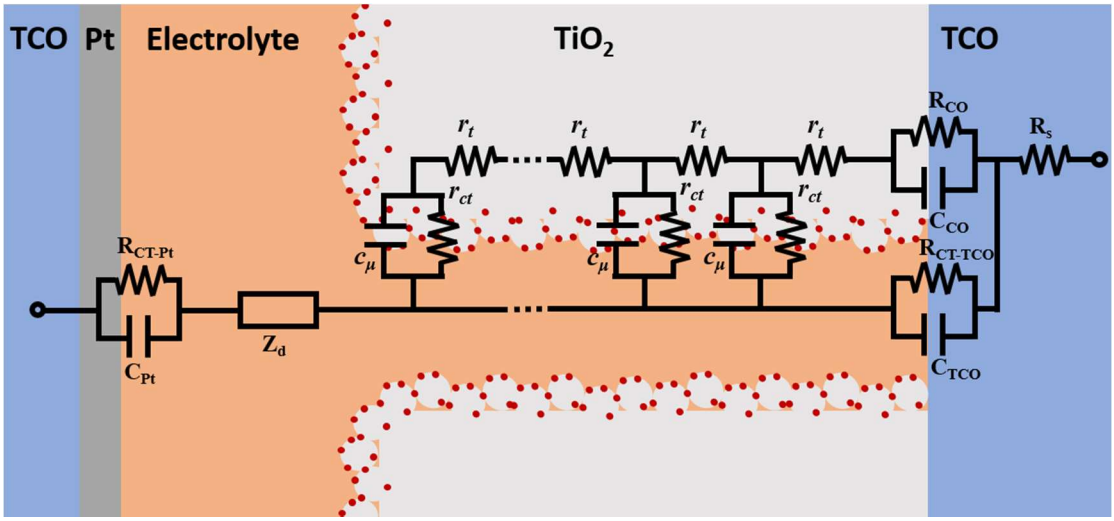

Figure 2.4 The equivalent-circuit diagram of all the components in a DSSC during an electrochemical impedance spectroscopy measurement.[53] All capacitance elements in the circuit are constant-phase elements (CPE).

To simulate the processes that occur in DSSCs during EIS measurements, the use of an equivalent-circuit diagram has been proposed,[53] and electrical elements have been adopted to illustrate the behavior of the DSSC system during the EIS measurements. The pure resistance, R_S, is the resistance of the system. The RC sub-circuit composed of $R_{CT\text{-}TCO}$ and C_{TCO} represents the charge-transfer resistance and double-layer capacitance at the TCO/electrolyte interface; the RC sub-circuit composed of R_{CO} and C_{CO} represents the charge-transfer resistance and capacitance at the TCO/TiO_2 interface; the RC sub-circuit composed of $R_{CT\text{-}Pt}$ and C_{Pt} represents the charge-transfer resistance and double-layer capacitance at the electrolyte/Pt-TCO interface; Z_d is a Warburg element describing Nernst diffusion in the electrolyte; r_t is the resistance of TiO_2 in the film, while r_{ct} and c_μ represent the resistance and capacitance at the surface of each dye/TiO_2 particle and electrolyte, and this part can be simplified to the circuit below:

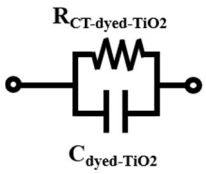

Figure 2.5 A simplified equivalent circuit of the charge-transfer process occurs at the dye-TiO_2/electrolyte interface ($R_{CT\text{-}dyed\text{-}TiO2}$: resistance at the dye-$TiO_2$/electrolyte interface; $C_{dyed\text{-}TiO2}$: capacitance at the dye-TiO_2/electrolyte interface).

Typically, EIS spectra of DSSCs are measured under two constraints, under illumination at a certain intensity or under a forward bias, which is normally the open-circuit voltage (V_{OC}) of the device. For under illumination, the DSSC is in its working state. Compared to the large contact area between the porous TiO_2 film and the electrolyte, the TCO/electrolyte area is relatively small so that the charge transfer should proceed predominantly via the dye-TiO_2/electrolyte pathway and the effect of TCO/electrolyte can be neglected. Furthermore, the impedance of TCO/TiO_2 is very small and its frequency response band overlaps with the impedance of TCO-Pt/electrolyte. Thus, the equivalent circuit under these conditions can be simplified to $R_S(R_{CT\text{-}dyed\text{-}TiO2}\ C_{dyed\text{-}TiO2})\ (R_{TCO\text{-}Pt/electrolyte}\ C_{TCO\text{-}Pt/electrolyte})\ Z_d$, which is shown as follow:

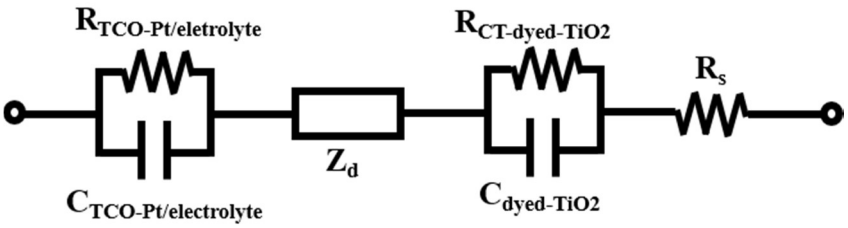

Figure 2.6 A simplified equivalent circuit under illumination.

The Nyquist plot of this model consists of three semicircles. In the high-frequency region, the intercept of the Z' axis is the value of R_S, and the first semicircle in this region represents the impedance of the TCO-Pt/electrolyte interface. The semicircle in the middle represents the recombination process at the dye-TiO_2/electrolyte interface. The last semicircle, which is in the low-frequency region describes the response of the Warburg element, i.e., the ion diffusion in the electrolyte.

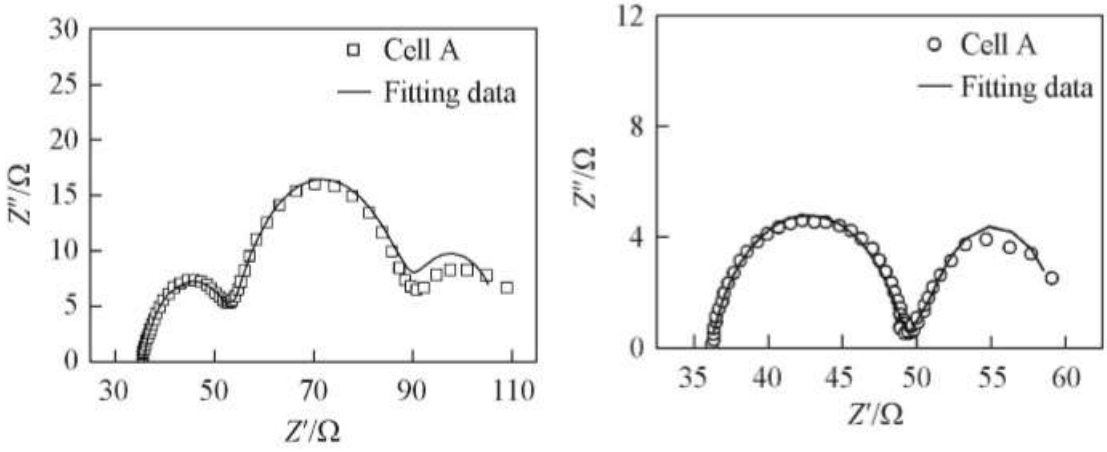

Figure 2.7 Nyquist plots under (a) illumination and (b) forward bias.

As the frequency-response region of the TCO/electrolyte and TCO-Pt/electrolyte are similar, their two semicircles cannot be separated and only one semicircle can be observed in the high-frequency region. As previously mentioned, the semicircle in the low frequency region is the Warburg impedance.

For measurement under a forward bias, the electron will transfer from reduced analyte in the electrolyte to TCO. Since the charge density of TiO_2 film is quite small under the forward bias, the TiO_2 film is almost insulated, the RC sub-circuit of dyed-TiO_2/electrolyte is almost open. Thus, the charge transfer at TCO/electrolyte is the main path way and the whole equivalent circuit can be simplified as R_S ($R_{TCO/electrolyte}$ $C_{TCO/electrolyte}$) ($R_{TCO-Pt/electrolyte}$ $C_{TCO-Pt/electrolyte}$) Z_d :

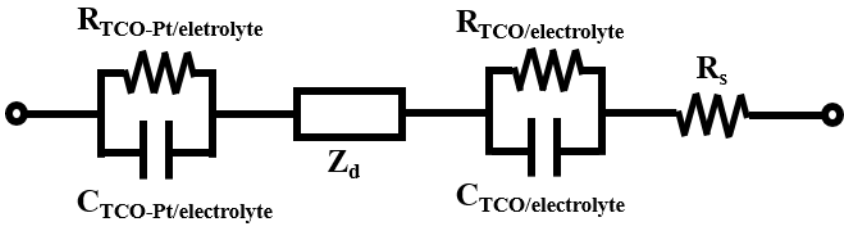

Figure 2.8 Simplified equivalent circuit under forward bias.

As the frequency response region of TCO/electrolyte and TCO-Pt/electrolyte are similar to each other so that their two semicircles cannot be separated and only one semicircle can be observed in the high frequency region. And as mentioned above, the semicircle in the low frequency region is the Warburg impedance.

In this thesis, only EIS spectra under a forward bias were recorded in order to compare different recombination processes of the devices in the dark state.

2.5 Density functional theory (DFT) and time-dependent density functional theory (TDDFT) methods

2.5.1 General considerations for DFT methods

Density Functional Theory (DFT) is a quantum-chemistry method commonly used to investigate properties of electronic structures of many-body systems, especially for atoms, molecules, and solids. The main concept of this theory is based on replacing the electron wavefunction, with 3N coordinates, by functionals of electron density, with only 3 coordinates, to describe an N-electron system. Thus, the computational cost of the calculations can be greatly reduced, while the accuracy of the results is maintained.

The theoretical foundation of DFT, the so-called Hohenberg–Kohn (H-K) theorems, was developed by Hohenberg and Kohn in 1964.[54] The original H-K theorems were concerned exclusively with non-degenerate ground states in the absence of a magnetic field, albeit that more generalized theorems were developed thereafter.[55] The first H-K theorem demonstrates that the ground-state properties of a many-electron system are determined by the electron density. The second H-K theorem defines an energy functional for the system, and proves that the minimum of this energy functional represents the correct electron density of the ground state.

2.5.2 Kohn-Sham (K-S) equation

For practical applications of DFT, Kohn-Sham (K-S) DFT methods are commonly used, which simplify a many-body problem of interacting particles (typically electrons) in a static external potential to a problem of non-interacting particles moving in an effective potential. The latter system is called the K-S system, and has the same density as its corresponding system with interacting particles. [56]

In the K-S system, the wavefunction of particles is a single Slater determinant constructed from a set of orbitals (K-S orbitals) that represent the lowest-energy solutions to:

$$\left(-\frac{\hbar^2}{2m}\nabla^2 + v_{\text{eff}}(\boldsymbol{r})\right) = \varepsilon_i \varphi_i(\boldsymbol{r}) \qquad \text{(eq 2.9)}$$

where ε_i is the orbital energy of the corresponding K-S orbital, φ_i. The density of this N-particle K-S system is defined as:

$$\rho(\boldsymbol{r}) = \sum_i^N |\varphi_i(\boldsymbol{r})|^2 \qquad \text{(eq 2.10)}$$

The effective potential, $v_{\text{eff}}(\mathbf{r})$, in which the non-interacting particles move, is

called K-S potential and expressed as:

$$v_{\text{eff}}(\mathbf{r}) = v_{ext}(\boldsymbol{r}) + e^2 \int \frac{\rho(\boldsymbol{r\prime})}{|\boldsymbol{r}-\boldsymbol{r\prime}|} d\boldsymbol{r}' + \frac{\delta E_{XC}[\rho]}{\delta \rho(\boldsymbol{r})} \qquad \text{(eq 2.11)}$$

where v_{ext} is the external potential acting on the interacting system. For e.g. a molecular system, the external potential should be the electron-nuclei interaction. E_{XC} represents the exchange-correlation energy.

2.5.3 Exchange-correlation functionals

The major problem of the K-S equation is that the exact functional for exchange and correlation is unknown (except for a free electron gas). To circumvent this obstacle, the implementation of some approximations is necessary. One of the most commonly used approximations is the so-called local-density approximation (LDA), in which the exchange-correlation energy depends exclusively on the density:

$$E_{XC}^{LDA}[\rho] = \int \epsilon_{XC}(\rho)\rho(\boldsymbol{r})d\boldsymbol{r} \qquad \text{(eq 2.12)}$$

where ϵ_{XC} is the exchange-correlation energy per particle of a homogeneous electron gas of charge density ρ.

The local-spin-density approximation (LSDA) is a modification of the LDA including the electron spin:

$$E_{XC}^{LSDA}[\rho_\alpha, \rho_\beta] = \int \epsilon_{XC}(\rho_\alpha, \rho_\beta)\rho(\boldsymbol{r})d\boldsymbol{r} \qquad \text{(eq 2.13)}$$

where ρ_α and ρ_β represent the charge density of the corresponding electron spin.

To render these approximations more realistic, i.e., closer to a inhomogeneous system, generalized gradient approximations (GGAs) have been used, and these depend on the gradients of the charge density:[57]

$$E_{XC}^{GGA}[\rho_\alpha, \rho_\beta] = \int \epsilon_{XC}(\rho_\alpha, \rho_\beta, \boldsymbol{\nabla}\rho_\alpha, \boldsymbol{\nabla}\rho_\beta)\rho(\boldsymbol{r})d\boldsymbol{r} \quad \text{(eq 2.14)}$$

Furthermore, hybrid functionals, which represent an approximation that incorporates a fraction of exact exchange from Hartree–Fock theory, have been successfully used to calculate the properties of organic molecules.[58] Commonly used hybrid functionals include the Becke-3-parameters-Lee-Yang-Parr (B3LYP) hybrid functional,[59] the Coulomb-attenuating Becke-3-parameters-Lee-Yang-Parr (CAM-B3LYP) hybrid functional, [60] and the meta hybrid GGA.[61]

2.5.4 Basis sets

In quantum calculations, DFT requires a basis set of functions to represent K-S orbits, whose linear combination ismolecular orbitals. To get a complete set of basis functions, the linear combination of atomic orbitals (LCAO) is used with the K-S orbitals. Slater-type orbitals (STOs)[62] are able to describe the long-range overlap between atoms, as they exponentially decay with distance from the nuclei, albeit with computational difficulty. However, calculations using Gaussian Type Orbits (GTOs)[63] are more convenient, as they can approximate STOs by linear combination. The smallest basis sets, which consist of GTOs with the minimum number of basis functions required to represent all the electrons, are called minimal basis sets. There are also other types of basis sets such as split-valence[64] and correlation-consistent basis sets.[65] To represent atom orbitals more precisely, some additions are used in the basis sets, such as polarization functions (denoted by “*” or “**”) and diffuse functions (denoted by “+” or “++”).

2.5.5 Time-dependent density functional theory (TD-DFT)

TDDFT is an extension of DFT that is used to describe excited states, based on the Runge-Gross (R-G) theorem,[66] which is analogous to the H-K theorem and shows the connection between the time-dependent external potential and time-dependent density in a given system. Furthermore, this non-interacting density can also be described by the time-dependent K-S formalism.[67] In this context, two approaches can be used to study the properties of a given system. When the time-dependent external potential is weak, linear-response theory can be used, while a full solution of the K-S equations is required when the potential is strong. In this thesis, linear-response theory is adopted in all TDDFT calculations.

Chapter 3

Quinodimethane-based Dyes

3.1 Introduction

This chapter contains the results of an experimental and computational investigation on four members of a novel class of organic dyes (**1**-**4**), characterized by a charge-transfer structure based on a quinodimethane backbone (Figure 3.1), which was identified based on a large-scale data-mining method.[68] To further develop the electrochemical properties for potential photovoltaic applications in e.g. dye-sensitized solar cells (DSSCs), different functional groups were connected to the core structure to form D-π-A or D-π-A-π-Ads (D = donor, A = acceptor, Ads = Adsorbing substituent) motifs.

Compound **1**: *(E)-2-cyano-3-(4-((3,5-di-tert-butyl-4-oxocyclohexa2,5-dien-1-ylidene)(4-(dimethylamino)phenyl)methyl)phenyl)acrylic acid*.

Compound **2**: *4-((3,5-di-tert-butyl-4-oxocyclohexa-2,5-dien-1-ylidene)(4-(dimethylamino)phenyl)methyl) benzoic acid*.

Compound **3**: *(E)-2-cyano-3-(4-((3,5-di-tert-butyl-4-oxocyclohexa-2,5-dien-1-ylidene*

(4-(diphenylamino)phenyl)methyl)phenyl)acrylic acid.

Compound **4**: *4-((3,5-di-tertbutyl-4-oxocyclohexa-2,5-dien-1-ylidene)(4-(diphenylamino)phenyl)methyl) benzoic acid*.

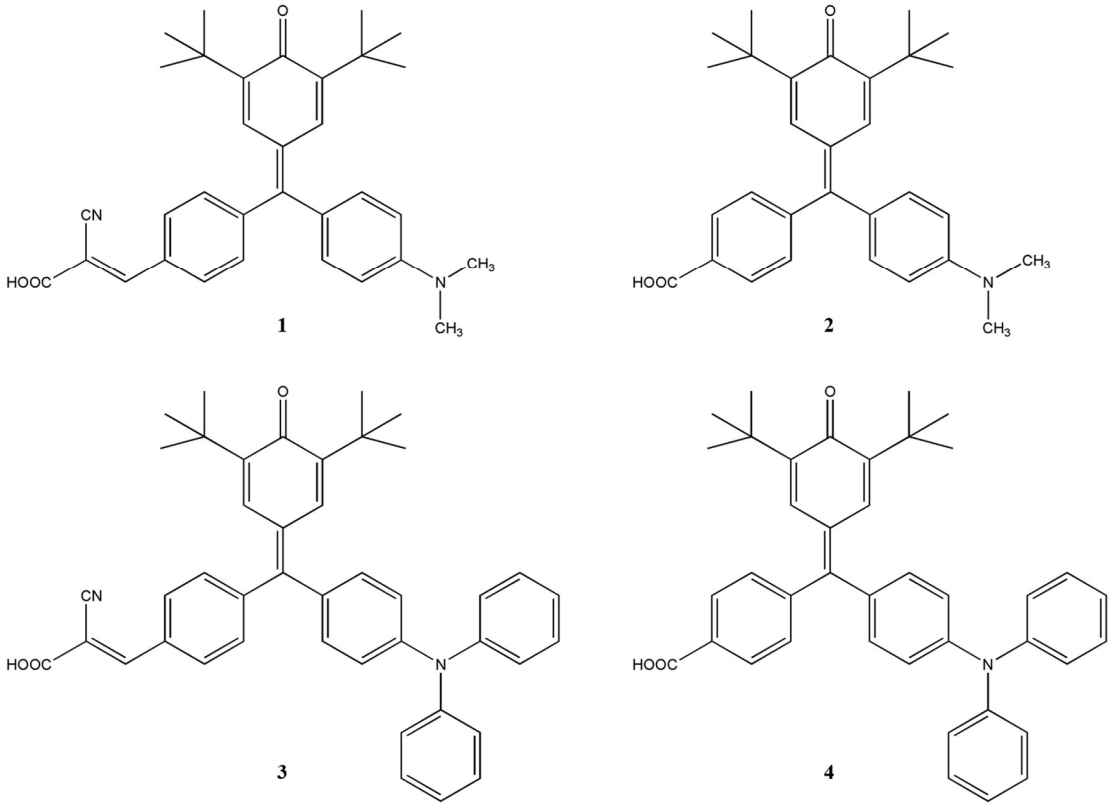

Figure 3.1 Chemical structure and systematic names of **1**-**4**.

3.2 Methods and materials

3.2.1 Experimental details

UV/vis absorption spectra of **1**-**4** in solution or of **1**-**4**/TiO_2 nanocomposites were recorded on an Agilent8453 Diode Array Spectrophotometer (resolution: 2 nm). Emission spectra of **1**-**4** in solution were determined using a Cary Eclipse Fluorescence spectrophotometer with a 20 nm excitation slit and a 20 nm emission slit.

Cyclic voltammograms were recorded using a computer-controlled Autolab PGSTAT101 potentiostat with a three-electrode setup based on a glass carbon working electrode, a platinum wire counter electrode, and an Ag/AgCl reference electrode. The Ag/AgCl reference electrode was calibrated against the ferrocene/ferrocenium (Fc/Fc+) redox couple as the external standard. **1**-**4** were dissolved into acetonitrile containing 0.1 M $[Bu_4N]ClO_4$ (TBAP) as the supporting electrolyte, and voltammograms were recorded at a scan rate of 100 mV/s.

TiO_2 (DSL 18NR-T, Dyesol) photoanodes (thickness: ~4 μm) were generated on well-cleaned FTO glass (Dyesol, TEC-15) by two cycles of the doctor-blade technique, interspersed by drying. The resulting electrode was sintered at 500 ºC for 30 min. Counter electrodes were fabricated using the same doctor-blade procedure, chloroplatinic acid hexahydrate ($H_2PtCl_6 \cdot 6H_2O$, Sigma), and sintering at 375 ºC. All the photoanodes were immersed overnight in methanolic solutions (5×10^{-5} M) of **1**-**4** or N719. The sensitized photoanodes and counter electrodes were assembled by sandwich techniques using a 5×10^{-2} M solution of I^-/I_3^- as the electrolyte (HPE, Dyesol).

To estimate the dye loading on the TiO_2 films, [69] the sensitized electrodes were separately immersed in a NaOH solution (0.1 M) in water:ethanol (1:1, v/v) for the desorption of **1**-**4**. The dye loading was obtained by measuring the absorbance of the resulting solutions, based on the molar extinction coefficients of **1**-**4**, which were obtained from the UV-vis spectra.

The current-voltage (*J-V*) curves and the overall DSSC photovoltaic performances were measured using an ABET Sun 2000 solar simulator under AM1.5 illumination at 100 mW cm^{-2}, after spectral mismatch (active area: 0.5 cm^2).

Electrochemical impedance spectroscopy (EIS) measurements were carried out using an Autolab PGSTAT electrochemical workstation with a frequency range from 10 mHz to 100 kHz. The amplitude of the modulated signal was 10 mV. The active area is 1.0 cm^2 of unsealed device.

3.2.2 Computational details

Isolated dye structures were optimized using the Gaussian 09 software [70] at the B3LYP [59a]/6-31g(d) [71] level of theory, both for vacuum structures and those in methanolic solution (polarizable continuum model, PCM; ε = 32.63).[72] To simulate the interface between the dye molecules and the TiO_2 nanoparticles, the optimized structures (gas phase) of the dye molecules were initially absorbed onto a $(TiO_2)_9$ cluster, [73] to provide a balance between scientific accuracy and computational cost. The geometries of the adsorbed dye molecules were also optimized at the same level of theory. All geometrically optimized structures were checked by the following vibrational frequency calculations at the same level of theory that no imaginary frequency was observed. Single point energy calculations were performed at the B3LYP/6-31g++(d, p) level of theory for the isolated dyes and at the B3LYP/6-31g(d) level of theory for the absorbed dyes. Several adsorption modes are possible for cyanoacrylic and carboxylic groups on TiO_2 nanoparticles, and generally, bidentate anchoring modes are considered more stable than other anchoring modes for similar

interfaces.[74] Therefore, bidentate chelating (B) and bidentate bridging (BB) anchoring modes were considered in this chapter together with the protonated forms (BH, BBH) for model dye **1** and**2**. For dye **1**, the COO/CN binding configuration was also studied as a possible anchoring mode for cyanoacrylic acid group.

Theoretical UV/vis absorption spectra were calculated using TDDFT methods at the M062X[61b]/6-31++g(d,p) level of theory for the isolated dyes and at the M062X/6-31g(d) level of theory for the adsorbed dyes based on the optimized GS structures. The geometries of all dyes in the ES were optimized at the B3LYP/6-31g(d) level of theory.

3.3 Molecular structures and geometries

3.3.1 Molecular structures

For an in-depth discussion of the structures of **1**-**4**, the chemical structures of these compounds were divided into three sub-sections (**a**-**c**):

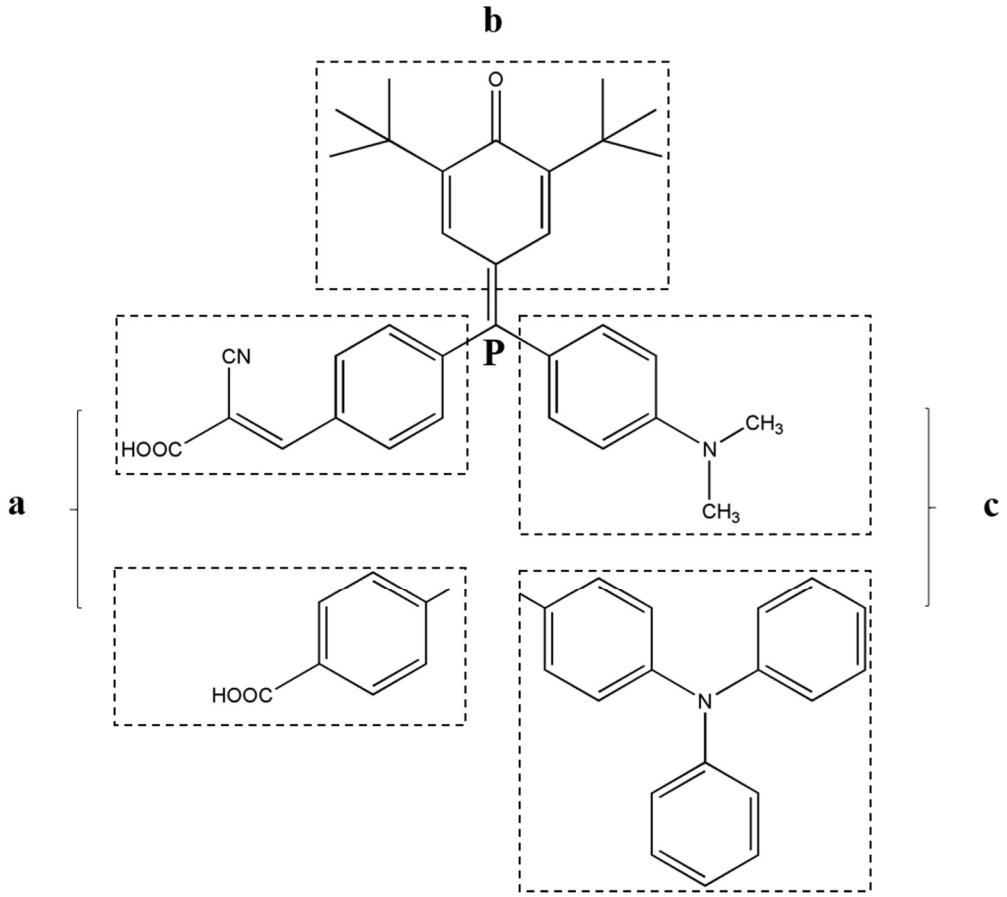

Figure 3.2 Sub-sections **a**-**c** for the chemical structures of **1**-**4**.

As previously mentioned (*cf.* section 3.1), **1**-**4** were designed based on a D-π-A-π-Ads structure with a strong charge-transfer backbone. Section **a** describes the carboxyl acid and the cyanoacrylic acid moieties that act as anchor groups (Ads) for the adsorption of the dye molecules onto the surface of semiconductors such as amorphous TiO_2 in DSSC devices. The phenyl ring in this section between the anchor and point **P** was introduced in order to improve the electron transport from the dye molecule to the dye…TiO_2 interface and suppress electron recombination in the opposite direction.[75] For section **c**, dimethylamino (NMe_2) and diphenylamino (NPh_2) groups were chosen as electron donors (D) to push electrons to the point **P** via the phenyl ring, which acts as the π-bridge in a classic D-π-A structure. Section **b**

describes a 3,5-di(*t*-butyl)quinomethyl group, which should increase i) π-delocalization and ii) the electron-withdrawing ability of **P** as the electron acceptor (A). This topic will be discussed in detail in the next subsection (*vide infra*) on the basis of the results of DFT calculation. The presence of the 3,5-di(*t*-butyl)quinomethyl group should furthermore increase the steric demand of **1**-**4**, which may help to reduce the aggregation of dye molecules and electron recombination from TiO_2 to the electrolyte in DSSC devices. [17]

3.3.2 Optimized ground state geometries *in vacuo*

All frontier molecular orbitals and ground-state (GS) geometries of **1**-**4** were calculated and optimized, respectively using DFT methods at the B3LYP/6-31++g (d,p) level of theory and selected structural parameters of the optimized structures are summarized in Table 3.1.

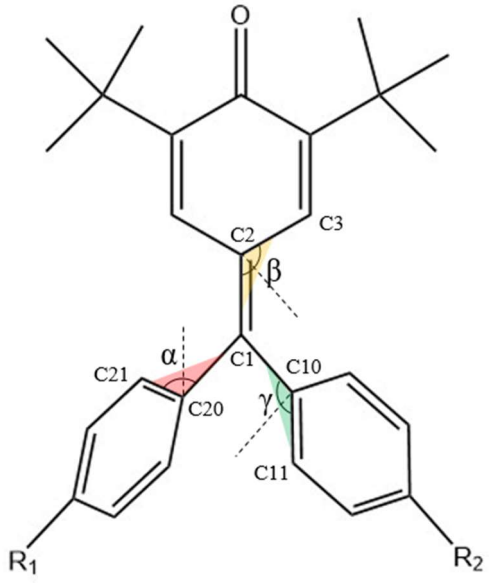

Figure 3.3 The chemical structure of the core part of **1-4** (R1 = –CH=C(CN)COOH or –COOH; R2 = –NMe2 or –NPh2). α, β and γ are dihedral angles of C21-C20-C1-C2, C3-C2-C1-C10 and C11-C10-C1-C20, which are also refer to the three aryl rings

reference to the referenced plane C10-C20-C2.

Table 3.1 Selected structural parameters for **1**-**4**.

Dye	α [°]	β [°]	γ [°]	C1-C2 [Å]	C1-C20 [Å]	C1-C10 [Å]	N-C [Å][a]
1	-46.84	-19.70	-35.87	1.401	1.485	1.462	1.377
1[b 68]	-52.82	-9.22	-39.57	1.382	1.491	1.475	1.371
2	-48.60	-19.72	-34.92	1.400	1.487	1.461	1.378
3	-46.17	-18.19	-40.32	1.396	1.483	1.472	1.407
4	-48.14	-18.24	-38.46	1.395	1.486	1.470	1.408

[a] N-C refers to the length of the bond between the donor and the phenyl ring in section **c**. [b] Experimental values for **1** from reference 68.

As shown in Table 3.1, the N-C bond lengths in **1** (1.377 Å) and **2** (1.378 Å) are similar to typical N-C bond lengths between sp^2-hybridized N and aromatic C atoms (~1.371 Å), [76] which indicates a partial double-bond character, and thus suggests that e.g. **1** or **2** with an NMe_2 group should contain dominant contributions from an electronic resonance structure that carry a positive partial charge on the N atom. And this computational result is also consistent with the N-C bond length of dye **1** from XRD data (1.371 Å).[68] For **3** and **4**, the bond lengths are slightly longer (**3**: 1.407 Å; **4**: 1.408 Å) and between C-N bonds that involve sp^2- (1.371 Å) or sp^3-hybridized (1.426 Å) N atoms, and very close to cationic triphenylamine (1.42 Å), [77] indicating a relatively weak but still positive partial charge on the N atom, induced by the NPh_2 group.

The lengths of the C1-C2 bonds for all dyes are ~1.392 Å,[76] which is typical for C=C double bonds in a quinodimethane structure at the corresponding position. Moreover, this quinodimethane structure, substituted with two *t*-butyl groups, forms a strong electronic resonance structure including C1, which is consistent with the torsion of the ring, i.e., the quinoidal ring offers a more planar structure than the other two phenyl rings (β is only about half of α and/or γ). Thus, a negative partial charge on C1indicates that C1 acts as an electron acceptor (**A**) in the molecule.

The optimized structures suggest that the cyanoacrylic (**1** and **3**) and the carboxyl (**2** and **4**) anchors adopt an almost co-planar arrangement relative to the phenyl ring in section **a**, which affords a beneficial π–conjugated structure that ensures desirable electron injection from the dye molecules to the TiO_2 surface.

3.4 Frontier molecular orbitals and cyclic voltammetry

To determine the properties of the intramolecular charge transfer (ICT) and of the frontier molecular orbitals whose energy levels are a crucial factor for the DSSC performance, the highest occupied molecular orbitals (HOMOs) and lowest unoccupied molecular orbitals (LUMOs) were calculated by DFT methods at the B3LYP/6-31++g (d,p) level of theory, while the energy levels of these orbitals were calculated using time-dependent DFT (TDDFT) methods (*cf.* **Section 3.4.2**). Cyclic voltammetry measurements were used to experimentally determine the HOMO energy levels and to calculate the LUMO energy levels from the band gap energy values obtained from optical measurements.

3.4.1 Cyclic Voltammetry Measurements

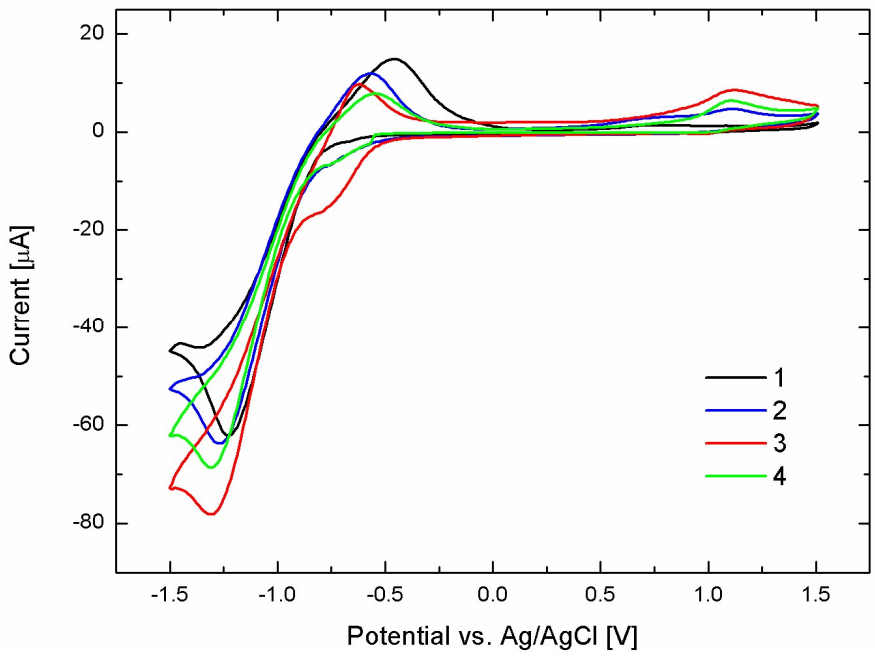

Figure 3.4 Cyclic voltammograms of **1-4** in acetonitrile; [analyte] = 5×10^{-5} mol·L^{-1}; T = 295 K; scan rate = 100 mV·s^{-1}; all potentials vs. Ag/AgCl; 0.1 M additive tetrabutylammonium perchlorate was added as supporting electrolyte.

The cyclic voltammograms measured in acetonitrile (**Figure 3.4**) showed reversible oxidation and reduction curves for all dyes. The oxidation potentials (E) for **1** (0.40 V), **2** (0.32 V), **3** (0.48 V), and **4** (0.43 V) (all potentials vs. Ag/AgCl) were assigned to the oxidation of the donor group (**1**, **2**: NMe_2; **3**, **4**: NPh_2). The oxidation of **1** and **2** at lower potentials than those of **3** and **4** should be attributed to the lower electron-donating ability of the NMe_2 group relative to that of the NPh_2 group, and to the consequently weaker interactions between the acceptor and the donor. The HOMO energy levels for **1-4** were determined based on the onset of the individual oxidation potentials, while the LUMO energies were obtained from the sum of the corresponding HOMO energy level and the optical band gap (*cf.* **Section 3.5.1**). A

summary of the relevant data is given in **Table 3.2**. The HOMO energy levels of **1**-**4** are lower than the redox potential of the most commonly used DSSC electrolyte (I^-/I^{3-}), which renders the regeneration of the dye molecules possible. The LUMO energy levels are sufficiently high to provide the driving force for electron injection from the excited dye molecules into the TiO_2 conduction band (CB).

Table 3.2. CV-derived oxidation potentials and calculated HOMO and LUMO energy levels.

Dye	E [V]	HOMO[a] [eV]	E_g^{opt} [b] [eV]	LUMO [c] [eV]
1	0.40	-5.15	2.06	-3.09
2	0.32	-5.07	2.15	-2.92
3	0.48	-5.23	2.16	-3.07
4	0.43	-5.18	2.19	-2.97

[a] set Fc^+/Fc E_{HOMO} = -4.8 eV; [b] estimated using the onset of the UV-vis spectra in methanol; [c] calculated from the sum of the HOMO value and E_g^{opt}.

3.4.2 DFT- and TDDFT-derived HOMOs and LUMOs

The calculated HOMO and LUMO energy levels (**Table 3.3**show the same trend as the results of the cyclic voltammetry measurements and optical studies.

Table 3.3. DFT- and TDDFT-derived HOMO and LUMO energy levels.

Dye	HOMO [a] [eV]	LUMO [c] [eV]	E_g^{TD} [b] [eV]
1	-5.408	-2.909	2.499
2	-5.385	-2.724	2.661
3	-5.447	-2.857	2.590
4	-5.434	-2.716	2.718

[a] Calculated by DFT methods: B3LYP/6-31++g(d,p)/PCM in methanol; [b] calculated by TDDFT methods: M062X/ 6-311+g(d,p)/PCM in methanol; [c] calculated from the sum of the HOMO value and E_g^{opt}.[78]

As shown in **Figure 3.5**, the HOMOs in the ground state is comparable for **1**-**4**, and the electron density is located predominantly on the donor moiety (NMe_2 or NPh_2) and the quinodimethane backbone. The LUMOs are located mainly on the (carboxylic or cyanoacrylic) anchor groups and the quinodimethane backbone. In addition, small parts of the LUMO of **2** and **4** are situated on the phenyl ring that connects the quinodimethane moiety and the donor group. Generally, **1**-**4** exhibit very good HOMO-to-LUMO charge redistribution from the donor to the anchor moieties, which renders the injection of excited electrons into the CB of TiO_2 possible.

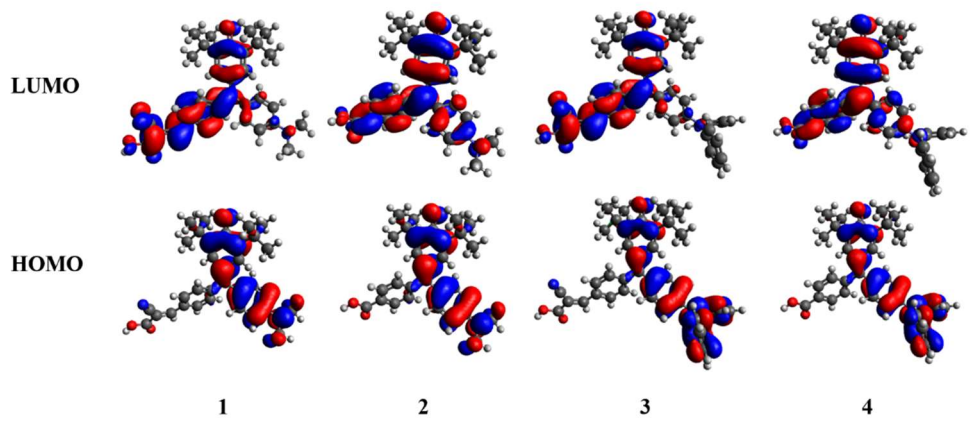

Figure 3.5 Calculated electron density distributions for the frontier molecular orbitals of **1**-**4** using DFT methods based on B3YLP/6-31++g (d,p)/PCM.

It should be noticed that the quinodimethane backbone between the donor and acceptor moieties offers sufficient overlap between the HOMOs and the LUMOs, which guarantees fast charge transfer transition.[2] Due to the pronounced alternation of the bond lengths, the quinodimethane structure should be isolated from charge transfer processes.[79] The first excitation of **1**-**4** in methanol was also studied by TDDFT methods at the M062X/6-31++g (d,p) level of theory. The calculated first excitation energies are in excellent accordance with the results of the UV-vis measurements for **1** and **3**, but slightly disagree with those for **2** and **4** (**Figure 3.8**). This divergence may be caused by the difference of anchor groups in reorganization and electron density in the excited state.

3.5 Optical band gaps and first excitation energies

To investigate the absorption and emission properties of **1**-**4**, UV-vis and emission spectra were measured to determine the optical band gaps, and TDDFT methods were used to calculate the first excitation energies and the excited states of **1**-**4**.

3.5.1 UV-vis absorption and emission spectra in methanol

The UV-vis absorption spectra of **1**-**4** in methanol are shown in **Figure 3.6**. A summary of all data is shown in **Table 3.4**.

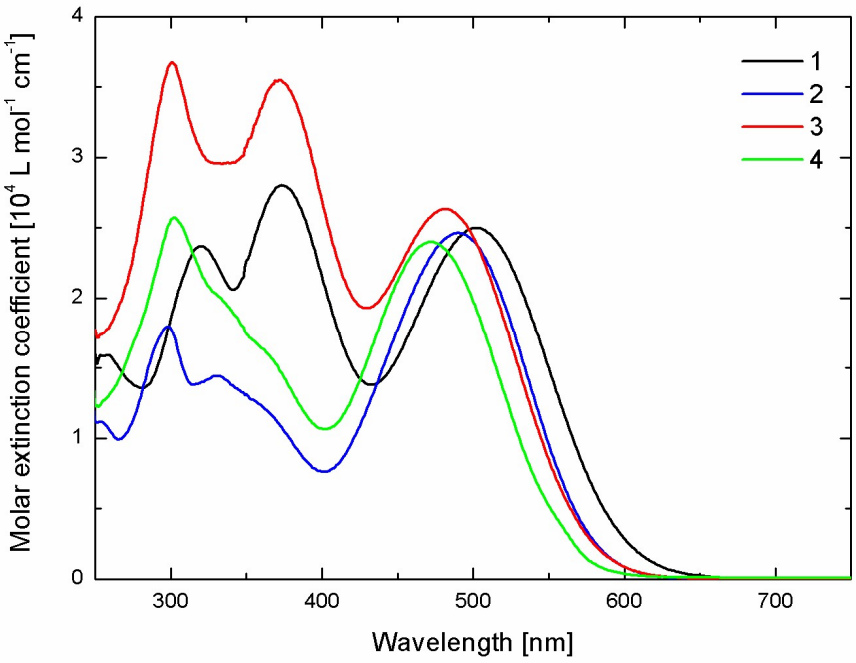

Figure 3.6 Absorption spectra of **1**-**4** in methanol ([dyes] = 5 × 10^{-5} mol^{-1} L).

The absorption spectra of **1** and **3**, as well as of **2** and **4** exhibit similar features, which indicates that certain strong excitation processes (300-450 nm) occur in the area of the anchor groups. For **1** and **3**, which contain cyanoacrylic acid anchors, the absorption bands at shorter wavelength (**1**: 320 and 375 nm; **3**: 301 and 372 nm) should be attributed to the aromatic π–π* electronic transition of the conjugated backbone, while the longest wavelength absorption band of **1** ($\lambda_{max, abs}$ = 503 nm) should be assigned to an ICT [68] that is slightly red-shifted compared to that of **3** ($\lambda_{max, abs}$ = 482 nm). For **2** and **4**, which contain carboxylic acid anchors, the longest wavelength absorption bands of **2** and **4** exhibit a similar trend for the ICT (**2**: $\lambda_{max, abs}$ = 490 nm; **4**: $\lambda_{max, abs}$ = 472 nm). For the shorter wavelength absorption bands, **2** and **4**

exhibit shoulder peaks at 310-400 nm, which may be attributed to several close π–π* transitions. Moreover, the ICT band of **1** and **3** is more intensive than that of **2** and **4**, indicating stronger ICT interactions in **1** and **3** due to a higher degree of π-delocalization, extended by the cyanoacrylic acid.

Table 3.4 Data of UV-vis and emission spectra of dye **1**, **2**, **3** and **4**.

Dye	$\lambda_{max,\ abs}$ [nm]	ε_{max} [$Lmol^{-1}cm^{-1}$]	$\lambda_{max,\ em}$ [nm]	Stokes shift [cm^{-1} (nm)]	E_g^{opt} [a] [eV]
1	503	2.50×10^4	647	4425 (114)	2.06
	375	2.80×10^4			
2	490	2.46×10^4	608	3961 (118)	2.15
	358	1.25×10^4			
3	482	2.63×10^4	638	5073 (156)	2.16
	372	3.55×10^4			
4	473	2.40×10^4	616	4907 (143)	2.19
	362	1.63×10^4			

[a] Estimated using the onset of the UV-vis spectra in methanol.

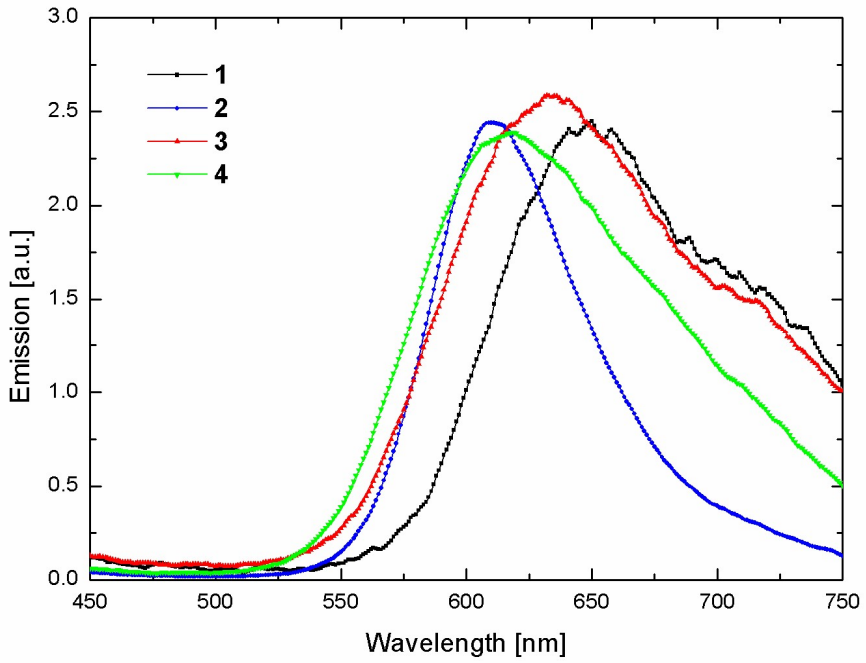

Figure 3.7 Normalized emission spectra of **1-4** in methanol ([dye] = 1×10^{-3} mol L^{-1}; λ_{ex} = 400 nm).

The emission spectra of **1-4** (Figure 3.7) show Stokes shifts in the UV/vis range to 647 (**1**), 608 (**2**), 638 (**3**), and 616 nm (**4**). The Stokes shifts of **3** (4907 cm^{-1}) and **4** (5073 cm^{-1}) are substantially larger than those of **1** (4405 cm^{-1}) and **2** (3961 cm^{-1}), indicating that these shifts may be dominated by a structural reorganization of the donor group. A more detailed comparison of the molecules that contain the same donor (NMe_2) showed that the Stokes shift of **2** is slightly smaller than that of **1**, which means that a small additional change in geometry must also occur between the ground state (GS) and the excited state (ES), whose nature affects the position of the anchoring group relative to that of the donor group. Considering the individual structures, the most probable geometry reorganization from the GS to the ES is some form of twist in the aryl rings in the π-bridge that connects the donor and anchoring groups. Thus, in section 3.5.2, DFT and TD-DFT studies were employed in order to

verify this chemical intuition about the nature of the geometry reorganization upon photo-excitation.

3.5.2 First excitation energies

The first excitation energies of **1**-**4** in methanol were studied by TDDFT calculations at the M062X/6-31++g (d,p) level of theory. A comparison between the experimental and the calculated TDDFT results is shown in **Figure 3.8**. The differences between the energy values of the calculated first excited-state transitions and the ICT wavelengths from the UV-vis spectra of **1** (0.01 eV), **2** (0.13 eV), **3** (0.02 eV), and **4** (0.09 eV) show that the calculated first excitation energies agree well with the results of the UV-vis spectra, especially for **1** and **3**, considering that the error using hybrid functionals does not exceed 0.4 eV.[80] For **2** and **4**, however, the discrepancy between experimental and theoretically calculated values is more substantial, which may be attributed to their anchoring group, the carboxyl acid group, which has a smaller π-conjugated structure compared to a cyanoacrylic acid group for **1** and **3**.

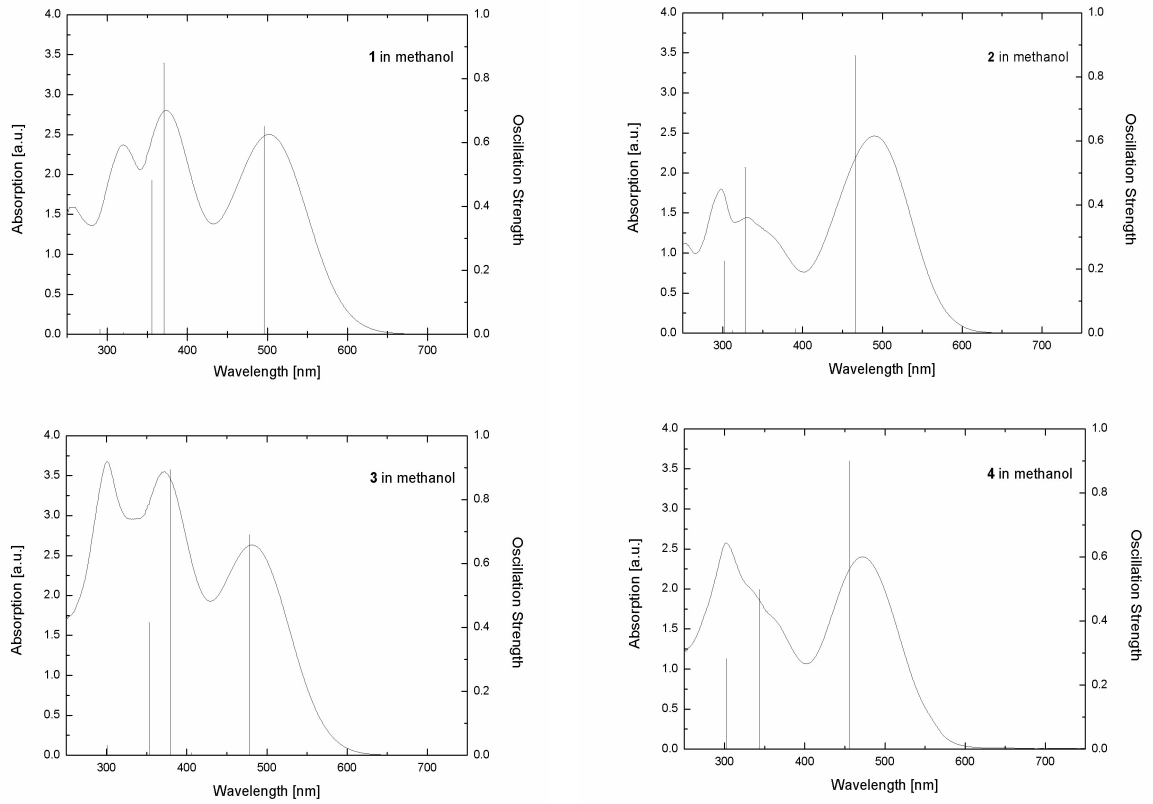

Figure 3.8 Theoretically calculated absorption spectra for **1**-**4** in methanol via TDDFT (vertical lines) and UV-vis absorption data (curves).

The compositions of the excitations in terms of molecular orbital transitions were also calculated (**Table 3.5**), and the results show that the ICT absorption bands of **1**-**4** should be attributed mainly to the HOMO-LUMO transitions. The subsequent two calculated excited-state transitions in **1** and **3** (n = 3, 4) and **2** and **4** (n = 3, 5) correspond to the experimentally observed absorption peaks at shorter wavelengths, and should be associated with two overlapping π - π* transitions of different characters.[81] The transitions with n = 3 for **2** (3.78 eV), **3** (3.27 eV), and **4** (3.61 eV) should be ascribed to the HOMO-1–>LUMO π - π* transition, which occurs from

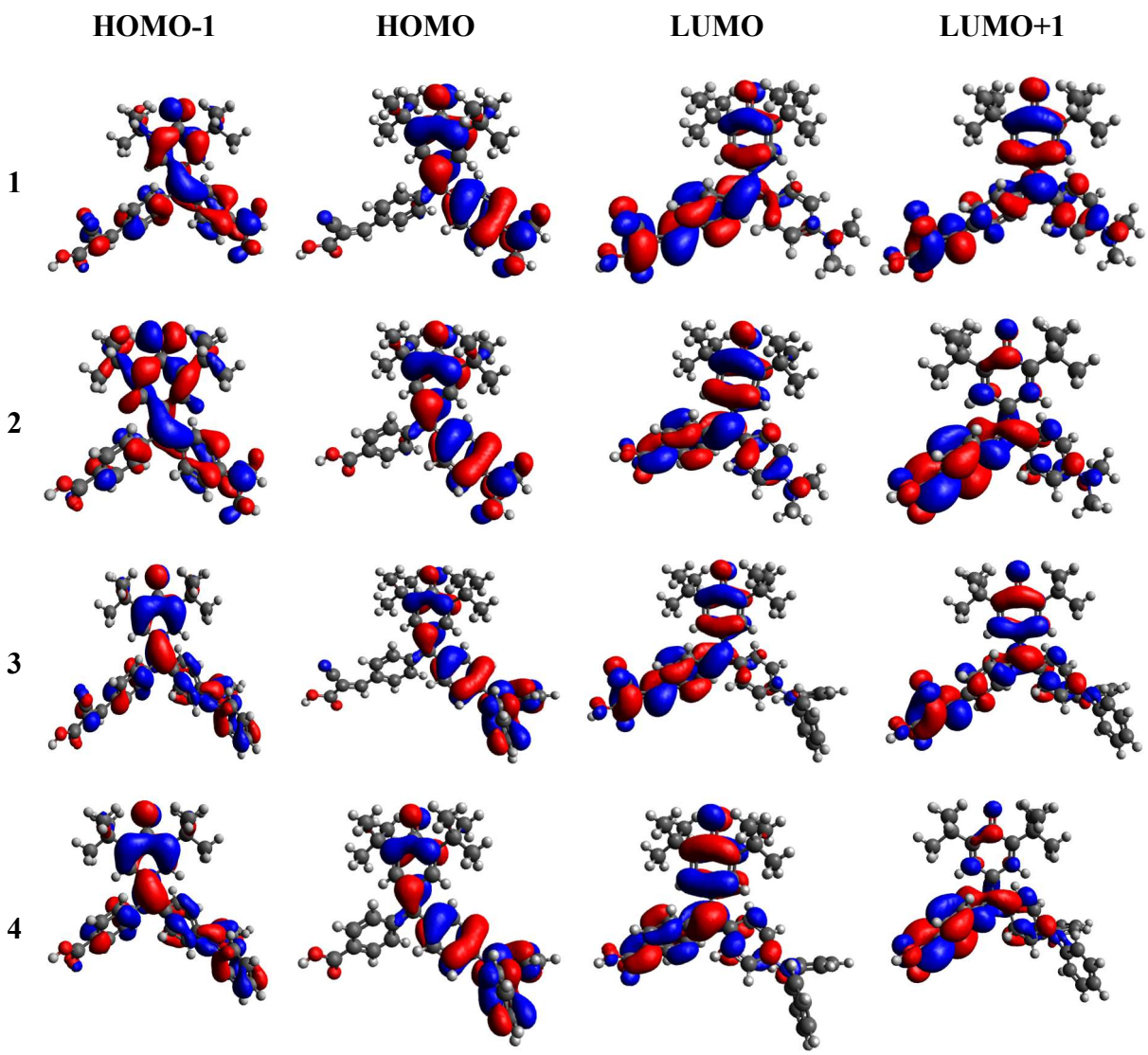

both phenyl rings in section **a** and **c** and exhibits localized excitation (LE) character. Following a similar argument, the higher energy transitions with n = 4 (**2**) and n = 5 (**3**, **4**) can be attributed to the HOMO–>LUMO+1 π - π* transitions, even though the HOMO–>LUMO+1 transition of **2** and **4** does not involve molecular orbitals at the quinodimethane backbone (section **b**), which is very distinct from all other transitions.

Figure 3.9 Electron density distributions of the HOMO-1, HOMO, LUMO, and LUMO+1 of **1**-**4** calculated at the DFT/B3LYP/6-31++g(d,p)/PCM (methanol) level of theory.

For **1**, there are no dominant molecular orbitals for n = 3, 4, as the contributions from the HOMO-1–LUMO and HOMO–LUMO+1 are comparable. Accordingly, the characteristics of these two transitions cannot be simply judged by the electron-density distribution of the frontier molecular orbitals. Therefore, the electron-hole-density distributions of the molecular orbitals of the ES of **1** (n = 3, 4) were generated using Multiwfn 3.3.9.[82] The hole and electron distribution for n = 3, 4 (**Figure 3.10**) shows that almost all the holes are located on the donor moiety, and that the electrons are predominantly concentrated on the acceptor and anchor moieties, which indicates that these two excitations exhibit mainly charge-transfer (CT) characteristics and good hole-electron separation.

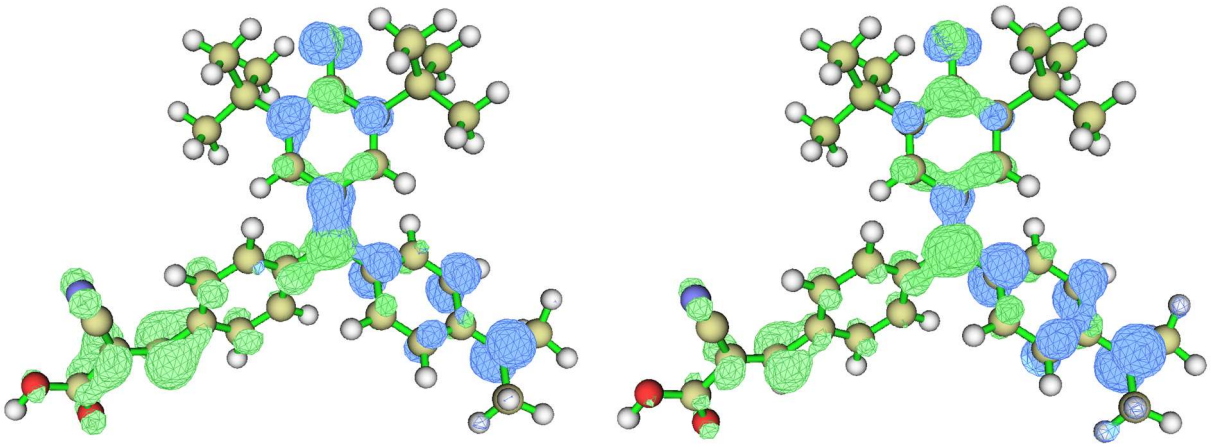

(a) **(b)**

Figure 3.10 Hole-electron density distribution of the excited states of **1** for n = 3 (a) and n = 4 (b) calculated at the DFT/B3LYP/6-31++g (d, p)/PCM (methanol) level of theory. Plots were realized using Multiwfn 3.3.9. Blue and green isosurfaces represent hole and electron distributions, respectively.

Table 3.5 Energy (eV, nm) and oscillator strength values for **1**-**4**, as well as sizable (f > 0.1) contributions of the molecular orbitals to the transitions.

Dye	ES (*n*)	First excitation energy [eV]	[nm]	Oscillator strength (*f*)	Composition	
1	1	2.499	496.07	0.6512	90.69%	HOMO - LUMO
	3	3.345	370.64	0.8487	47.75%	HOMO-1 - LUMO
					42.86%	HOMO - LUMO+1
	4	3.485	355.81	0.4828	39.78%	HOMO-1 - LUMO
					45.88%	HOMO - LUMO+1
2	1	2.661	465.87	0.8657	96.41%	HOMO - LUMO
	3	3.780	327.96	0.5174	91.75%	HOMO-1 - LUMO
	5	4.108	301.81	0.226	91.26%	HOMO - LUMO+1
3	1	2.590	478.71	0.69	84.55%	HOMO - LUMO
	3	3.268	379.36	0.8924	73.75%	HOMO-1 - LUMO
	4	3.512	353.02	0.4154	68.90%	HOMO - LUMO+1
4	1	2.718	456.17	0.8998	90.93%	HOMO - LUMO
	3	3.606	343.84	0.499	87.97%	HOMO-1 - LUMO
	5	4.095	302.80	0.283	61.39%	HOMO - LUMO+1

3.5.3 Optimized structures for the excited states (ES)

To better understand the origin of the different Stokes shifts and the properties of **1**-**4** in the ES, the geometric structures of these dyes in the ES were optimized by

DFT/TDDFT methods at the same level of theory as the GS. The metric parameters for the ES are listed in Table 3.6 and a juxtaposition "(overlapping two geometries by fixing three points: C2, C10 and C20) of the corresponding optimized structures is shown in **Figure 3.11**.

Table 3.6 Structural parameters for the ES of **1**-**4**.

Dye	Excited State					
	α[a]	β	γ	C1-C2 [b]	C1-C20	C1-C10
1	-23.74	-14.8	-86.81	1.422	1.433	1.499
	(23.10)[c)]	(4.9)	(-50.94)	(0.021)	(-0.052)	(-0.037)
2	-15.08	-23.08	-88.98	1.431	1.440	1.497
	(33.52)	(-3.36)	(-54.06)	(0.031)	(-0.047)	(0.036)
3	-17.95	-27.76	-61.59	1.418	1.437	1.499
	(28.22)	(-9.57)	(-21.27)	(0.023)	(-0.046)	(0.027)
4	-16.21	-23.98	-79.77	1.430	1.440	1.500
	(31.93)	(-5.74)	(-41.31)	(0.035)	(-0.046)	(0.030)

[a] α, β and γ are dihedral angles of C21-C20-C1-C2, C3-C2-C1-C10 and C11-C10-C1-C20 (*cf.* Figure 3.3). The signal "-" denominates an anticlockwise rotation relative to C1; [b] C-C defines the bond length (Å) of the corresponding carbon atoms; [c] Values in parentheses represent Δparameter = parameter(GS)-parameter(ES).

The ES molecular structures of **1-4** show consistent differences to those of the GS particularly with regard to the relative orientation of the three aryl groups. The C1-

C20 bond lengths are shorter in the ES to the extent that its bonding manifests a more delocalized nature. The adjoining C1-C2 bond is longer in the ES such that its distinctly double-bonded GS character (*cf.* 1.392 Å for a purely double C=C bond[76]) is better described as π-delocalized in the ES structure. The π-bridge that connects the quinone with the phenyl ring which features the electronic acceptor would therefore appear to be more delocalized in the ES structure. The associated dihedral angle between the plane of the aryl ring and the referenced plane, α, shown in Figure 3.3, is smaller in the ES, indicating that π-conjugation will extend more readily between them subject to a suitably delocalized π-bridging connection; and the nature of this is enhanced in the ES structure relative to that of the GS. The combined effects mean that for the ES structure, more ICT between these two planes will result, strengthening the role of the electron acceptor group.

The C1-C10 bond involved in the π-bridge that connects to the dialkylamino-phenyl moiety becomes much longer in the ES, to the extent that it is best described as a single C-C bond (*cf.* 1.54 Å for a purely $C(sp^3)$-$C(sp^3)$ bond[76]). The origin of this bond elongation can be understood by considering the substantial increase in dihedral angle between the referenced plane and the involved aryl ring, γ, upon realizing the ES structures of **1-4**: Δγ values of 50.94°, 54.06°, 21.27°, 41.31° respectively. The particularly large Δγ value for **2** means that ICT will be hindered between the electron donor and anchoring groups; as such, there will be little chance of electron back transfer for the D-to-Anc ICT that occurs. Moreover, the dimethylamino-phenyl moiety lies almost perpendicular (86.81° for **1** and 88.98° for **2**) to the plane, C10-C20-C2, which contains the π-bridge that links all three aryl rings in **1-4**. So the

ability of the π-bridge to channel π-conjugation between rings in **1** and **2** is severely compromised.

Considering Δα and Δγ values together with the Stokes shift observations for **1-4** from the UV/vis and emission spectroscopy data, their ES geometries could be more effectively understood. The much larger Δγ values for **1** and **2** present distinctly smaller Stokes shifts compared to **3** and **4**, indicating that the steric effect of the donor moiety may be one of the dominant factors in affecting the Stokes shift of these dyes since the diphenylamino group is more sterically bulky than the dimethylamino group. That said, the bulkier nature of the anchoring group in **1** compared with **2** also needs to be considered. Despite **1** having a smaller Δγ than **2, 1** still shows a larger Stokes shift than **2** owing to its larger Δα value which is affected by the anchoring group, whereby the cyanoacrylate substituent is more sterically bulky and electron rich than the carboxylate group in **2**.

All of these factors combined mean that the π-conjugation in the acceptor group of **2** is particularly strengthened upon forming its ES structure, while it is attenuated in the donor; this effect should ultimately promote charge separation upon photoexcitation. In contrast, the large twist in the dimethylamino-phenyl moiety of **2** hinders ICT such that it almost eliminates a potential back electron transfer from TiO_2 through to the donor group in **2** via its acceptor in the ES; this may effectively suppress electron recombination in DSSCs. Also, this large twist appears to raise the HOMO level, judging from the fact that the HOMO energies follow the same trend as Δγ, i.e. E_{HOMO} for **2** > **1** > **4** > **3.**

Accordingly, the suspected twisting of the phenyl group in the donor region of **1-4** is supported by these computational studies. Moreover, the calculations explain the origin of the distinct emission features that are experimentally observed in **2**. Meanwhile, the photovoltaic prospects for **2** as a DSSC dye are attractive on account of the predicted diode-like action of the phenyl twisting upon formation of its ES which will help prevent undesirable electron recombination effects.

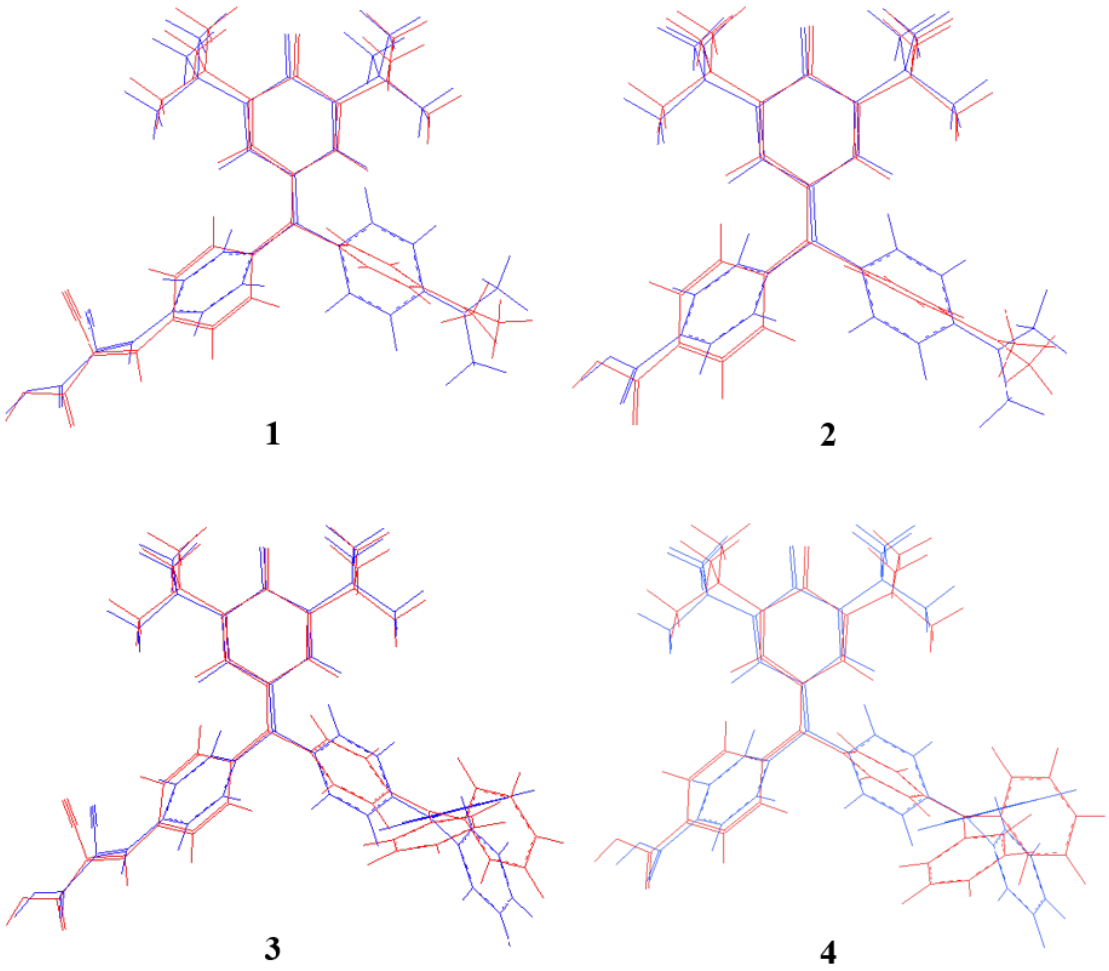

Figure 3.11 Juxtaposition of the optimized structures of **1-4** in the ground (blue) and excited state (red).

3.6 Preferred Anchoring Configurations of 1-4 on TiO_2 Surfaces

3.6.1 Anchoring configuration by DFT calculation.

The possible adsorption modes of **1-4** on TiO_2 were assessed using DFT calculations that employed a $(TiO_2)_9$ cluster model to simulate the interface between the dyes and the TiO_2 films. For dyes that contain a carboxylic acid anchor (*c.f.* **2** and **4**), the four most common anchoring modes in its protonated or deprotonated form are shown in figure 3.12(a),[74] i.e., bidentate chelating (B and BH) and bidentate bridging (BB and BBH). These four possibilities were used as models to investigate the adsorption behavior of **2**, taking this dye as representative for dye···TiO_2 adsorption of **2** and **4**.

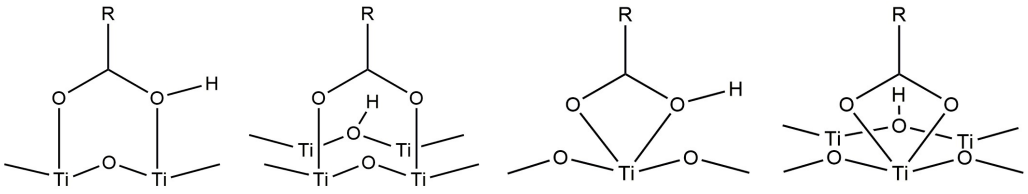

(a)

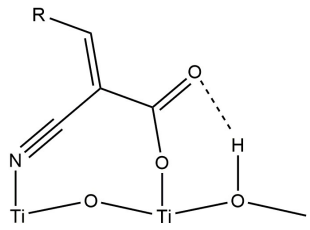

(b)

Figure 3.12 (a) The four most common adsorption modes for the carboxylic acid anchoring group on TiO_2: protonated (BBH) and deprotonated (BB) bidentate bridging anchoring, as well as protonated (BH) and deprotonated (B) bidentate chelating. (b) The possible CN/COO adsorption mode for the cyanoacrylate acid anchoring group on TiO_2.

For dyes featuring a cyanoacrylate acid anchoring group (*c.f.* **1** and **3**), there is an additional adsorption mode possibility, given that the nitrogen of its nitrile group may also contribute to the adsorption via a COO/CN binding configuration (see figure 3.12(b)).[83] This COO/CN anchoring mode was therefore studied for **1**, as representative for dye···TiO_2 adsorption of **1** and **3**, in addition to the options that are available for a carboxylic acid anchoring group.

Dye···TiO_2 adsorption energies were calculated according to:

$$E_{ads} = E_{dye\ldots TiO_2} - E_{dye} - E_{TiO_2}, \qquad \text{(eq 3.1)}$$

wherein *E* refers to the DFT-calculated single-point energy, and all the calculations were based on optimized structures of dye…TiO_2 model, free dye molecule and TiO_2 cluster respectively.

In the case of **1**, the BBH mode showed, by far, a higher adsorption energy than all of the other possibilities and so was ruled out. The remaining anchoring options were considered in light of not only the adsorption energies but also the photoexcitation properties of **1**. To this end, the TD-DFT results revealed that the B and BB modes show hypsochromic shifts of 45.51 and 29.49 nm for the first excitation energy upon adsorption, which is in good agreement with the hypsochromic shift measured by UV-vis absorption spectroscopy ($\Delta\lambda$ = 39 nm; Figure 3.13). The DFT model containing the CN/COO anchoring mode shows the lowest adsorption energy while its cognate TD-DFT results yielded a hypsochromic shift of $\Delta\lambda$ = 10.49 nm which is much smaller than that of experimental UV-vis spectroscopy finding. In contrast, the TD-DFT results for the BH mode suggest a bathochromic shift ($\Delta\lambda$ = ~16 nm) upon

adsorption. Comparing the best overall merits of these modes in terms of the adsorption and first excitation energies (Table 3.7), it would seem that the BB mode presents the most feasible adsorption mode for the dye···TiO_2 interface. This notion should also strengthen the view that deprotonation of the anchoring group upon dye adsorption may induce the hypsochromic shift observed in the UV-vis absorption spectra.

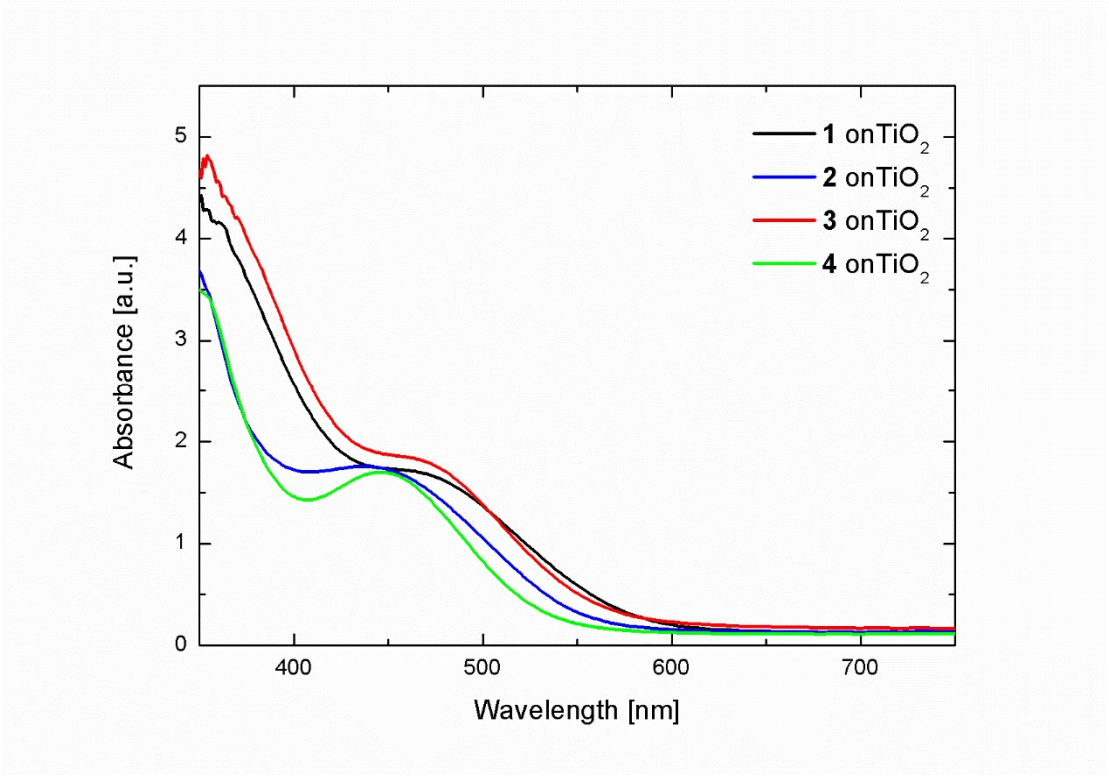

Figure 3.13. Absorption spectra of **1-4** on thin films of TiO_2 (thickness: 4 μm). The absorptions peaks for **1-4** on TiO_2 films are all shown a hypsochromic shift compared to that in methanol. (503→464 nm for **1**, 490→437 nm for **2**, 482→474 nm for **3** and 473→446 nm,for **4**)

In the case of **2**, the BBH mode showed a markedly higher adsorption energy than the other modes, in common to the case for **1**, thus precluding this option as a binding mode for this type of dye. In terms of photoexcitation properties of **2**, the TD-DFT

results on the structures containing B, BH and BB modes predict a hypsochromic shift of the first excitation energy once the dye has been adsorbed onto TiO_2. However, all of their shifts (see table 3.7) are noticeably smaller than that observed experimentally by UV-vis absorption spectroscopy ($\Delta\lambda$ = 53 nm); those of the B and BB modes offer the closest agreement with experiment. Taking both adsorption and first excited state energies into account, the BB anchoring mode would appear to be the best choice for **2** to anchor on the surface of TiO_2; this conclusion is also consistent with the preferred anchoring mode for **1**.

Table 3.7. Calculated first excitation and adsorption energies for the different adsorption modes of **1** and **2** on TiO_2.

Adsorption Mode	First excitation wavelength [nm]	ΔFirst excitation energy [a] [nm]	Adsorption energy [eV]
1B	450.56	-45.51	-0.902
1BH	512.64	16.57	-1.099
1BB	466.58	-29.49	-0.957
1BBH	542.19	46.12	-0.197
1CN/COO	485.58	-10.49	-1.200
2B	425.90	-39.97	-0.892
2BH	459.09	-6.78	-0.993
2BB	429.82	-36.05	-0.985
2BBH	445.21	-20.66	-0.442

[a] ΔFirst Excitation Energy = First Excitation Energy (dye on TiO_2) - First Excitation

Energy (dye in methanol). The sign "-" refers to a hypsochromic shift relative to the energy for the unadsorbed dye dissolved in a methanol solution.

3.6.2 Dye loading

To verify the effect of the anchor group on the dye loading, which is a crucial parameter for the DSSCs performance, a 0.1 M NaOH solution in a water:ethanol (1:1, v/v) was used for the desorption of **1**-**4** on the TiO_2 films (~ 4 μm). And then the dye loading amount can be obtained by measuring the absorbance of the resulting solutions, based on the based on the molar extinction coefficients of **1**-**4**, which were obtained from the UV-vis spectra.[69]

Table 3.8 Dye loadings for **1**-**4** on TiO_2.

Dye	Dye loading [10^{-7}mol cm^{-2}]
1	0.89
2	0.82
3	0.63
4	0.76

Table 3.8 summarizes the estimated dye loadings for **1**-**4**. The fact that **1** and **2** show better adsorption on TiO_2 films than **3** and **4** indicates that the cyanoacrylic acid anchor may adopt the same adsorption mode as the carboxylic acid anchor. Moreover, the steric bulk of the NPh_2 group in **3** and **4** should require more surface space per

molecule and thus reduce the total amount of adsorption sites available on the TiO_2 surface.

3.7 Electrochemical Impedance Spectroscopy of 1-4

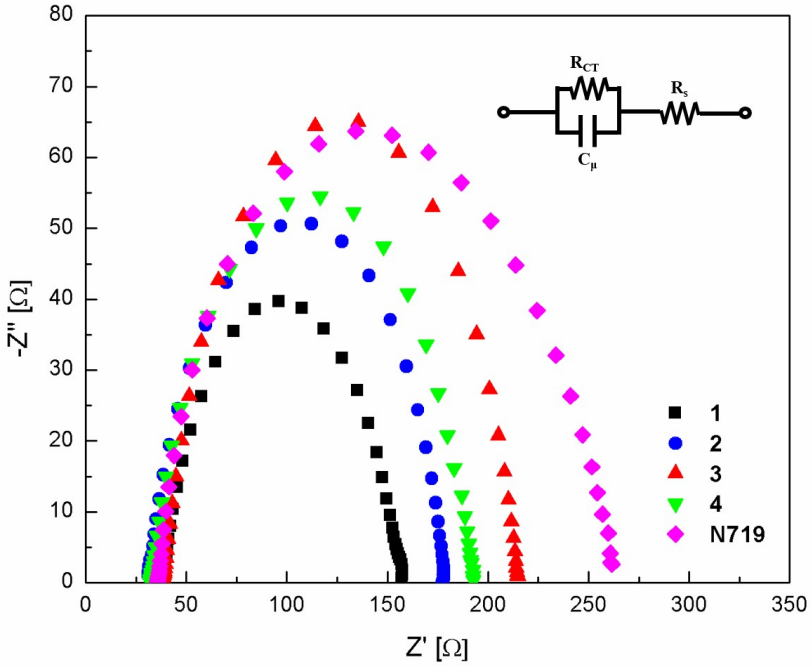

Figure 3.14 The EIS Nyquist plot of **1-4** measured from 100 kHz to 10 mHz under dark condition with a forward bias of -0.60 V; (inset): the corresponding equivalent circuit. The active area is 1.0 cm^2.

Figure 3.14 shows the Nyquist plots of the corresponding devices with the equivalent circuit in the figure inset. The simulated data from the EIS spectra are summarized in Table 3.9. The semicircle observed in the figure represents the electron recombination process at the TiO_2/dye/electrolyte interfaces. The calculated resistance values (R_{CT}) are 82.2 Ω/cm^2, 105.1 Ω/cm^2, 126.1 Ω/cm^2, and 116.4 Ω/cm^2 for dye **1-4** respectively. Generally the larger the R_{CT}, the slower the recombination kinetics. The associated R_{CT} values for **1-4** present in the order **1** < **2** < **4** < **3**, indicating the relative

extent by which electron recombination can be suppressed for interfaces involving **1-4**. Therefore, it seems that charge recombination from TiO_2 to electrolyte in dye **3** and **4** could be more efficiently blocked may be due to the steric effect of their diphenylamino groups which reduce the contact of TiO_2 and I_3^- in the electrolyte. And **1** and **2** show smaller R_{CT} values indicating that the dimethylamino groups are less efficient to suppress this recombination at the TiO_2/dye/electrolyte surface. Compared to the benchmark, **3** shows a comparable R_{CT} value to **N719** (138.0 Ω/cm^2), but generally all the dyes are need to be further improved to compete with **N719** in suppressing this recombination.

However, to investigate how the twist of diakylamino-phenyl ring affect the charge transfer process in DSSC, EIS spectra measured under illumination are needed, which can characterize the charge transfer process in the working state. So due to the limitation of equipment, EIS spectra under illumination are not discussed in this thesis and needed to be further investigated in the future.

Table 3.9. Simulated data, R_{CT}, C_μ and R_S values of **1-4** from EIS measurements.

Dye	R_{CT} [Ω/cm^2]	C_μ [$\mu F/cm^2$]	R_S [Ω]
1	82.2	0.001327	61.4
2	105.1	0.001120	58.4
3	126.1	0.001117	69.5
4	116.4	0.001144	60.4
N719	138.0	0.000715	95.7

3.8 Photovoltaic (PV) performance

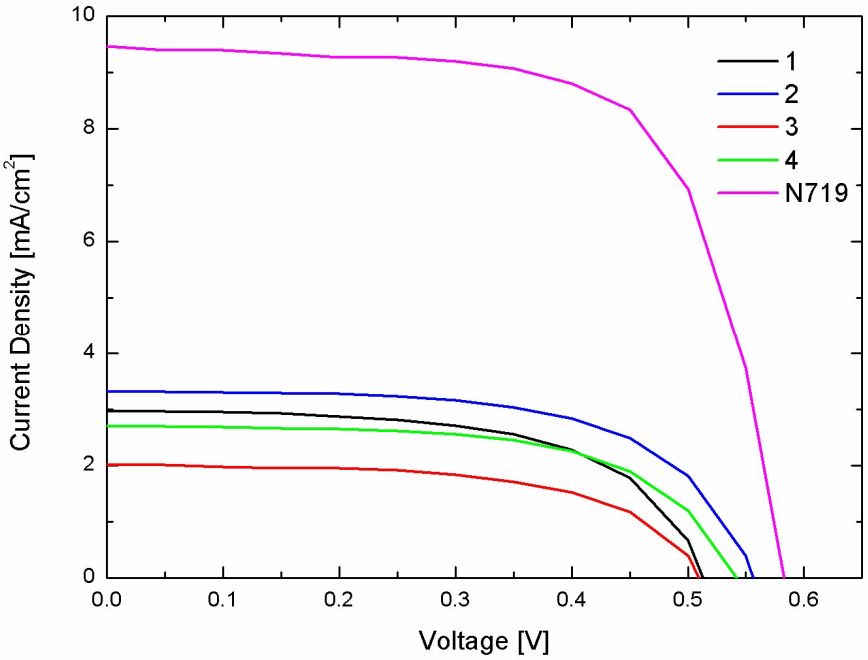

Figure 3.15 Current density as a function of voltage for DSSCs containing **1**-**4** or **N719**.

To further examine the photovoltaic performance of **1**-**4**, a series of unsealed DSSCs were prepared using thin layers (4 μm) of TiO_2 nanoparticles to ensure compatibility with the high extinction coefficient of the organic dyes. **Figure 3.15** shows the current density of these DSSC devices as a function of voltage (*J*-*V* curves). In general, **1**-**4** still cannot compete with the DSSC performance of **N719**, especially given their low current densities that arise from the narrow absorption band and strong recombination. The dye with the best performance (**2**) exhibits an overall efficiency, η, which is ~30% of the efficiency of **N719**. The short-circuit current density, J_{SC}, shows the same trend of **2** > **1** > **4** > **3** as that of Δγ and R_{CT}, which corroborates the notion that the pronounced twist of the dialkylamino-phenyl moiety

blocks back-electron transfer from the acceptor to the donor in the ES, and thus suppresses the recombination of electrons from the CB of TiO_2 to the donor group of the dye. This diode-like effect presents as a structure-function relationship for this class of dyes. Its encoding into a knowledge-based rule for the molecular engineering of derivatives of **1-4** could be highly advantageous in helping produce superior photovoltaic properties in DSSC devices while precluding undesirable electron recombination effects.

Table 3.10 Photovoltaic parameters of DSSCs containing **1**-**4** or N719.

Dye	V_{OC} [V]	J_{SC} [mA/cm^2]	FF [%]	η [%]	η_{dye}:η_{N719} [%]
1	0.516±0.005	2.88±0.47	59.6±1.4	0.89±0.13	23.8
2	0.540±0.009	3.43±0.26	60.7±1.4	1.13±0.07	30.2
3	0.510±0.003	2.03±0.10	59.7±2.2	0.62±0.04	16.6
4	0.540±0.006	2.71±0.35	61.4±1.7	0.90±0.08	24.1
N719	0.593±0.013	9.68±0.30	65.3±3.7	3.74±0.04	100.0

3.9 Conclusion

In this chapter, a new set of organic dyes (**1**-**4**), which were chosen based on the results of a data-mining study, was investigated for potential photovoltaic applications in DSSCs. **1**-**4** share a quinodimethane-based D-π-A-π-A_{ads} core structure but differ with respect to the anchor group (**1** and **3**: cyanoacrylic acid; **2** and **4**: carboxylic group) and donor moiety (**1** and **2**: NMe_2; **3** and **4**: NPh_2).

The structures of **1**-**4** were initially optimized, before the HOMO/LUMO levels were determined experimentally (CV) and theoretically (DFT). The combined results revealed strong ICT processes for all dyes and well-suited HOMO/LUMO energies relative to the CB of TiO_2 and the I^-/I_3^- redox potential, which ensures sufficient electron injection and dye regeneration in DSSC devices. Electrochemical impedance spectroscopy revealed thatelectron recombination at TiO_2/dye/electrolyte interfaces could be effectively suppressed by the steric effect of the diphenylamino groups for **3** and **4**. .

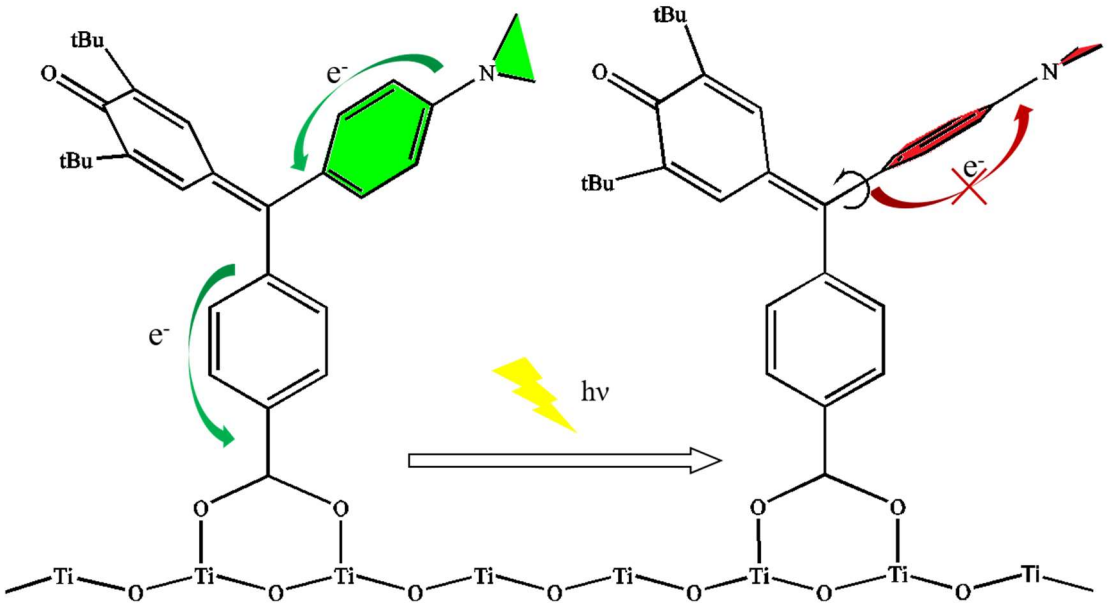

Figure 3.16. Schematic illustration of the performance of **2** under illumination.

DFT and TD-DFT methods provided an insight into the electronic and geometric structures of 1-4 and their adsorption modes on the TiO_2 surfaces. Theoretical

calculations on the ES of **1-4** have shown that a twist of the dialkylamino-phenyl moiety explains the Stokes shifts observed in the emission spectra of **1-4**. Moreover, it has been found that the dialkylamino-phenyl moiety in **2** exhibits the largest torsional change upon photoexcitation, and that the extent of this twist in these dyes follows the order, **2** > **1** > **4** > **3**. DSSC device photovoltaic performance tests supported this anticipated structural change and revealed a direct relationship between this photo-induced torsional change and photovoltaic output. DSSC devices sensitized with **2** furnished the highest open-circuit voltage (0.54 V) and power conversion efficiency (30% of that of **N719**) among **1-4**, which is due to the diminished back-electron transfer from the acceptor to the donor as a result of the large torsional change in its dialkylamino-phenyl moiety. Moreover, the short-circuit current density, Jsc, values track the same order, **2** > **1** > **4** > **3**, observed for the dihedral angle. This discovered structure-property relationship, which may be classified as twisted intramolecular charge transfer (TICT), [84] can now be exploited to create larger chromophores in this class of dyes which exhibit superior photovoltaic performance with good dye regeneration characteristics while precluding undesirable electron recombination by incorporating this diode-like effect as a knowledge-based rule within the molecular engineering strategy for these dyes.

Chapter 4

Functionalized Carbazole Dyes (MK series)

4.1 Introduction

The MK series of dyes is a class of alkyl-functionalized carbazole dyes, which were reported for the first time in 2006.[16] Subsequently, systematic studies on their molecular structures,[85] electrolyte effects,[86] and their long-term stability in devices[87] have been reported. MK dyes exhibit a typical D-π-A structure with a carbazole electron donor (D), a cyanoacrylic acid electron acceptor (A) / anchor, and oligothiophene (or alkyl-substituted oligothiophenes) π-bridges.

MK-44, i.e., *2-cyano-3-(5-(9-ethyl-9H-carbazol-3-yl) thiophen-2-yl) acrylic acid* (Figure 4.1) represents the simplest MK dye, as it contains only one unsubstituted oligothiophene. **MK-2**, i.e., *2-cyano-3-[5'''-(9-ethyl-9H-carbazol-3-yl)-3', 3'', 3''', 4-tetra-n-hexyl-[2, 2', 5', 2'', 5'', 2''']-quarter-thiophen-5-yl] acrylic acid* (Figure 4.2) is structurally a little more complex, as it contains a *n*-hexyl-substituted quarter-thiophene, which allows to effectively control the dye loading and/or aggregation thickness on TiO_2 surfaces. Notably, in DSSCs under standard conditions, the use of

MK-2 results in a competitive power conversion efficiency (PCE, η) of 8.3%.[85]

For these MK dyes, different redox couples such as I^-/I^{3-},[16, 85-87] $Co^{+2/+3}$,[88] and $Fe^{+2/+3}$ complexes[89] were designed to optimize dye regeneration.

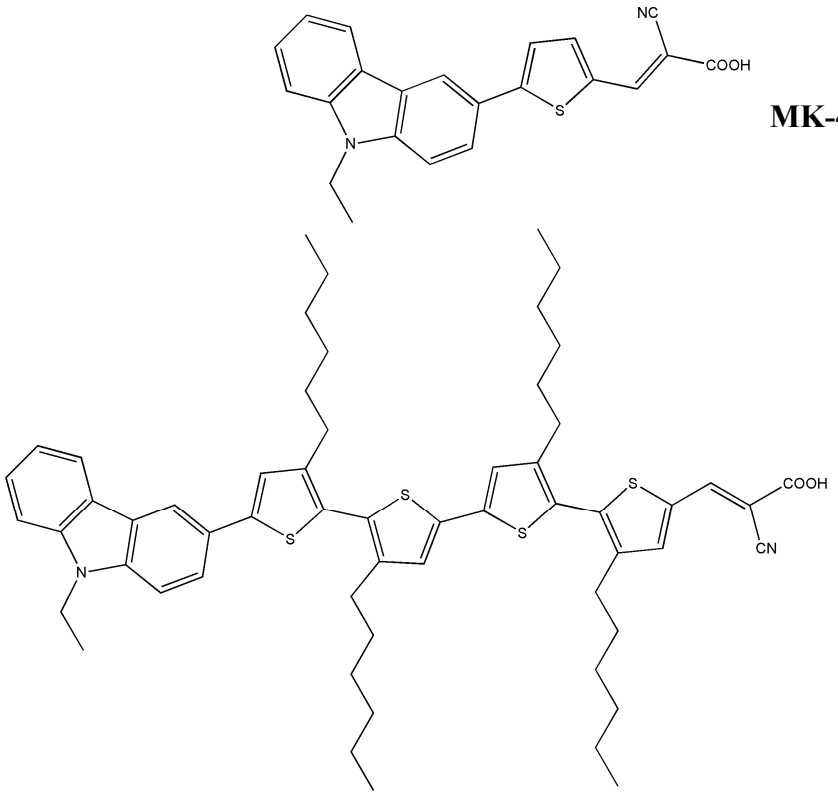

MK-44

MK-2

Figure 4.1 Chemical structures of **MK-44** and **MK-2**.

In order to obtain a better understanding of the structure-property relationships of the MK dyes, especially with respect to the relationship between well-performing MK sensitizers such as **MK-2** and the basic building blocks, computational methods including density functional theory (DFT) and time-dependent (TD) DFT methods

will be used in this chapter. Given the structural complexity of **MK-2**, the theoretical investigations, with a focus on molecular structure and adsorption properties, were conducted on **MK-44** in the interest of maximizing computational results while concomitantly minimizing computational costs and time. Considering the structural similarities between **MK-44** and **MK-2**, the results for **MK-44** should be transferrable to **MK-2**. Samples of **MK-44** and **MK-2** were synthesized in the group of Prof. Kawase at Osaka University (Japan). All the X-ray diffraction and X-ray refraction results of **MK-44** and **MK-2** in this chapter were measured by Dr. Jacqueline M Cole and her colleagues.

4.2 Methods and materials

4.2.1 Experimental details

UV/vis absorption spectra of **MK-44** or **MK-2** in a mixture of acetonitrile, *t*-butanol, and toluene (1:1:1, v/v), as well as of **MK-44**/TiO_2 and **MK-2**/TiO_2 nanocomposites were recorded on an Agilent8453 Diode Array spectrophotometer (resolution: 2 nm). Emission spectra of **MK-44** and **MK-2** in the same solvent mixture were determined using a Cary Eclipse fluorescence spectrophotometer with a 20 nm excitation/emission slits.

TiO_2 (DSL 18NR-T, Dyesol) photoanodes (thickness: ~4 μm) were generated on well-cleaned FTO glass (Dyesol, TEC-15) using the doctor-blade technique, interspersed by drying. The resulting electrodes were sintered at 500 ºC for 30 min. All photoanodes were subsequently immersed overnight in a mixture of acetonitrile, *t*-butanol, and toluene (1:1:1, v/v) containing 5×10^{-5} M of **MK-44** or **MK-2**.

4.2.2 Computational details

Isolated dye structures were optimized using the Gaussian 09 software package[90] at the B3LYP[59]/6-31g(d)[71] level of theory, both for vacuum structures and those in methanolic solution (polarizable continuum model, PCM;[72] $\varepsilon_{MeOH} = 32.63$[90]). To simulate the interface between the dye molecules and the TiO_2 nanoparticles, the optimized gas-phase structures of the dye molecules were initially absorbed onto a $(TiO_2)_9$ cluster,[73] as this offers a feasible balance between scientific accuracy and computational costs. The geometries of the adsorbed dye molecules were optimized at the same level of theory. All geometrically optimized structures were checked by subsequent vibrational-frequency calculations at the same level of theory; single-point-energy calculations were performed at the B3LYP/6-31g++(d, p) level of theory for the isolated dyes and at the B3LYP/6-31g(d) level of theory for the absorbed dyes. Several adsorption modes are possible for cyanoacrylic and carboxylic acid groups on TiO_2 nanoparticles. In general, the bidentate bridging (BB) anchoring mode is considered more stable for **MK-2** than other anchoring modes for similar interfaces.[40, 74, 91] For **MK-44**, the COO/CN (A2) anchoring mode is the most stable, albeit that the A2 mode is only slightly more stable than the BB mode ($\Delta E = 0.2$ eV).[83] Theoretical UV/vis absorption spectra were calculated using TDDFT methods in methanol (PCM) based on 6-31g(d) and 6-31++G(d,p) basis sets with different functionals (B3LYP, CAM-B3LYP,[60] wB97X ,[92] wB97XD,[93] LC-BLYP,[59b, 94] LC-PBEPBE,[94-95] LC-wPBE,[96] LSDA,[97] B3PW91,[57, 59a] mPW1PW91,[98] PBEPBE, [95] HSEH1PBE,[99] HCTH,[100] TPSSTPSS,[101] and M062X[61a]). For **MK-2**, TDDFT calculations were carried out at the M062X/6-31g(d) level of theory using the PCM model.

To investigate the effect of Li^+ on the adsorption mode of **MK-44** on TiO_2 surface, electronic-structure calculations for the Li···dye···TiO_2 interface were performed for the A2 and BB adsorption modes with different connections to Li^+ ions (via O atom and N atom respectively) . The structure and energy of the A2 and BB adsorption modes were calculated with and without surrounding Li^+ ions. Geometry optimizations were carried out at the B3LYP/3-21G* level of theory. Frequency calculations were conducted in order to confirm that the optimized geometric structures represent minimum energies at same level of theory.

In Section 4.8, the structures and associated energy levels of free **MK-44** molecules and TiO_2-adsorbed **MK-44** molecules were calculated using the NWChem.6.6 software package.[102] For free **MK-44**, gas-phase calculations were performed, optimizing the geometry at the B3LYP/6-31g(d) level of theory, before conducting a single-point-energy calculation with a property module at the same level of theory, forming a set of wave functions. Electronic structures of the dye···TiO_2 interfaces were calculated, modelling the dye on (101) surfaces of TiO_2, sampling two cluster sizes, $(TiO_2)_9$ and $(TiO_2)_{38}$.[103] The A2 anchoring mode was used to simulate the dye···TiO_2 interfaces. For the adsorbed dye molecules on the $(TiO_2)_9$ cluster, the geometries were optimized at the B3LYP/6-31g(d) level of theory, and single-point-energy calculations with a property module were performed at the same level of theory. For the adsorbed dye molecules on the $(TiO_2)_{38}$ cluster, the geometries were initially optimized at the B3LYP/STO-3G[104] level of theory, before single-point-energy calculations were carried out at the B3LYP/6-31g(d) level of theory. Atom-In-Molecule (AIM) analyses were carried out for all the models using the Multiwfn 3.3.9

software package.[82]

4.3 Geometry optimizations and analysis of the frontier molecular orbitals in MK-44 and MK-2

The optimized structures of **MK-44** and **MK-2** *in vacuo* are shown in Figure 4.2.

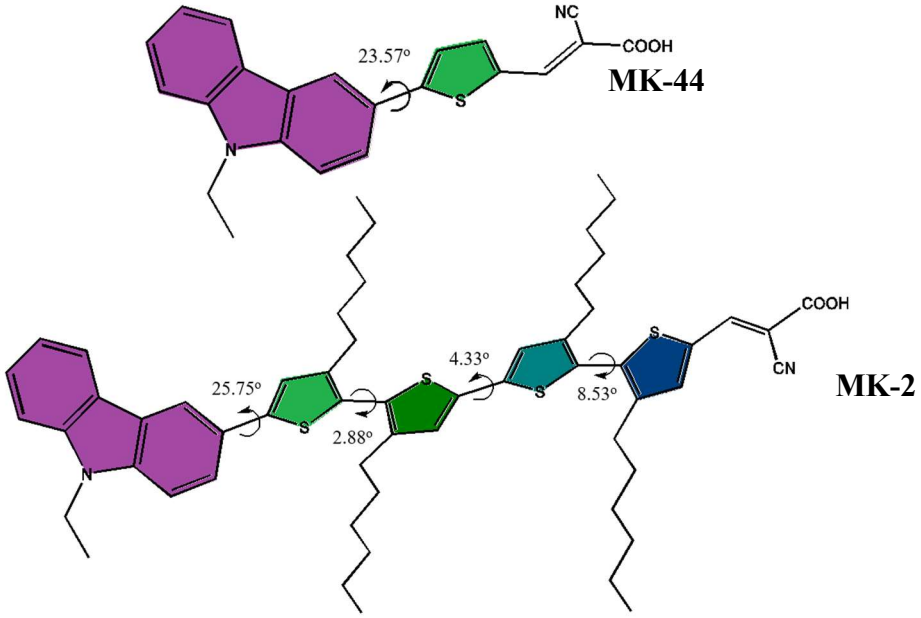

Figure 4.2 Rotation of the thiophene moieties in the *in-vacuo* structures of **MK-44** and **MK-2** optimized at the B3LYP/6-31g(d) level of theory.

The thiophene moieties connected to the carbazole unit in both **MK-44** and **MK-2** include dihedral angles of 23.57° and 25.75°, respectively. The dihedral angles relative to the adjacent thiophene units in **MK-2** decrease to 2.88°-8.53°. With a maximum dihedral angle of ~25° and sufficient rotational degrees of freedom, the carbazole and thiophene moieties should exhibit attractive levels of π–conjugation, especially in the

case of **MK-2**.

Based on the optimized structures, the molecular orbitals were calculated subsequently. For **MK-44**, the HOMO is distributed almost uniformly over the entire molecule, while the LUMO is located predominantly on the anchor group and the thiophene ring, albeit that smaller parts of the LUMO are still situated on the carbazole moiety. In **MK-2**, the HOMO is located on one phenyl ring of the carbazole group and the adjacent three thiophene rings. The LUMO is centered predominantly at the anchor group and the adjacent thiophene moiety.

Compared to **MK-44**, **MK-2** shows a much more pronounced intramolecular charge-transfer (ICT) character induced by the more extended π–conjugated area. The energy levels of the HOMOs and LUMOs for **MK-44** and **MK-2** are suitable for DSSC purposes, i.e., the HOMO levels are higher than the conduction band (CB) of TiO_2, which is important for electron injection, and the LUMO levels are lower than the potential of the I^-/I^{3-} redox electrolyte, which is important for dye regeneration. The more extended π–conjugation in **MK-2** relative to **MK-44** leads to a narrower band gap by raising the HOMO and lowering the LUMO level, which expands the absorption band of **MK-2**.

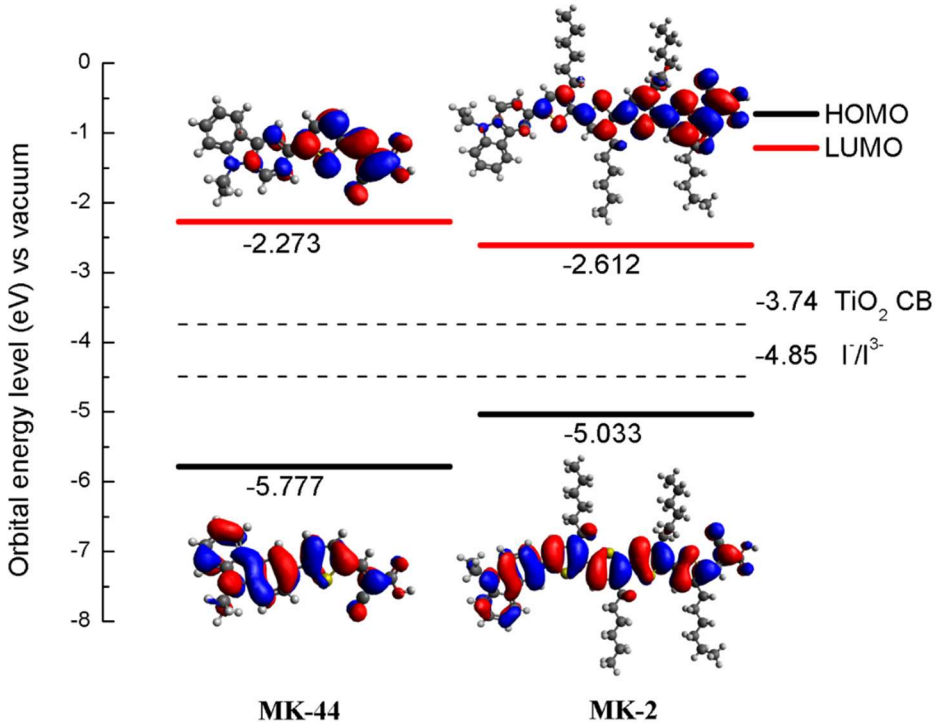

Figure 4.3 Frontier molecular orbitals for **MK-44** and **MK-2** *in vacuo* calculated at the B3LYP/6-31++G(d,p) level of theory.

4.4 UV/vis absorption and emission spectra in solution

The UV/vis absorption and emission spectra of **MK-44** and **MK-2** in a mixture of acetonitrile, *t*-butanol, and toluene (1:1:1, v/v) are shown in Figure 4.4.

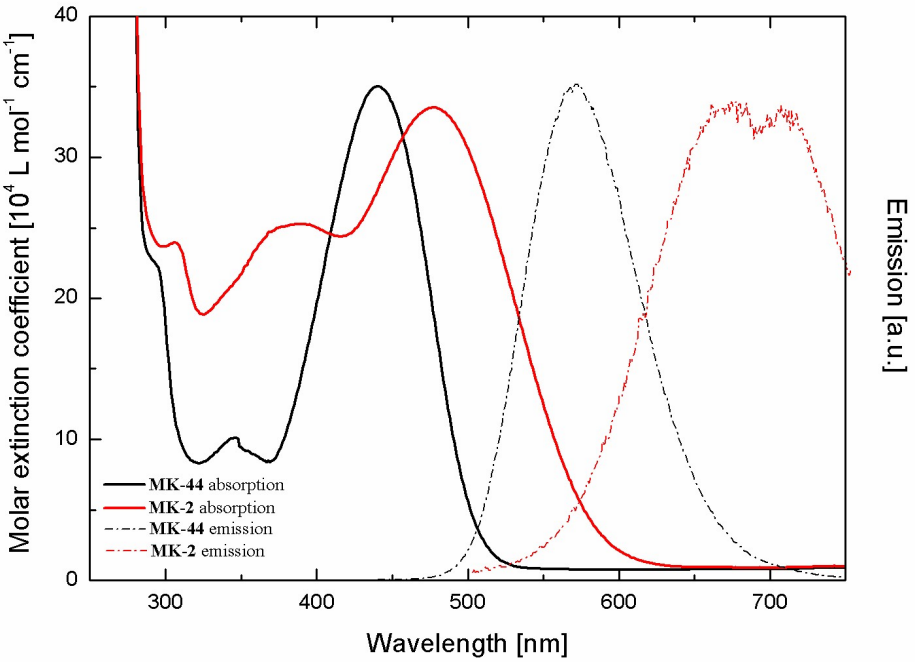

Figure 4.4 Absorption and emission spectra of **MK-44** and **MK-2** in a mixture of acetonitrile, *t*-butanol and toluene (1:1:1, v/v; [dyes] = 5×10^{-5} mol^{-1} L). For emission spectroscopy measurements, the same samples were employed and excited by exposure to light of 420 nm (**MK-44**) and 480 nm (**MK-2**).

In general, the two dyes exhibit similar features, whereby **MK-2** exhibits a stronger absorption in the shorter-wavelength region (300-400 nm) and a bathochromic shift of the edge of the longer-wavelength absorption band, probably induced by the extended π-bridge. The absorption bands at longer wavelengths (**MK-44**: 440 nm; **MK-2**: 477 nm) should be attributed to an ICT process in the dye molecules, while those at shorter wavelengths (**MK-2**: 389 nm; **MK-44**: 345 nm) should be assigned to the aromatic π–π* electronic transition of the conjugated thiophenes, which represents another piece of evidence that the extended π-conjugation improves the absorption properties of **MK-2**. In the emission spectra, the maxima of the emission peaks were observed at 571 nm (**MK-44**) and 671 nm (**MK-2**). The Stokes shift for **MK-2** (6061

cm^{-1}) is higher than that of **MK-44** (5214 cm^{-1}), indicating that this shift may be attributed to a structural reorganization by the rotation of the oligothiophene rings.

4.5 TD-DFT calculations on MK-44 and MK-2 in solution

To simulate the excitation processes of these MK dyes, TDDFT calculations were carried out on the optimized structures using different long-range functionals with 6-311++g(d,p) and 6-31g(d,p) basis sets and the PCM model. As it is difficult to simulate a mixture of three different solvents using the PCM, methanol was chosen as the solvent for the calculations, as: (i) its dielectric constant (32.7) is slightly smaller that of acetonitrile (37.5), (ii) the dielectric constant of toluene is negligible, and (iii) the balance between computational costs and accuracy of the results should be taken into account.

Table 4.1 First excitation energies for **MK-44** in methanol, calculated by TDDFT methods using different long-range functionals in combination with the 6-31g(d) basis set and the PCM model.

Functional	**Basis Set**	**First Excitation Energy**	
		eV	**nm**
B3LYP	6-311+g(d,p)	2.46	504.90
	6-31g(d,p)	2.52	491.10
CAM-B3LYP	6-311+g(d,p)	2.90	427.56
	6-31g(d,p)	2.99	414.09

wB97xd	6-311+g(d,p)	2.98	416.48
	6-31g(d,p)	3.06	405.02
wB97x	6-311+g(d,p)	3.08	401.94
	6-31g(d,p)	3.18	389.80
lc-blyp	6-311+g(d,p)	3.15	393.08
	6-31g(d,p)	3.27	379.60
lc-pbepbe	6-311+g(d,p)	3.20	387.76
	6-31g(d,p)	3.30	375.97
lc-wpbe	6-311+g(d,p)	3.15	393.79
	6-31g(d,p)	3.25	381.72
lsda	6-311+g(d,p)	1.98	626.44
	6-31g(d,p)	2.03	612.33
b3pw91	6-311+g(d,p)	2.47	501.48
	6-31g(d,p)	2.53	489.64
mpw1pw91	6-311+g(d,p)	2.57	482.18
	6-31g(d,p)	2.64	470.29
pbepbe	6-311+g(d,p)	2.00	620.46
	6-31g(d,p)	2.05	605.56
hseh1pbe	6-311+g(d,p)	2.45	505.28
	6-31g(d,p)	2.52	492.89
hcth	6-311+g(d,p)	2.01	618.19
	6-31g(d,p)	2.06	601.94
tpsstpss	6-311+g(d,p)	2.05	603.88
	6-31g(d,p)	2.10	590.78

m062x	6-311+g(d,p)	2.89	428.62
	6-31g(d,p)	2.98	416.16
Experimental result	-	2.84	437.0

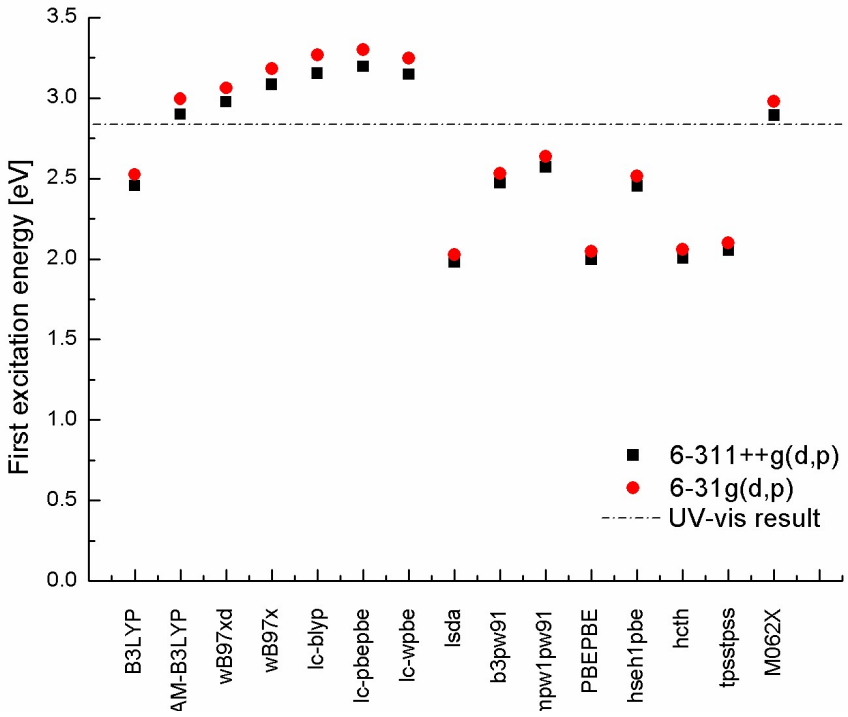

Figure 4.5 Comparison of the values of the calculated first excitation energies and the experimental results of the UV/vis measurements for **MK-44**.

Generally, for the valence excitation of singlets, with a larger percentage of the Hartree-Fock (HF) exchange functional, the calculations tend to underestimate the excitation energy. For example, PBE0 (25% long range), B3LYP (20% long range), or B3PW91 (20% long range) do not exhibit any obvious over- or underestimation of the excitation energy in terms of statistical results. Conversely, functionals such as CAM-B3LYP (65% long range), wB97XD (100% long range), or M062X (54% long range)

usually afford higher calculated excitation energies. However, for aromatic molecules with large-area π-conjugated structures, the percentage of the HF functional should be >25% to get a precise result, and accordingly, functionals with higher HF composition are suggested.[105] Figure 4.5 shows the experimental (UV/vis) and calculated first excitation energies for **MK-44** in methanol using different functionals and basis sets. A comparison to the experimental UV/vis result and to previous reports suggests that M062X (ΔE = 0.055 eV) and CAM-B3LYP (ΔE = 0.062eV) in combination with the 6-311++g(d,p) basis set afford the best agreement.[105] Based on these results, M062X was used for the calculations in the following sections.

The excitation energy of **MK-2** was calculated at the same level of theory and the UV/vis spectrum was measured under identical conditions. The energy difference between the experimental results and the results of the TDDFT calculations (ΔE = 0.266 eV) does not exceed 0.4 eV,[80] and thus indicates that this method is suitable for TDDFT calculations on **MK-2**.

Table 4.2. Experimental (UV/vis spectroscopy; MeCN : *t*-BuOH : toluene = 1:1:1 (v/v) and calculated (TDDFT; M062X/6-31g(d); PCM; MeOH) first excitation energy for **MK-2**.

MK-2	**Functional**	**Solvent**	First **excitation energy**
TD-DFT	M062X	methanol	2.325 eV (533.3 nm)
UV-vis result	-	acetonitrile, *t*-butanol, and toluene = 1:1:1 (v/v)	2.599 eV (477 nm)

4.6 Adsorption modes of MK-2 and MK-44 on TiO_2

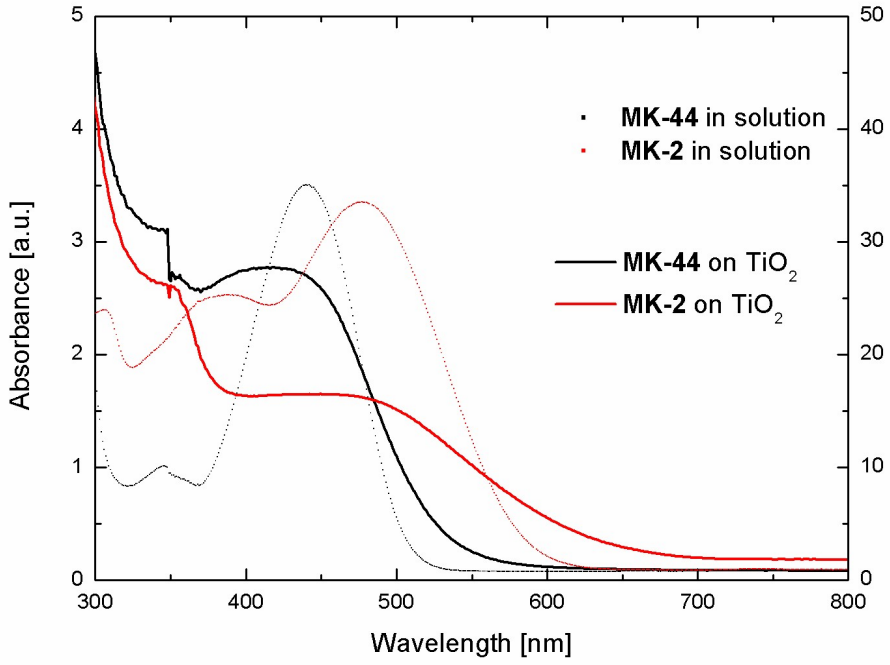

Figure 4.6 Absorption spectra of **MK-2** and **MK-44** adsorbed on thin films of TiO_2 (thickness: ~ 4 μm).

For **MK-2** in its deprotonated form, the bidentate bridging (BB) mode has been reported as the most probable binding mode for the adsorption on TiO_2 films.[40, 74, 91] The hypsochromic shift of the absorption peaks upon adsorption on TiO_2 furthermore indicates that the anchoring group binds in its deprotonated form (COO^-) at the dye···TiO_2 interface.[106] To further investigate the adsorption of **MK-2**, the dye···TiO_2 interface was optimized with different binding modes: bidentate chelating (B and BH; 'BH' represents the protonated form) and bidentate bridging (BB and BBH; 'BBH' represents the protonated form). Adsorption energy was defined as equation 3.1 in Chapter 3.

Table 4.3 Calculated adsorption energies for the different adsoption modes of **MK-2** on TiO_2 cluster.

Adsorption mode	Adsorption energy [eV]	ΔE^* [eV]
B	-1.650	0
BB	-1.031	0.620
BH	-0.963	0.963
BBH	-0.816	0.816

*: the energy of the B mode was chosen as the reference energy.

The B mode shows the lowest adsorption energy, which indicates that this mode is more stable than the other three. The calculated result is different from the previous study[40, 74, 91] that the bidentate bridging (BB) mode is the most probable binding mode for the adsorption on TiO_2 films. This discrepancy may be attributed to the size of the $(TiO_2)_9$ cluster, which is smaller than that of **MK-2** molecule (especially the long alkyl chain), and thus a larger TiO_2 cluster or a slab is needed to simulate the interface between **MK-2** and TiO_2 film.

Given the smaller size of **MK-44** relative to **MK-2** and the absence of long alkyl chains connected to the backbone, the situation regarding the adsorption modes of **MK-44** is more complicated than that of other MK dyes, especially compared to that of alkyl-functionalized MK dyes. Coordination of **MK-44** and **MK-2** to the Lewis-acidic Ti centers is possible via the O and N atoms. Meng has demonstrated that the COO/CN (A2) binding mode is energetically the most preferable adsorption mode for typical cyanoacrylic D-π-A dyes.[83] In this study, the two most favorable deprotonated

modes, i.e., A2 and BB were calculated with a $(TiO_2)_9$ cluster. The results of these calculations show that the A2 mode exhibits a slightly lower adsorption energy (-1.21 eV) than the BB mode (-1.02 eV), i.e., the BB mode is by 0.19 eV less stable than the A2 mode, which is consistent with the results of a similar study (0.2 eV).[83]

Table 4.4. Geometries of **MK44** on $(TiO_2)_9$ with different adsorption modes optimized at the B3LYP/6-31g(d) level of theory and corresponding adsorption energies.

Adsorption mode	Starting structure	Final structure	Adsorption energy [eV]	ΔE* [eV]
A2	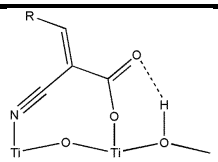	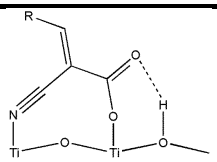	-1.21	0
BB	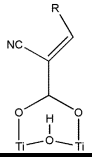	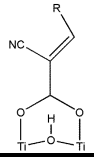	-1.02	0.19

*: the energy of the A2 mode was chosen as the reference energy.

4.7 The effect of Li^+ ions on the adsorption mode

To further study the interface between **MK-44** and TiO_2, X-ray reflectometry (XRR) experiments using different electrolytes (acetonitrile in the presence or absence of Li^+ ions) were conducted and revealed that after the immersion in a Li^+-containing electrolyte, the height of **MK-44** on TiO_2 changed from 9.2 Å to 15.9 Å, which corresponds to a binding mode change from A2 to BB.[83] In terms of energy, the A2 mode is slightly more preferable, but the adsorption energy is very close to that of the BB mode, which makes a binding-mode change between A2 and BB possible via

an environmental perturbation. To prove this change of binding modes, DFT methods were used to calculate the corresponding models.

To simulate the effect of the presence of Li^+ ions on the adsorption mode of **MK-44**, potential connections between the Li^+ ions and **MK-44** adsorbed on the TiO_2 cluster were examined, whereby Li···O and Li···N bonds were considered.[108] Accordingly, Li^+ cations were connected to the two O and the N atoms in the anchor group and examined for the A2 and BB binding modes. Thus, six different possible Li···dye ···TiO_2 models were calculated.

Table 4.5 DFT modelling of the Li···dye···TiO_2 moiety at the B3LYP/6-31g(d) level of theory.

Adsorption Mode	Starting Structure	Final Structure	Adsorption Energy[a] [eV]	ΔE[b] [eV]
CN/COO _Li_N	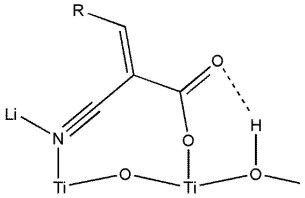	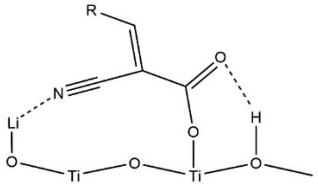	-3.14	0
BB_Li_N	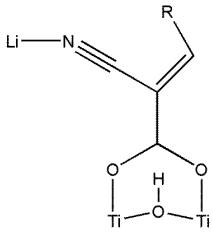	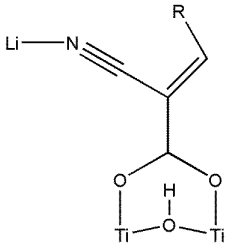	-2.53	0.60
CN/COO _Li_O_1	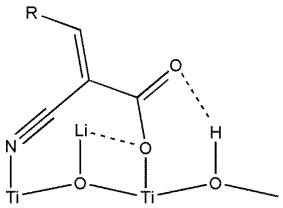	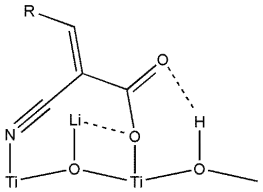	-3.15	-0.01
CN/COO _Li_O_2	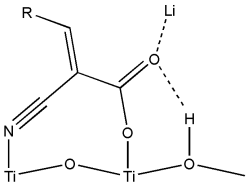	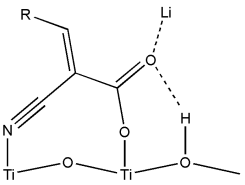	-2.40	0.73
BB_Li_O_1	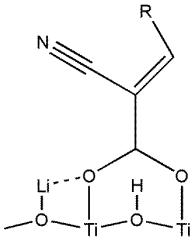	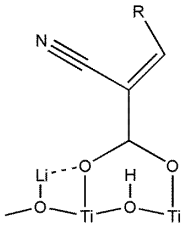	-3.44	-0.30
BB_Li_O_2	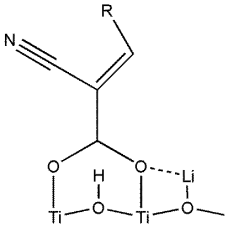	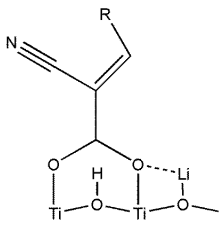	-2.68	0.45

a: $E_{ads} = E_{Li+\ldots dye\ldots TiO_2} - E_{dye\ldots TiO_2} - E_{Li}$

b: the energy of the CN/COO _Li_N mode was chosen as the reference energy.

The six computational models of the dye···TiO_2 interface structure in the presence of Li^+ ions are shown in Table 4.5. The lowest-energy model featured a Li···O interaction with a BB adsorption mode. Given that **MK-44** will be deprotonated in acetonitrile, the Li^+ ions should be attracted to the negative charge on the carboxylate moiety. These DFT results are consistent with the results obtained from XRR measurements on the **MK-44**···TiO_2 interface in solution containing Li^+ ions, as manifested by a much thicker dye-layer (15.9 ± 1.0 Å) compared to that in solution in the absence of Li^+ ions (9.2 Å).

In addition, it should be noted that for the Li···N connection in the A2 mode, the final structure is different from the starting structure with respect to the coordination of Li^+. During the geometry optimizations, Li^+ inserts into the N···Ti bond. This should represent a good starting point for future investigations on the details of how Li^+ can affect the adsorption on **MK-44**.

4.8 Intramolecular S···C≡N charge transfer

As **MK-44** represents the most basic building block of the MK dye series, its molecular and electronic structures were further investigated by single-crystal X-ray diffraction analysis. A charge density analysis based on the XRD results by Jacqueline Cole and her colleagues, suggests an intramolecular bonding of S···C≡N and then a potential second intramolecular charge-transfer pathway for **MK-44** from the S atom

in the thiophene ring to the C atom in the cyan group (Figure 4.7).[109]

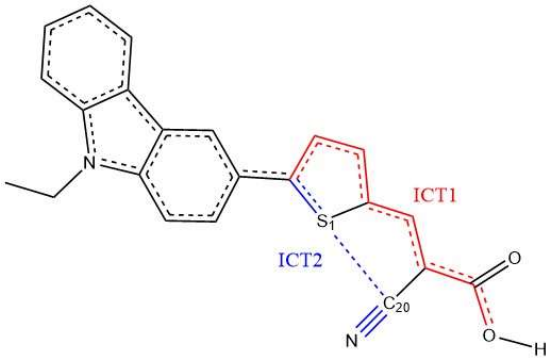

Figure 4.7 Two intramolecular charge-transfer pathways in **MK-44**.

To further prove the additional electron-transfer pathway in **MK-44** theoretically, a quantum-theory-of-atom-in-molecule (QTAIM) analysis was adopted based on the results of the DFT calculations.

The QTAIM, which was first developed by Richard Bader and his research group in at McMaster University, [110] describes all the basic concepts in a molecular system, such as atoms, molecules, chemical bonds, which are naturally expressed by the system's observable electron density distribution function.

In AIM theory, molecular systems are divided into subsystems (atoms). The topology of the electron density, $\rho(\mathbf{r})$, is used to define where one subsystem (atom) ends and the next begins. Each subsystem (atoms) is surrounded by a surface, through which the gradient vector field of $\rho(\mathbf{r})$ has no flux:

$$\nabla\rho(r) \cdot n(\mathbf{r}) = 0 \qquad \text{(eq 4.1)}$$

where, $\nabla\rho(\mathbf{r})$ is the gradient of the electron density and $n(\mathbf{r})$ is a unit vector normal to the surface. And at certain points, called critical points (CP), the gradient vanishes. A bond critical point (BCP) is one of the CPs to define a chemical bond between two neighboring atoms. The BCP is a saddle point of electron density with a maximum in

two directions of space, that electron density falls down in two perpendicular directions of space, and a minimum in the third direction, that electron density rises in the third direction.

4.8.1 Bond-critical points (BCP) for free and adsorbed MK-44

To examine any potential chemical bonds between the S1 and C20 atoms in **MK-44**, **MK-44** was initially studied in the gas phase by DFT calculations and a quantum-theory-of-atoms-in-molecules (QTAIM) analysis (Figure 4.8).

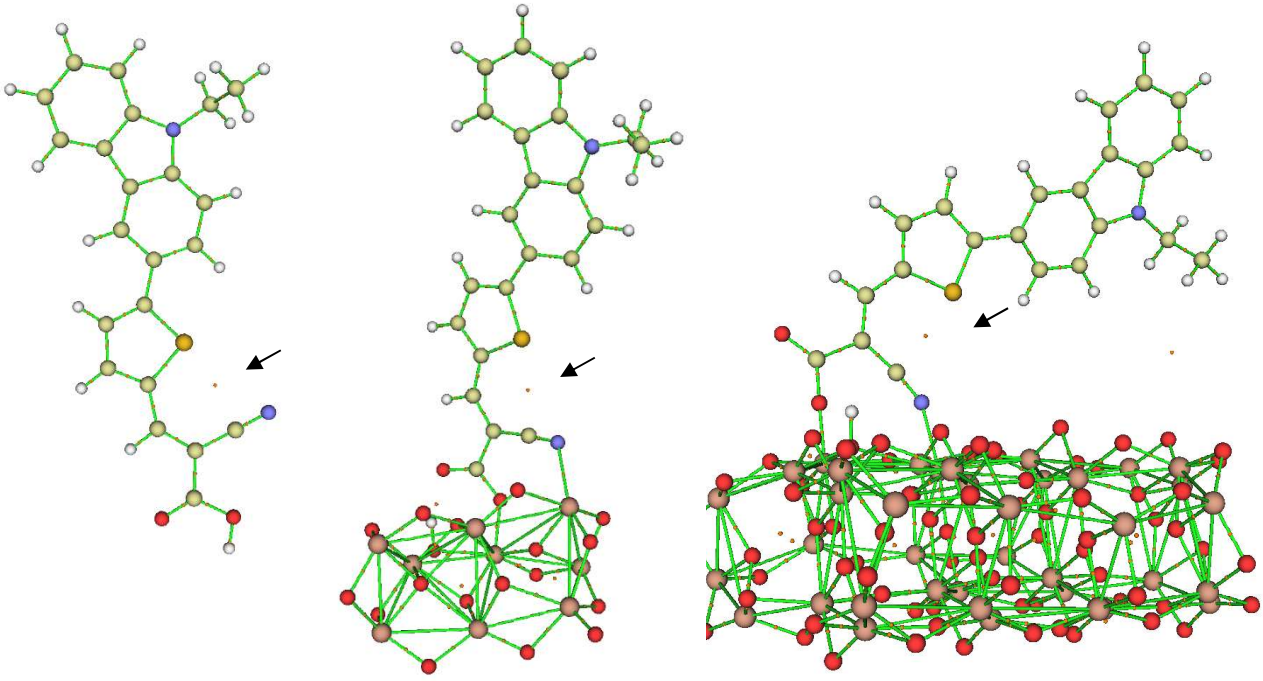

(a) **(b)** **(c)**

Figure 4.8 Bond-critical points for (a) free **MK-44**, (b) **MK-44** adsorbed on $(TiO_2)_9$, and (c) **MK-44** adsorbed on $(TiO_2)_{38}$; all calculated at the B3LYP/6-31g(d) level of theory. The BCP between S1 and C20 atoms in all the three models were pointed by the black arrows.

All BCPs in Figure 4.8 are located between the S1 and C20 atoms (arrows), which represents strong evidence for the existence of an intramolecular chemical bond between S1 and C20 that would thus support the presence of an additional electron-transfer pathway.

MK-44 adsorbed on TiO_2 via the A2 binding mode was also investigated by DFT calculations and a QTAIM analysis. To simulate the dye···TiO_2 interface more precisely, $(TiO_2)_9$ and $(TiO_2)_{38}$ were used in these calculations. The results of these calculations show that after anchoring on the surface of TiO_2 via N···Ti and O···Ti bonds, the BCP between S1 and C20 still exists, which indicates that the intramolecular bond was not broken upon adsorption and even promoted the formation of the A2 binding mode, in which the additional electron-transfer pathway can be constructed between the TiO_2 surface and the donor of **MK-44**.

4.8.2 Density of states (DOS) for free and adsorbed MK-44

To further interpret the effect of the adsorption of **MK-44** on its intramolecular charge transfer, the density of states (DOS) of adsorbed **MK-44** was calculated. The total DOS (TDOS) and partial DOS (pDOS) are shown in Figure 4.9.

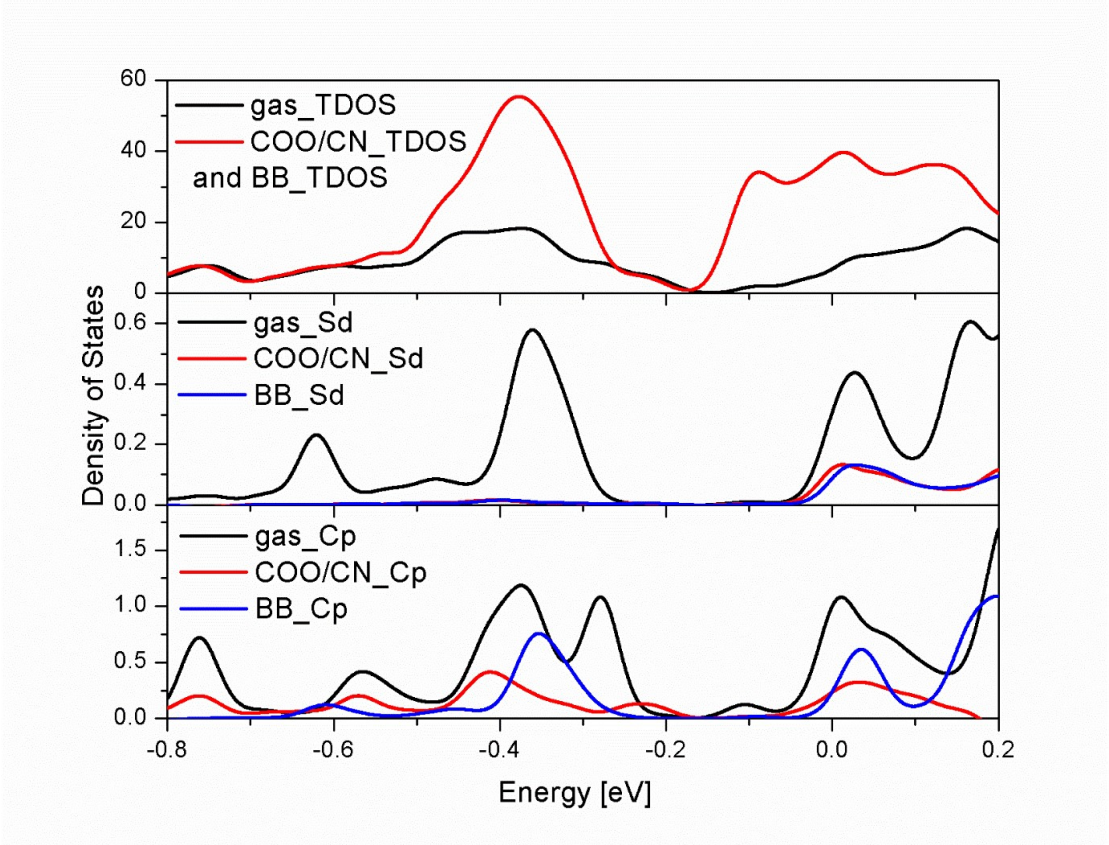

Figure 4.9: Density of states (DOS) plots for **MK-44** in the gas phase (black) and for **MK-44** adsorbed onto TiO_2 via an A2 (red) or BB (blue) dye anchoring configuration. The top plot shows the TDOS; the middle and bottom plots display the pDOS distributions of 3d orbital of S atom (Sd) and 2p orbital of C atom (Cp), respectively.

These plots display a large overlap between the Sd and Cp orbitals for the gas-phase model of **MK-44**, confirming the existence of the experimentally observed S1···C20 bond.[109] These plots also show a small yet noticeable overlap of the Sd contribution with the Cp orbitals upon adsorption of **MK-44** onto TiO_2 via either the A2 or BB binding mode. The calculated TDOS contribution of the A2 and BB binding modes are indistinguishable, and thus, the red curve represents the DOS of both modes. The associated PDOS contributions show very small differences, which are mostly located in the antibonding region. In these plots, the Sd and Cp pDOS overlap

appears very subtly in the models of the dye···TiO_2 interface. This should be due to not only the cluster model, but also to the method that was used to obtain the DOS by expanding local to periodic wave-functions, which is somewhat limited. Thus, the conclusions drawn from the current computational results remain preliminary and have to be considered with caution. For more reliable results, a substantially better model must be developed, even though that may require significantly more extensive and complex calculations.

4.9 Conclusions

In this chapter, **MK-44**, i.e., the basic building block for the MK dye series, was systematically studied by UV/vis spectroscopy and DFT calculations, and compared to **MK-2**, which contains an extended π-bridge with long alkyl chains. The UV/vis spectra of **MK-44** showed that a shorter π-bridge results in a lower absorption at shorter wavelength and a narrower absorption peak at longer wavelength compared to **MK-2**. In the absence of long alkyl substituents, the anchoring of **MK-44** is more complex than that of **MK-2**. The results of DFT calculations showed that the COO/CN (A2) anchoring mode is only slightly more stable than bidentate bridging (BB) mode ($\Delta E = 0.19$ eV). In the presence of Li^+ ions, the computational results for **MK-44** adsorbed in A2 or BB mode show that the BB mode with Li···O bond is the most stable among the six possible Li···dye···TiO_2 models that were examined. Moreover, these results are consistent with the results of X-ray reflectometry (XRR) measurements, which suggest that the adsorption mode of **MK-44** changes from A2 to BB in the presence of Li^+ ions.

A single-crystal X-ray diffraction analysis revealed that **MK-44** contains an additional charge-transfer pathway between the sulfur atom of the thiophene ring and the carbon atom of the cyano group. This pathway and the S···C≡N bond were also reproduced by DFT calculations. Bond-critical points (BCPs) were calculated for free **MK-44** and for **MK-44** adsorbed on $(TiO_2)_9$ and $(TiO_2)_{38}$ clusters. The results of these calculations indicated the existence of BCPs between S1 and C20, which represents a strong piece of evidence for the presence of an S···C≡N bond. Calculations of the density of states (DOS) were used to interpret this chemical bond and showed an overlap between the Sp and Cd orbitals only for the free molecule, which is points towards the existence of the S···C≡N bond.

Chapter 5

The Benzothiadiazole-based Dye RK-1

5.1 Introduction

The recently reported benzothiadiazole-based organic dye 2-cyano-3-(4-(7-(5-(4-(diphenylamino)phenyl)-4-octylthiophen-2-yl)benzo[*c*][1,2,5]thiadiazol-4-yl)phenyl) acrylic acid (**RK-1**) exhibits an energy-conversion efficiency of 10.20%, which is comparable to that of **N719** (10.19%) under identical conditions.[34] Moreover, devices containing **RK-1** show an excellent stability after 2200 h at 65 ºC under standard irradiation conditions.[34] To further develop the performance of **RK-1**, derivatives that contain different anchor groups and substituents at the *para* position of the triphenylamine moiety were synthesized to be used in ZnO-based dye-sensitized solar cells (DSSCs). The results showed that **RK1**-based dyes generally performed very well with ZnO photoanodes.[111] However, despite the promising potential of **RK1**, only few systematic investigations, especially on the **RK-1**$\cdots TiO_2$ interface, have been carried out. Thus, in this chapter, the optical and electrochemical properties of **RK-1** and the **RK-1**$\cdots TiO_2$ interface were investigated experimentally and computationally.

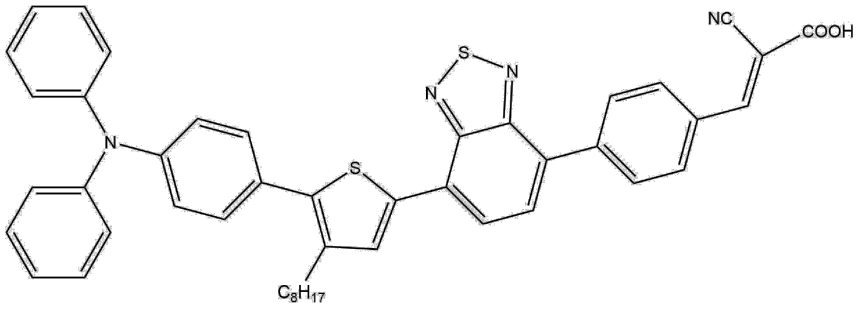

Figure 5.1. Chemical structure of **RK-1**.

5.2 Methods and materials

5.2.1 Experimental details

Ultraviolet-visible (UV/vis) absorption spectra of **RK-1** in solution (acetonitrile) and of **RK-1**/TiO_2 nanocomposites were recorded on an Agilent8453 Diode Array spectrophotometer with a resolution of 2 nm.

TiO_2 (DSL 18NR-T, Dyesol) photoanodes (thickness: ~ 4 μm) were generated on well-cleaned FTO glass (Dyesol, TEC-15) using the doctor-blade technique, interspersed by drying. The resulting electrodes were sintered at 500 ºC for 30 min. All photoanodes were subsequently immersed overnight in an acetonitrile solution of **RK-1** ([**RK-1**] = 6×10^{-5} M).

Electrochemical impedance spectroscopy (EIS) measurements were carried out using an Autolab PGSTAT electrochemical workstation (frequency range: 10 mHz to 100 kHz). The amplitude of the modulated signal was 10 mV. The tested samples were sealed devices with active area of 1.0 cm^2.

5.2.2 Computational details

Isolated dye structures were optimized using the Gaussian 09 software package[90] at the B3LYP[59]/6-31g(d)[71] level of theory, both for vacuum structures and those in acetonitrile solution (polarizable continuum model, PCM[72]; $\varepsilon_{MeCN} = 35.688$[90]). To simulate the interface between the dye molecules and the TiO_2 nanoparticles, the optimized gas-phase structures of the dye molecules were initially absorbed onto a $(TiO_2)_9$ cluster,[73] which offers a feasible balance between scientific accuracy and computational costs. The geometries of the adsorbed dye molecules were optimized at the same level of theory. All geometrically optimized structures were checked by subsequent vibrational frequency calculations at the same level of theory; single-point energy calculations were performed at the B3LYP/6-31g++(d, p) level of theory for the isolated dyes and at the B3LYP/6-31g(d) level of theory for the absorbed dyes. For the adsorption of cyanoacrylic and carboxylic acid groups onto TiO_2 nanoparticles, two adsorption modes, i.e., the bidentate bridging (BB) and the COO/CN (A2) anchoring mode, are possible and were considered in the calculations. Theoretical UV/vis absorption spectra were calculated using time-dependent density functional theory (TDDFT) methods in acetonitrile (PCM) based on different functionals (B3LYP,[59] CAM-B3LYP,[60] wB97XD,[93] and M062X[61a]) with the 6-31g(d) basis set.

5.3 Geometry optimizations for RK-1 and analysis of its frontier molecular orbitals

The optimized structure of **RK-1** *in vacuo* is shown in Figure 5.2.

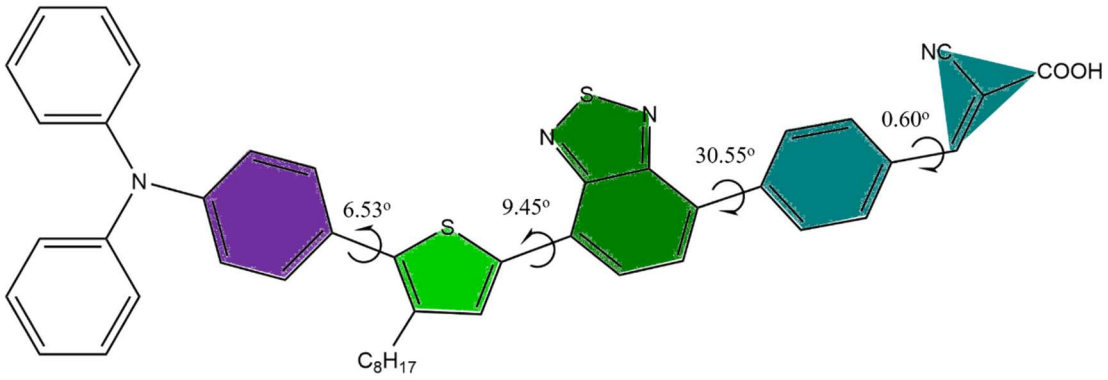

Figure 5.2 Deviations of the thiophene, benzothiadiazole, and benzene moieties of **RK-1** from co-planarity; optimized at the B3LYP/6-31g(d) level of theory *in vacuo*.

Figure 5.2 shows the optimized geometry for **RK-1**, which includes a deviation of the thiophene, benzothiadiazole, and benzene rings from a co-planar arrangement. The dihedral angles between the triphenylamine and the thiophene and between the thiophene and benzothiadiazole moieties are 6.53º and 9.45º, respectively. Considering these relatively modest deviations from co-planarity the triphenylamine-thiophene-benzothiadiazole moiety should be able to act as an excellent π–conjugated structure for the electron-donor part of **RK-1**. Moreover, the dihedral angle between the benzene moiety and the cyanoacrylic acid group is also very low (0.60º), which should render the acceptor part almost co-planar. Therefore, an excellent π–conjugation, and a concomitantly efficient electron injection should be expected upon adsorption onto TiO_2. However, it should also be noted that the dihedral angle between the benzothiadiazole ring and the adjacent benzene ring is 30.55º, which

decreases the π–conjugation of the entire molecule.

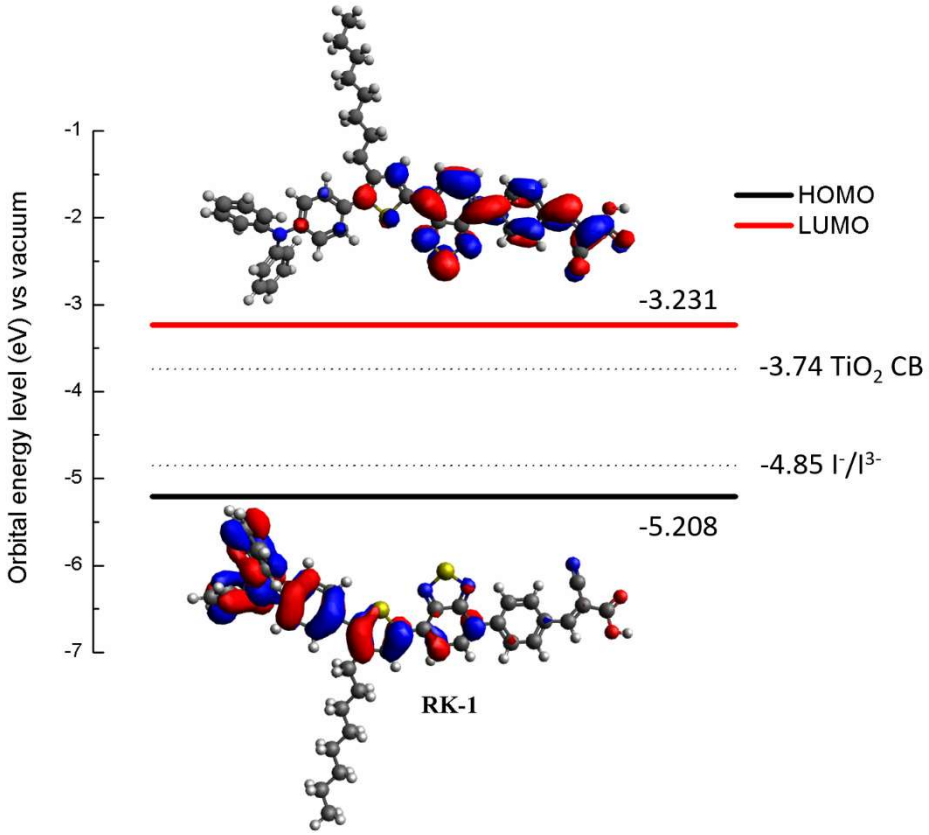

Figure 5.3 Frontier molecular orbitals for **RK-1** calculated at the B3LYP/6-31++g(d,p) level of theory *in vacuo*.

The molecular orbitals were calculated based on the optimized structures *in vacuo*. As shown in Figure 5.3, the highest occupied molecular orbital (HOMO) is situated on the triphenylamine moiety and the following thiophene ring, while the lowest unoccupied molecular orbital (LUMO) is located on the benzothiadiazole and benzene rings, as well as on the cyanoacrylic acid group. An intramolecular charge transfer (ICT) is induced by the large π–conjugated area. The HOMO and LUMO energy levels for **RK-1** are suitable for applications in DSSCs, as the energy of the LUMO level is higher than that of the conduction band (CB) of TiO_2, which is required for the injection of electrons, and as the LUMO level is lower than the potential of the I^-

/I^{3-} redox couple, which is required for the regeneration of the dye molecules. Moreover, neither the HOMO nor the LUMO are located on the alkyl chain, which means that the $–C_8H_{17}$ group has no effect on the electronic structure, and only serves as a means to reduce dye aggregation.

5.4 UV/vis and emission spectra of RK-1

5.4.1 UV/vis spectra of RK-1 in acetonitrile solution and adsorbed on TiO_2 films

The UV/vis absorption and emission spectrum of **RK-1** in acetonitrile is shown in Figure 5.4.

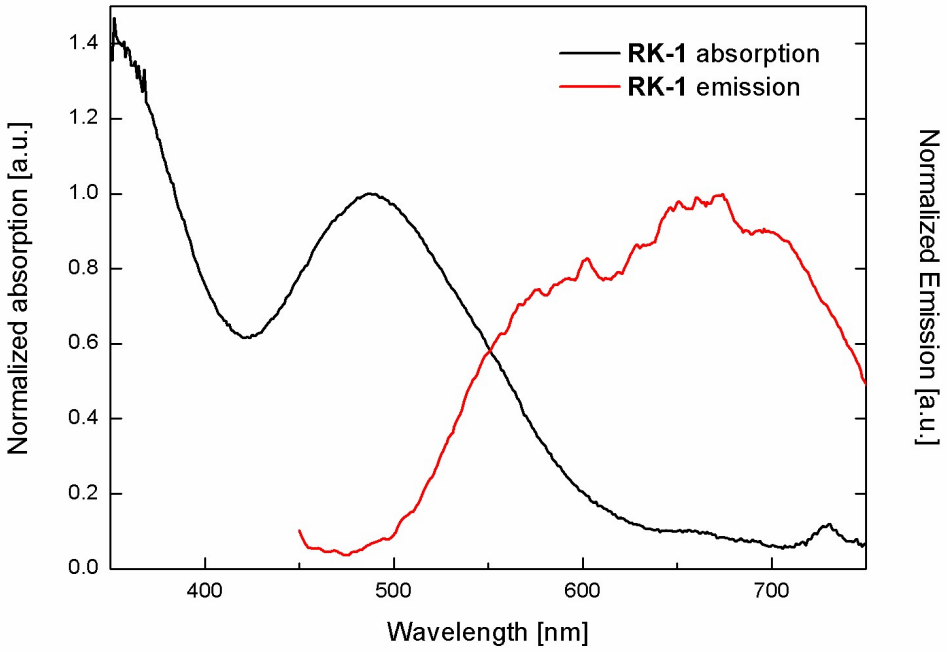

Figure 5.4 Absorption and emission spectra of **RK-1** in acetonitrile ([**RK-1**] = 6×10^{-5} mol^{-1} L). For emission spectroscopy measurements, the same samples were employed and excited by exposure to light of λ_{ex} = 440 nm.

Figure 5.4 exhibits two absorption bands for **RK-1** in acetonitrile at ~350 nm and at 450-550 nm. The absorption band at longer wavelength (λ_{max} = 490 nm) should be attributed to an ICT process in the dye molecules, while that at shorter wavelength (λ_{max} = 472 nm) should be assigned to the aromatic π–π* electronic transition of the conjugated thiophene and benzothiadiazole rings. In the emission spectrum, the maximum of the emission peak was observed at 674 nm with a Stokes shift of 5571 cm^{-1}, indicating that this shift may be attributed to a structural reorganization via a rotation of the rings in the π-bridge. It is also noticeable that there are at least one peak in the middle and two shoulders in the emission band, which may be attributed to different processes of structural reorganization. The geometry of **RK-1** in the excited state is discussed in Section 5.5.2.

5.4.2 Concentration-dependent UV/vis spectra of RK-1 in acetonitrile

Given that DSSC dyes commonly suffer from aggregation, it may be possible that **RK-1** also aggregates in solution or when adsorbed on TiO_2, which may lead to a bathochromic or hypsochromic shift of the UV/vis absorption spectrum. The UV/vis absorption peaks of **RK-1** in acetonitrile at different concentrations ([**1**] = c_0 = 6 × 10^{-5} mol L^{-1}, [**2**] = c_0/2 = 3 × 10^{-5} mol L^{-1}, [**3**] = c_0/4 = 1.5 × 10^{-5} mol L^{-1}, [**4**] = c_0/8 = 7.5 × 10^{-6} mol L^{-1}, [**5**] = c_0/16 = 3.75 × 10^{-6} mol L^{-1}) are summarized in Table 5.1.

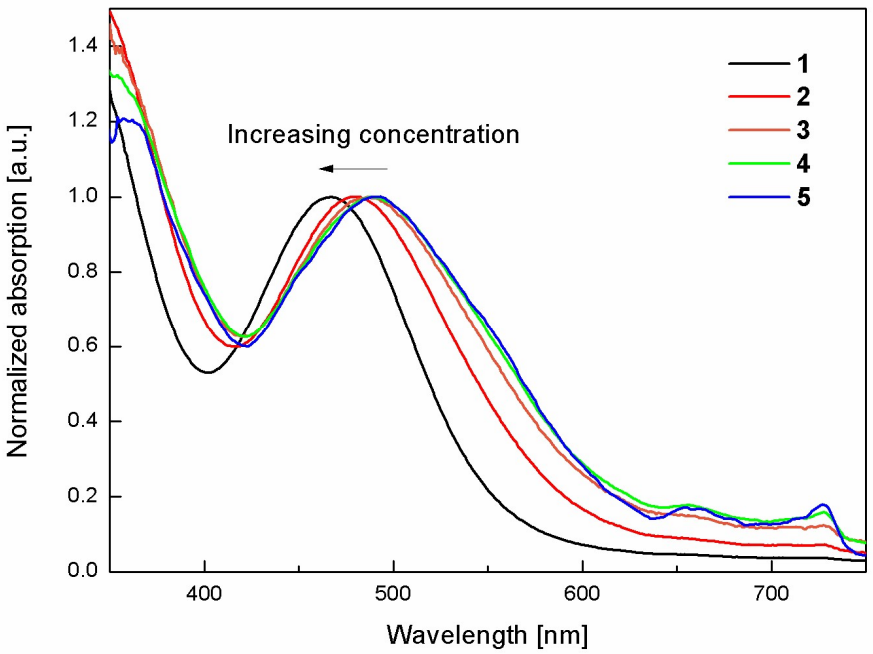

Figure 5.5 Concentration-dependent absorption spectra of **RK-1** in acetonitrile ([**1**] = $c_0 = 6.0 \times 10^{-5}$ mol L^{-1}, [**x**] = $c_0 / 2^{x-1}$).

Table 5.1. The concentration-dependent UV/vis absorption peaks of **RK-1** in acetonitrile solution.

Sample	$\lambda_{max,abs}$ [nm]
1	467
2	479
3	487
4	490
5	490

The absorption peaks of **RK-1** are subject to a hypsochromic shift (490 → 467 nm) upon increasing the concentration, which is consistent with H-aggregation.[112] The

absorption peaks of **4** and **5** are identical, which suggests that **RK-1** exist as a monomer in acetonitrile for concentrations < 7.5×10^{-6} mol L^{-1}.

5.5 TDDFT calculations on RK-1

5.5.1 TDDFT calculations on RK-1 in acetonitrile

To simulate the excitation processes of **RK-1**, TDDFT calculations on its optimized structure were carried out employing different long-range functionals. A summary of the results of these calculations is shown in Table 5.2.

Table 5.2 First excitation energies for **RK-1** in acetonitrile, calculated by TDDFT methods using different long-range functionals in combination with the 6-31g(d) basis set and the PCM model (experimental value given for comparison).

Functional	**First excitation energy**	
	eV	**nm**
B3LYP	1.84	674.80
CAM-B3LYP	2.69	460.51
wB97XD	2.80	442.53
M062X	2.68	461.79
Experimental result	2.53	490

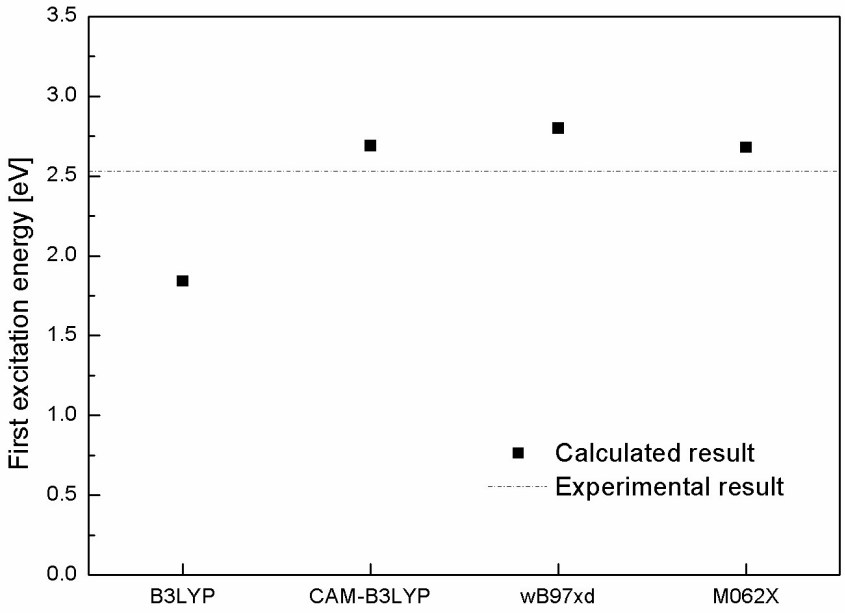

Figure 5.6 Comparison of the values of the calculated first excitation energies for **RK-1** and the experimental results obtained from UV/vis measurements.

For aromatic molecules with extended π-conjugated structures (*cf.* Section 4.5), the percentage of the HF functional should be >25% to get a precise result, and accordingly the use of functionals with higher HF compositions has been recommended.[105] Figure 5.6 shows the experimental UV/vis absorption peaks and the TDDFT-calculated first excitation energies for **RK-1** in methanol using different long-range functionals. A comparison between the experimental and theoretical results suggests that M062X (ΔE = 0.15 eV) and CAM-B3LYP (ΔE = 0.16 eV) afford the best agreement with the experimental results. Based on these results, M062X was used for the subsequent TDDFT calculations presented in this chapter.

Table 5.3 Energy (eV, nm) and oscillator strength values for **RK-1**, as well as sizable (f > 0.1) contributions of the molecular orbitals to the corresponding transitions.

ES (*n*)	First excitation energy		Oscillator strength (*f*)	Composition	
	[eV]	[nm]			
1	2.685	461.79	1.3586	59.22%	HOMO – LUMO
4	4.0345	307.31	0.8638	68.43%	HOMO – LUMO+2

The contributions from the transitions between molecular orbitals to the first excitation energy values were also calculated (Table 5.3), and the results show that the ICT absorption bands should be attributed predominantly to the HOMO–LUMO transition. The calculated excited-state transitions at higher energy should thus correspond to the experimentally observed absorption peaks at shorter wavelengths, which should be associated with overlapping π - π* transitions.[81] The transition with n = 4 should be ascribed to the HOMO–LUMO+2 π - π* transition, which exhibits localized-excitation (LE) character according to the molecular-orbital distribution shown in Figure 5.7. The LUMO+2 is mainly located on the triphenylamine, thiophene, and benzothiadiazole moieties.

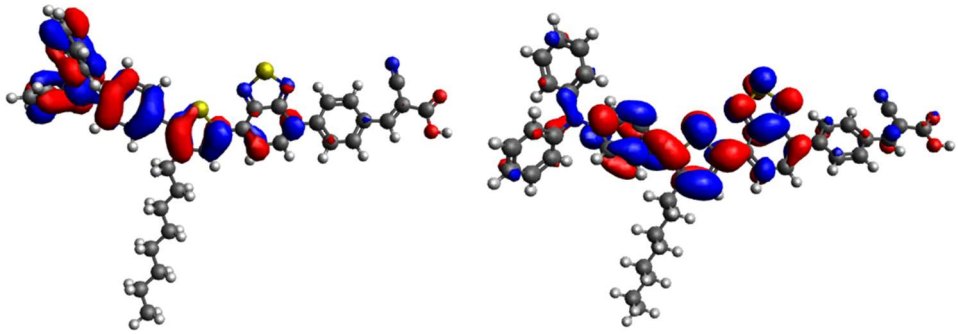

HOMO **LUMO+2**

Figure 5.7 HOMO and LUMO+2 for **RK-1** in acetonitrile calculated at the B3LYP/6-31g(d) level of theory.

5.5.2 Optimized structures for the excited state (ES) of RK-1

To better understand the origin of the Stokes shift, the excited-state (ES) structure of **RK-1** in acetonitrile was also optimized. The metric parameters for the ground state (GS) and ES structures are listed in Table 5.5, and a juxtaposition of the corresponding optimized structures is shown in Figure 5.8.

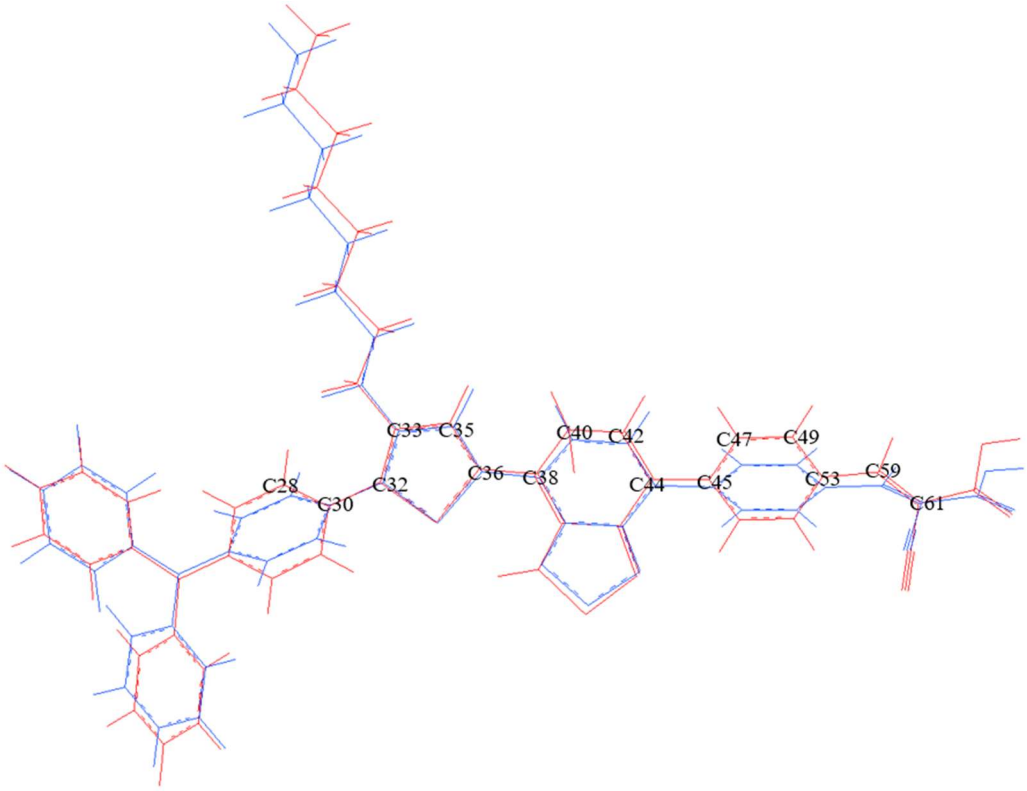

Figure 5.8. Juxtaposition of the optimized structures for **RK-1** in the ground (blue) and excited state (red) in acetonitrile; only selected atoms are labeled for clarity.

Table 5.5 Structural parameters for the GS and ES structures of **RK-1**.

	Angle			
	1	**2**	**3**	**4**
GS	45.47°	-12.18 °	-33.26 °	179.97 °
ES	26.81 °	-0.42 °	-20.45 °	179.76 °
ES-GS	-18.66 °	11.76 °	12.81 °	-0.21 °

Angles **1**-**4** are defined as the dihedral angles C28-C30-C32-C33 (between the triphenylamine benzene ring and the adjacent thiophene ring), C35-C36-C38-C40

(between the thiophene ring and the adjacent benzothiadiazole ring), C42-C44-C45-C47 (between the benzothiadiazole and the adjacent benzene ring), and C49-C53-C59-C61, respectively.

As shown in Table 5.5, the angles **1**-**3**, between different adjacent aromatic rings change significantly upon excitation (ES-GS = -18.66° to 12.81°), which may be one possible explanation for the experimentally observed Stokes shift. Moreover, these three modes of twisting and the associated three dihedral angles may account for the observed thepeak and two shoulders in the emission band of **RK-1** at 550-750 nm. In addition, the benzene ring and the adjacent cyanoacrylic acid group (angle **4**) preserve a co-planar arrangement during excitation, i.e., the π-conjugation of the anchoring group should be able to promote an efficient electron injection when adsorbed onto the TiO_2 film.

5.6 Binding mode of RK-1 on TiO_2 films

The hypsochromic shift of the absorption peaks of **RK-1** upon adsorption onto TiO_2 (Figure 5.9) indicates that the anchoring group binds in its deprotonated form at the dye···TiO_2 interface,[106] and generally, bidentate bridging (BB) anchoring modes are considered more stable than other anchoring modes for similar interfaces.[74] Furthermore, the cyanoacrylic acid group could also bind via the COO/CN binding mode to the surface of the TiO_2 substrate, given that coordination of **RK-1** to the Lewis-acidic Ti centers is possible via the O and N atoms. In order to investigate the adsorption of **RK-1** in detail, the **RK-1**···TiO_2 interface was optimized using the two most favorable deprotonated modes, i.e., A2 (COO/CN) and BB, on a $(TiO_2)_9$ cluster.

Adsorption energies were calculated according to equation 3.1 in Chapter 3.The results of these calculations, which are summarized in Table 5.6, show that the A2 and the BB mode are comparable in energy ($\Delta E = 0.013$ eV), which indicates that the binding mode cannot be simply determined on the grounds of energetic differences. These results also suggest that the two binding modes most likely co-exist and that the coordination mode is probably strongly influenced by the immediate environment of the dye···TiO_2 interface.[107] Thus, more experimental work, such as X-ray (XRR) or neutron reflectometry (NR) should be carried out in order to determine the binding mode of **RK-1** on TiO_2 with more accuracy.

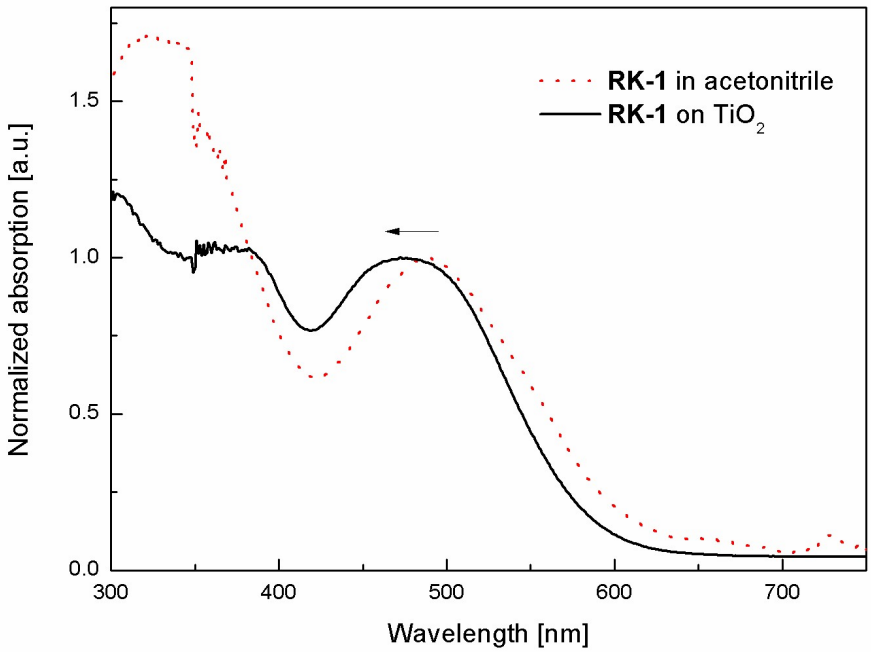

Figure 5.9 Absorption spectra of **RK1** adsorbed on thin films of TiO_2 (thickness: ~ 4 μm) and in acetonitrile ([**RK-1**] = 7.5×10^{-6} mol^{-1} L).

Table 5.6. Adsorption-mode-dependent geometries of **RK-1** on $(TiO_2)_9$ optimized at the B3LYP/6-31g(d) level of theory, and the corresponding adsorption energies.

Adsorption mode	Starting structure	Final structure	Adsorption Energy [eV]	ΔE[a] [eV]
A2	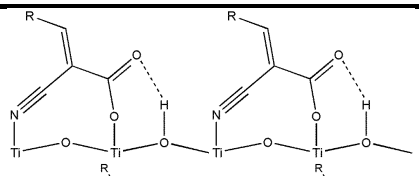		-1.198	0
BB	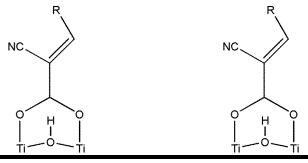		-1.186	0.013

5.7 Electrochemical impedance spectroscopy (EIS) measurements on RK-1

In the Nyquist plots of **RK-1** and **N719** (Figure 5.9), the larger semicircle is attributed to the impedance of the recombination at the TiO_2/dye/electrolyte interface (R_{CT}). The calculated R_{CT} value of **RK-1** (144.5 Ω/cm^2) is slightly larger than that of **N719** (138.0 Ω/ cm^2), which indicates that the recombination of the sensitized TiO_2 electrode is slightly more effienciently to be suppressed by **RK-1** than **N719**, and that this is in agreement with the photovoltaic results for the **RK-1** device, which shows comparable open-circuit voltage values to the **N719** device.[34] And generally, **RK-1** shows a competitive ability to suppress recombination in photovoltaic devices.

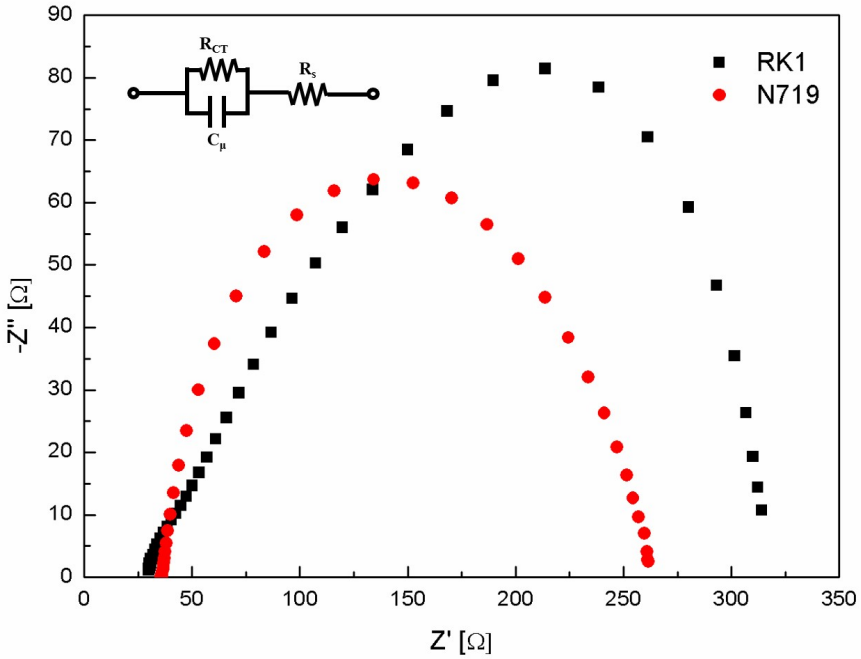

Figure 5.9 EIS spectra of TiO_2 electrodes sensitized with **RK-1** and **N719** (100 kHz - 10 mHz) under the dark condition. The circuit illustrated here is identical to that of the tested sample. The active area of the sealed cell is 1.0 cm^2.

Table 5.7. Simulated data, R_{CT}, C_μ and R_S values of **RK-1** from EIS measurements.

Dye	R_{CT} [Ω/cm^2]	C_μ [μF/cm^2]	R_S [Ω]
RK-1	144.5	0.000722	88.8
N719	138.0	0.000715	95.7

5.8 Conclusions

In this chapter, the previously reported organic dye **RK-1** was investigated experimentally (UV/vis, fluorescence, and electrochemical impedance spectroscopy) and computationally (DFT and TDDFT calculations *in vacuo*, acetonitrile, and on a $(TiO_2)_9$ cluster).

The UV/vis spectrum of **RK-1** in acetonitrile revealed broad absorption bands in the visible region (λ_{max} = 490 nm). The concentration-dependent UV/vis spectra of **RK-1** in acetonitrile showed a hypsochromic shift upon increasing the concentration, which is consistent with H-aggregation. The UV/vis spectrum of **RK-1** adsorbed onto TiO_2 also exhibited a hypsochromic shift of the absorption band compared to the spectra of the dye in acetonitrile. This hypsochromic shift should be attributed to the deprotonation of the cyanoacrylic acid group during adsorption. The emission spectrum of **RK-1** showed an emission band with one peak and two shoulders, indicating the presence of several different structural reorganization processes during excitation. The EIS spectrum of **RK-1** revealed a competitive ability to suppress electron recombination (R_{CT} = 144.5 Ω cm^{-2}) compared to that of a device based on **N719** (138.0 Ω cm^{-2}).

The results of the DFT/TDDFT calculations are in a good agreement with the UV/vis results, and were thus used to analyze the composition and contributions to the excitations in terms of molecular orbital transitions. The result of this analysis revealed that the ICT should be predominantly attributed to the HOMO-LUMO transition. Moreover, the geometry of **RK-1** in the excited state was calculated, and the result showed that the three dihedral angles between the adjacent aromatic rings in the donor and the π-bridge change significantly during the excitation, and that this may be consistent with the observed three peaks in the experimental emission spectrum. To investigate the behavior of **RK-1** on the TiO_2 surface, A2 and BB binding modes were calculated, and the results showed a relatively small difference in energy (0.013 eV), which suggests that the adsorption mode cannot be determined

solely on the basis of energetic differences, and that further experimental studies are required to unequivocally answer this question.

Chapter 6

The Ruthenium-based Dyes N3 and N749

6.1 Introduction

Ruthenium-based dyes are the most commonly used high-efficiency sensitizers in dye-sensitized solar cells (DSSCs), especially **N719** (*di-tetrabutylammonium cis-bis(isothiocyanato)bis(2,2'-bipyridyl-4,4'-dicarboxylato)ruthenium(II)*),[13b, 113] **N3** (*cis-bis(isothiocyanato)bis(2,2'-bipyridyl-4,4'-dicarboxylato)ruthenium(II)*), [13b, 13d, 113b] and **N749** (*4,4',4''-tricarboxy-2,2':6',2'-terpyridine*), the latter of which is also commonly known as Black Dye (BD).[13c, 114] **N719** is usually regarded as the industry standard for DSSC performance[9a, 14] and the bench mark for conversion efficiency (10%).[13b] As the prototype for most Ru-based dyes, **N3** also shows a competitive power-conversion efficiency (η; PCE) of 11.2%.[13d] **N749** is remarkable for its wide absorbance range, which covers the visible region and extends into the near-infrared (NIR) area,[114] reaching an efficiency of 10.4%.[13c]

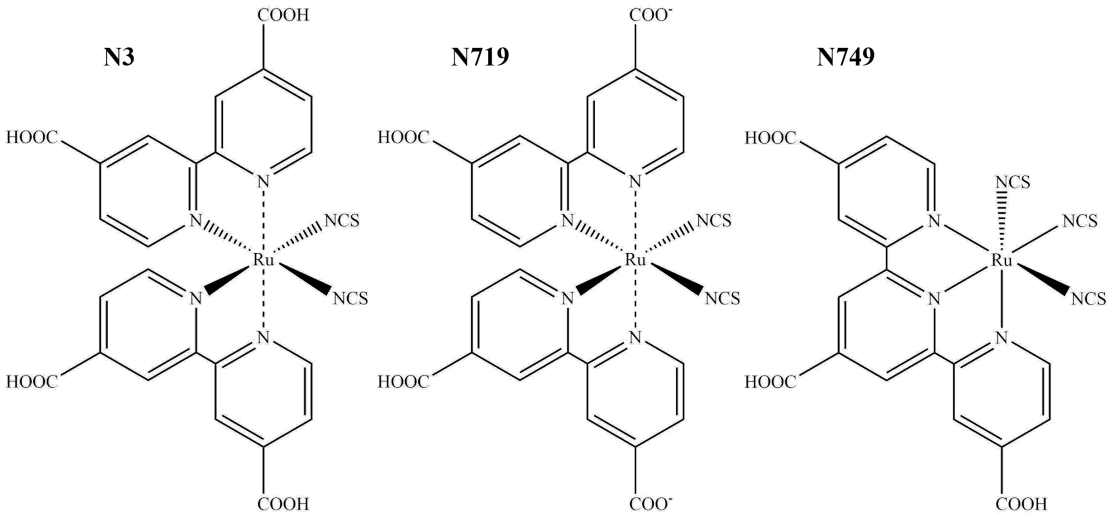

Figure 6.1 Chemical structures of **N3**, **N719**, and **N749** (Black Dye); cations are omitted for clarity.

Ru-based dyes have been widely and systematically investigated with respect to their optical, electrochemical, and photovoltaic properties.[113b, 114-115] However, ambiguity of the configuration and orientations of these dye molecules at the dye···TiO_2 interface remains.[116] To get a better insight into these topics, X-ray diffraction (XRD) was used to investigate the refined structure of **N749**,[117] and X-ray reflectometry (XRR), which has been validated as an effective method to study the dye···TiO_2 interface,[118] was used to examine the behavior of **N3** and **N719** on TiO_2 films under varying conditions. In this chapter, the existence of multiple conformations of **N749** anions discovered by XRD experiments was further investigated theoretically by density functional theory (DFT) methods. Moreover, acid dissociation constants of the carboxyl groups in **N749** and **N3** were examined experimentally and theoretically, as the deprotonation behavior of the anchor group is crucial for the anchoring of the dye molecules on the TiO_2 surface. All X-ray

diffraction and X-ray reflectometry experimental results about **N3** and **N749** in this chapter were measured by Dr. Jacqueline M Cole and her colleagues.

6.2 Computational details

In Section 6.3, conformation **1** (shown in Figure 6.2, **1**) was used as a starting point for geometry optimizations at the B3LYP[59]/6-31g(d)[71] (H, C, N, O, S) and B3LYP/LANL2DZ[119] (Ru) level of theory; the optimized structure is denoted as **6**. Frequency calculations were carried out at the same level of theory to prove the absence of any imaginary frequencies. Subsequently, single-point energies were calculated for **1**-**6** at the same level of theory as for the geometry optimizations.

The implicit method employed in Sections 6.5 and 6.6 was used to carry outgeometry optimizations of all deprotonated species for **N3** and **N749** in the gas phase at the B3LYP level[59]/6-31g(d)[71] (H, C, N, O, S) or B3LYP[59]/LANL2DZ[119] (Ru) level of theory. Subsequently, frequency and single-point energy calculations were carried out at the same level of theory to obtain the Gibbs free energy values based on the optimized geometries. In solution, all species were initially optimized, and then used to calculate single-point energies at the same level of theory using the solvation model based on density (SMD)[120] and CPCM-UFF models,[72b, 121] respectively. For the calculations of the solvation-free energies in the CPCM-UFF model, single-point energy calculations in the gas phase were performed on the optimized structures in solution, using the same level of theory.

To calculate the pK_a values with the explicit model, all deprotonated species with

four explicit water molecules were initially optimized geometrically in the gas phase and in solution, before frequency and single-point energy calculations were carried out. Then, single-point energy calculations were performed on the optimized structures in solution, using the same level of theory to obtain the solvation-free energy. With the explicit-assist method (details were shown in section 6.6.2), four explicit water molecules were removed after the geometry optimizations in solution, followed by a single-point energy calculation with and without the solvent effect using the CPCM-UFF model.

6.3 Refined configuration of the N749 anions

6.3.1 Conformations with varying orientations of the NCS groups

N749 molecules contain three carboxylic acid groups that can potentially be used as anchors for the adsorption onto the TiO_2 surface. Carboxylic acid groups can bind to the TiO_2 surface, although carboxylates are generally regarded as better anchor groups.[122] This is mostly due to the monodentate binding mode[74] of the carboxylic acid group, which is less efficient than the bidentate bridging mode of the carboxylate anion. Generally, **N749** is modeled under the assumption that it contains one carboxylate and two carboxylic acid groups.[117] However, this assumption was not supported by previously reported crystal structures.[13c, 123] In addition, the refined structure of the three NCS groups in **N749** also needs to be determined in detail, as these NCS groups play an important role in the context of electron recombination by blocking the electrolyte from accessing the surface of TiO_2 and the transparent conductive oxide (TCO).

Therefore, two single crystals of **N749** were generated by evaporating the solvent from solutions of **N749** in either methanol or methanol:acetonitrile (1:1, v/v), which allowed observing five conformations of the corresponding anion by single-crystal X-ray diffraction analysis.[117] For comparison, the structure of the anion was optimized by DFT calculations at the B3LYP/6-31g(d) (H, C, N, O, S) and B3LYP/LANL2DZ (Ru) levels of theory.

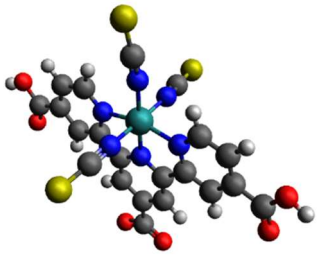	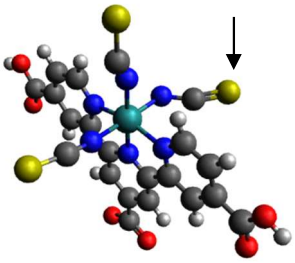	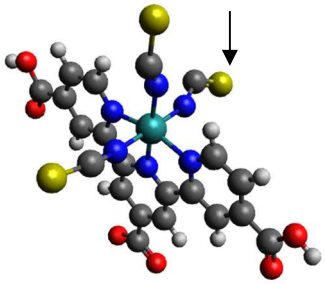
1 Symmetric anion	**2** Asymmetric anion 1 (major disorder component)	**3** Asymmetric anion 1 (minor disorder component)
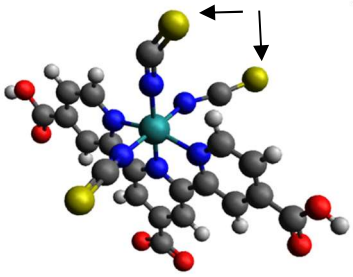	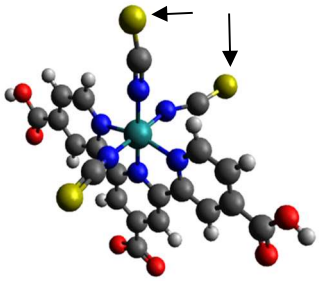	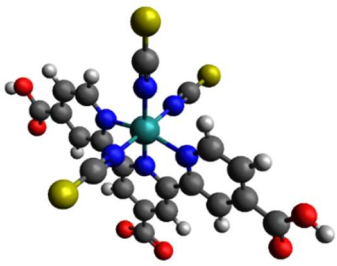
4 Asymmetric anion 2 (major disorder component)	**5** Asymmetric anion 2 (major disorder component)	**6** Theoretically optimized anion (DFT)

Figure 6.2 Experimentally observed symmetric (**1**) and asymmetric (**2**-**5**) conformations for the monoanion of **N749**, together with the DFT-optimized structure of monoanion of **N749** (**6**). The asymmetric anions 1 (**2**, **3**) are shown with relative occupancies: major (86%) and minor (14%). The axial and equatorial NCS disorder in

anion 2 (**4**, **5**) are shown with relative occupancies: major (77% axial; 60% equatorial) and minor (23% axial; 40% equatorial). Arrows highlight disordered groups.

6.3.2 Conformational energies

To further investigate the conformations of the **N749** anions (**1**-**5**) in terms of energy, DFT calculations were carried out at the B3LYP[24, 25]/6-31g(d)[26] (H, C, N, O, S) and B3LYP[24, 25]/LANL2DZ[27] (Ru) levels of theory. For the geometry optimizations, the structure of **1** was chosen as a starting point, which delivered **6** as the optimized structure. For the single-point energy calculations, all conformations (**1**-**6**) were calculated at the same level as the geometry optimization mentioned above.

Table 6.1 Conformational energies calculated by DFT methods.

Conformation	Energy [Hartree]	ΔE [eV][a]
1	-2874.906	0.21
2	-2874.597	8.63
3	-2874.306	16.54
4	-2874.742	4.68
5	-2874.754	4.37
6	-2874.914	-

a: ΔE refers to the energy difference between **1**-**5** and **6**.

Conformation **1** shows the lowest energy value among **1**-**6**, indicating that **1** should energetically be the most stable conformation. Moreover, a very small energy

difference (~0.2 eV) was observed between **1** and **6**, which exhibits an almost symmetric structure. Intuitively, this can be rationalized in terms of high levels of similarity between **1** and **6**, due to the presence of three ordered NCS groups in both conformations. Furthermore, **1** most closely resembles the conventional model for the **N749** anion with one carboxylate and two carboxylic acid groups. In consequence, due to its low energy and symmetric structure, **1** should be ideally suited as a starting point for modelling **N749** in the gas phase or upon adsorption onto TiO_2 films.

In contrast, **2-5** form asymmetric anions, and their relatively large energy differences (~4.4 to 16.5 eV) relative to **6** should primarily be associated with the substantially distorted NCS ligands. Nevertheless, the energy differences seem relatively large, especially compared to solution-based computational results that show that the energy penalty for distortion of one NCS ligands in **N749** is only 0.17 eV.[124] These large energy differences may thus arise from crystal-field forces that have a significant impact on molecular structures so that the solid-state-energy differences are higher than the solution-state-energy barriers. Moreover, in the solution-based calculations, the distortion of the NCS ligands affect mainly the Ru-N-C angle, while in **2-5**, the distortions of the NCS ligands primarily occur at the N-C-S angle, which may cause much larger energy differences. To examine this hypothesis, the energies of the NCS anions (NCS1-3), under the same geometric constraints as in **2-5**, were calculated at the B3LYP/6-31g(d) level of theory.

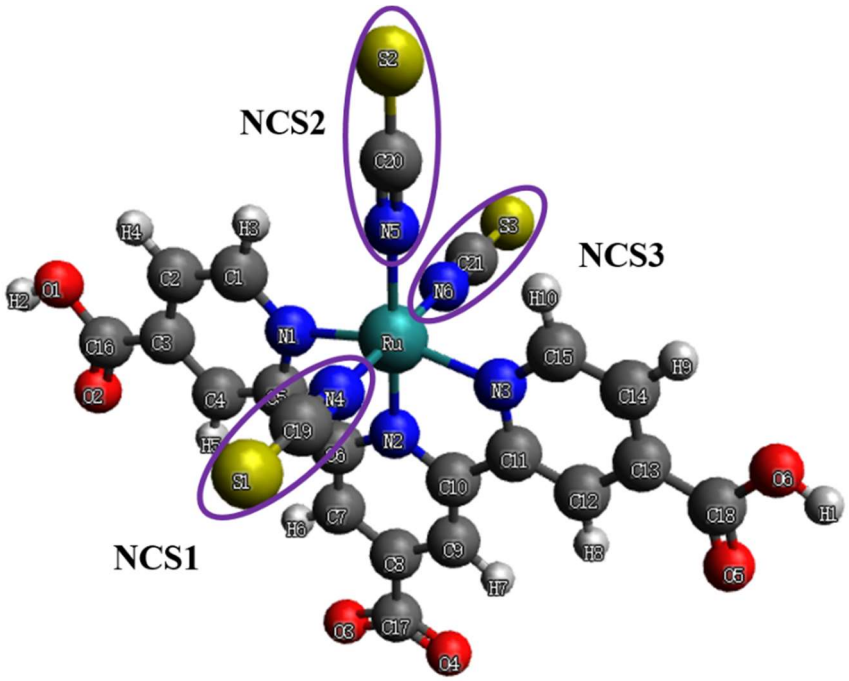

Figure 6.3 Calculated structure of **6**, wherein S1-C19-N4 is denoted as NCS1, S2-N20-N5 as NCS2, and S3-C21-N6 as NCS3.

Table 6.2 Geometric parameters and energies for the NCS anions in **1**-**6**.

	NCS1				NCS2				NCS3					
	Angle N-C-S [º]	Bond N-C [Å]	Bond C-S [Å]	ΔE [eV]	Angle N-C-S [º]	Bond N-C [Å]	Bond C-S [Å]	ΔE [eV]	Angle N-C-S [º]	Bond N-C [Å]	Bond S-C [Å]	ΔE [eV]	ΔE_{NCS} [eV]	ΔE_{tot} [eV]
1	178.87	1.14	1.67	0.06	177.37	1.16	1.66	0.02	178.85	1.16	1.64	0.03	0.11	0.21
2	157.30	0.93	1.95	6.77	174.83	1.23	1.73	0.18	157.58	1.36	1.54	1.70	8.64	8.63
3	174.83	1.23	1.73	0.17	157.30	0.93	1.95	6.77	122.42	1.26	1.53	10.80	17.74	16.54
4	171.62	1.08	1.56	1.06	143.08	1.27	1.58	1.25	172.18	1.48	1.62	2.66	4.97	4.68
5	171.62	1.08	1.56	1.06	169.25	1.27	1.61	0.46	155.10	1.48	1.77	3.05	4.56	4.37
6	179.79	1.18	1.64	-	180.00	1.18	1.65	-	179.90	1.18	1.64	-		-

The results show that most distortions of the NCS groups at the N-C-S angle lead to an energy penalty of ~ 1 eV. For NCS1 in **2**, the main energy difference should be attributed to the N-C-S angle (157.60°), as the other N-C-S angles are very close to 180°. For NCS2 in **3**, the energy cost for distortion of the NCS ligand is much higher than for the other conformers, probably due to the unexpectedly short N≡C bond (0.93Å). Furthermore, the estimated total energy differences of the three distorted NCS ligands are in good agreement with the results listed in Table 6.1, which supports the notion that the main energy difference of the disordered conformations results from changes to the optimal N-C-S angle and the N≡C bond length.

6.4 Calculating pK_a values: theoretical background

6.4.1 The thermodynamics of acid dissociation equilibria

Acid dissociation constants, i.e., the so-called pK_a values, are a quantitative solvent-specific index to measure the dissociation of a Brønsted acid (HA) and to describe the protonation and deprotonation state. The dissociation (in the following with water as a representative solvent) of an acid, HA, can be expressed by:

$$HA(aq) \rightleftharpoons H^+(aq) + A^-(aq) \qquad \text{(eq 6.1)}$$

The pK_a value is defined as the negative decadic logarithm of the equilibrium constant, K_a:

$$pK_a = -logK_a \qquad \text{(eq 6.2)}$$

$$K_a = \frac{[A^-_{aq}][H^+_{aq}]}{[HA_{aq}]} \qquad \text{(eq 6.3)}$$

And given that

$$\Delta G^* = -2.303RTlogK_a \qquad \text{(eq 6.4)}$$

$$pK_a = \frac{\Delta G^*}{2.303RT} \qquad \text{(eq 6.5)}$$

where R represents the ideal gas constant, T the temperature, ΔG^* the Gibbs free energy of the reaction under standard conditions in solution, where an error of 1.36 kcal/mol affords an error of ±1 for the pK_a value.

To accurately calculate the pK_a value of an acid in a certain solvent, two thermodynamic cycles have commonly been used in a direct method or a proton-exchange method.[125] In this thesis, the direct cycle (Figure 6.4) was adopted to calculate the pK_a values for both the implicit solvent model[126] and the implicit-explicit model.[125, 127]

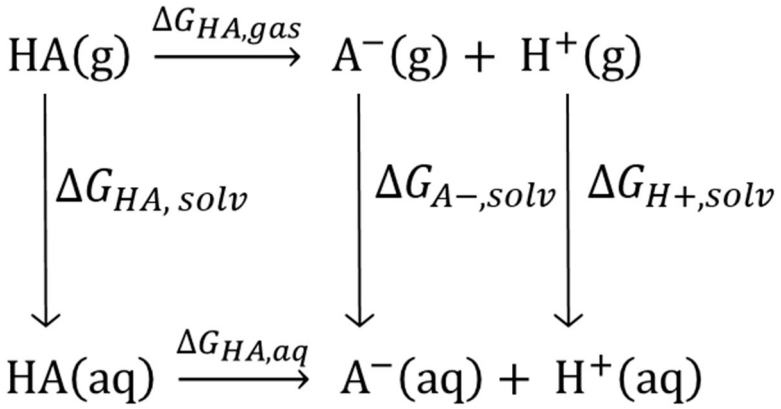

Figure 6.4. Direct thermodynamic cycle for the dissociation of an acid, HA. $\Delta G_{X,\,solv}$ represents the free energy of solvation of a specific solute X.

Based on the cycle shown in Figure 6.4, $\Delta G_{HA,\,aq}$ can be calculated according to:

$$\Delta G_{HA,gas} = G_{H^+,gas} + G_{A^-,gas} - G_{HA,gas} \quad \text{(eq 6.6)}$$

$$\Delta G_{HA,aq} = \Delta G_{HA,gas,} + \Delta G_{A^-,solv} + \Delta G_{H^+,solv} - G_{HA,sol} \quad \text{(eq 6.7)}$$

Combining equation 6.6 and 6.7 leads to:

$$\Delta G_{HA,aq} = G_{H^+,gas} + G_{A^-,gas} - G_{HA,gas} + \Delta G_{H^+,solv} + \Delta G_{A^-,solv} - G_{HA,solv} \quad \text{(eq 6.8)}$$

The theoretical values for the Gibbs free energy of the proton in the gas phase ($G_{H+,gas}$ = -6.28 kcal/mol)[128] and in solution ($\Delta G_{H+,solv}$ = -265.9 kcal/mol)[125] were obtained from previous reports. All other free energy values in the gas phase ($G_{A-\ gas}$ and $G_{HA\ gas}$) were obtained from DFT frequency calculations on the corresponding optimized geometries in the gas phase. In these calculations, a value of 1.894 kcal/mol was used as a corrective term for the conversion of ΔG_{gas} (1 atm) to ΔG^*_{gas} (1 M).

Subsequently, after determining the free energies of solvation of A^- and HA, the pK_a values can be calculated according to:

$$pK_a = \frac{G_{A^-,gas} - G_{HA,gas} + \Delta G_{A^-,solv} - G_{HA,solv} - 270.29}{1.3644} \quad \text{(eq 6.9)}$$

6.4.2 Calculating the free energy of solvation

The free energy of solvation is defined as the difference between the free energy of a species in the gas phase and in solution:

$$\Delta G_{solv} = G_{soln} - G_{gas} \quad \text{(eq 6.10)}$$

However, according to a comment on the use of continuum solvent models,[129] such

as the polarization continuum model (PCM),[72] the free energy of solvation should be defined as:

$$\Delta G_{solv} = (E_{soln} + G_{nes}) - E_{gas} \qquad \text{(eq 6.11)}$$

where E_{soln} and E_{gas} refer to the electronic energies of the solvent with and without the solvent effect, while G_{nes} refers to the sum of all non-electrostatic contributions to the solvation free energy. Quantum-chemistry software packages such as Gaussian09 suggest calculating the solvation free energy according to eq 6.11.[129] So far, two methods have been reported.[125-126, 127] The first uses the SMD model,[120] whereby ΔG is explicitly shown in the calculating results. The second uses the difference in electronic energy for the optimized geometry in the presence or absence of the solvent field.[126a] Both methods were used to calculate the pK_a values of **N3**, and the latter was chosen for all calculations in this chapter, as the results of the SMD model deviate too much from the experimental results. For the sake of completeness, the results of the SMD calculations are shown in Appendix B. All calculations were based on water as a solvent.

6.5 Calculating pK_a values with the implicit method.

6.5.1 Calculating the pK_a value of N749 in water

N749 contains three carboxylic acid groups that can be deprotonated in a stepwise fashion:

$$BDH3 \rightleftharpoons BDH2^- + H^+ \quad pK_a1$$

$$BDH2^- \rightleftharpoons BDH1^{2-} + H^+ \quad pK_a2$$

$$BDH1^{2-} \rightleftharpoons BDH0^{3-} + H^+ \quad pK_a3$$

Scheme 6.1. Stepwise deprotonation of **N749** and the corresponding acid-base equilibria.

To further determine the deprotonation path of **N749**, all deprotonated forms were denoted as BDHx, which is consistent with a previous study,[126b] (x = 0-3, whereby x refers to the number of protons left in the Black Dye). **BDH2** (**BDH2_A** and **BDH2_B**) and **BDH1** (**BDH1_A** and **BDH1_B**) consist of two isomers each. All structures are shown in Figure 6.5. To compare the stability of the isomers, the Gibbs free energies in solution were calculated using equations 6.10 and 6.11.[129]

$$G_{soln} = (E_{soln} + G_{nes}) + \Delta G_{corr} \qquad \text{(eq 6.12)}$$

wherein ΔG_{corr} refers to the thermal contribution to the Gibbs free energy in the gas phase. Thus, in terms of the Gibbs free energy in solution, the species **BDH_2^-_A** and BDH^-_A are the most stable structures (Table 6.3).

Table 6.3. Relative Gibbs free energies of **BDH2_A** and **BDH2_B**; **BDH1_A** and **BDH1_B**.

	A (kcal/mol)	**B** (kcal/mol)
$BDH2^-$	**0.00**	0.27
$BDH1^-$	**0.00**	0.76

Subsequently, the implicit method with the CPCM-Universal Force Field (UFF) was used to calculate the pK_a values of all deprotonated forms of **N749** as outlined in Scheme 6.1.

The fully protonated species contains two potential deprotonation sites, i.e., a carboxylic acid group attached to the central pyridyl moiety, and two carboxylic acid groups attached to the adjacent pyridyl moieties; for the first deprotonation, pK_a values of 3.12 (pK_a1 for **BDH3**/**BDH2_A**) and 3.32 (pK_a1 for **BDH3**/**BDH2_B**) were calculated, which suggests that the proton on the lateral carboxyl acid groups are more acidic that that on the central pyridyl moiety, and that the initial deprotonation should occur there. The relatively higher pK_a value of the proton of the carboxyl acid group attached to the central pyridyl moiety is *trans* to a more electron-donating NCS ligand, which increases the acidity of this carboxylic acid group via π-back-bonding.[130] Accordingly, the diprotonated species (**BDH2**) should also show two possible deprotonation sites on the lateral and the central pyridyl moiety. At this stage, both carboxylate anion and anionic NCS ligand should donate electron density to the lateral and central carboxylic acid groups at the *trans* positions, respectively. Based on

calculations of the Gibbs free energy in solution, **BDH1_A** should be the most stable isomer so that the central carboxyl acid group is involved in deprotonation. Subsequently, the last proton on the lateral carboxylic acid group should dissociate.

Table 6.4 Calculated pK_a values for all deprotonated forms in Scheme 5.1 using the UFF model.

Acid/base couple	UFF
BDH3/BDH2_A	3.12
BDH3/BDH2_B	3.32
BDH2_A/BDH1_A	4.00
BDH2_A/BDH1_B	4.56
BDH2_B/BDH1_A	3.80
BDH2_B/BDH1_B	4.36
BDH1_A/BDH0	5.65
BDH1_B/BDH0	5.09

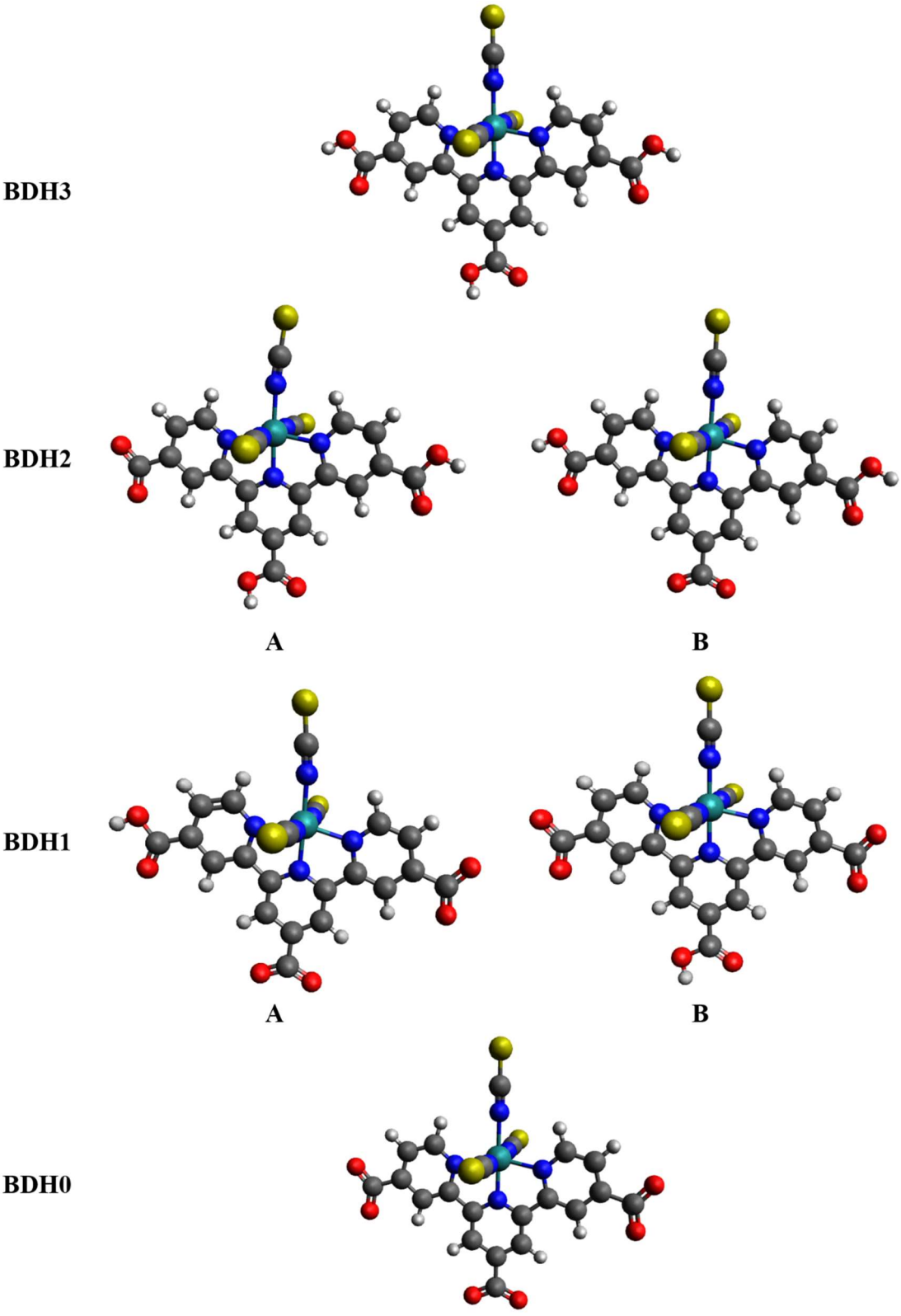

Figure 6.5. Optimized molecular structures of BDHx complexes (x = 0-3).

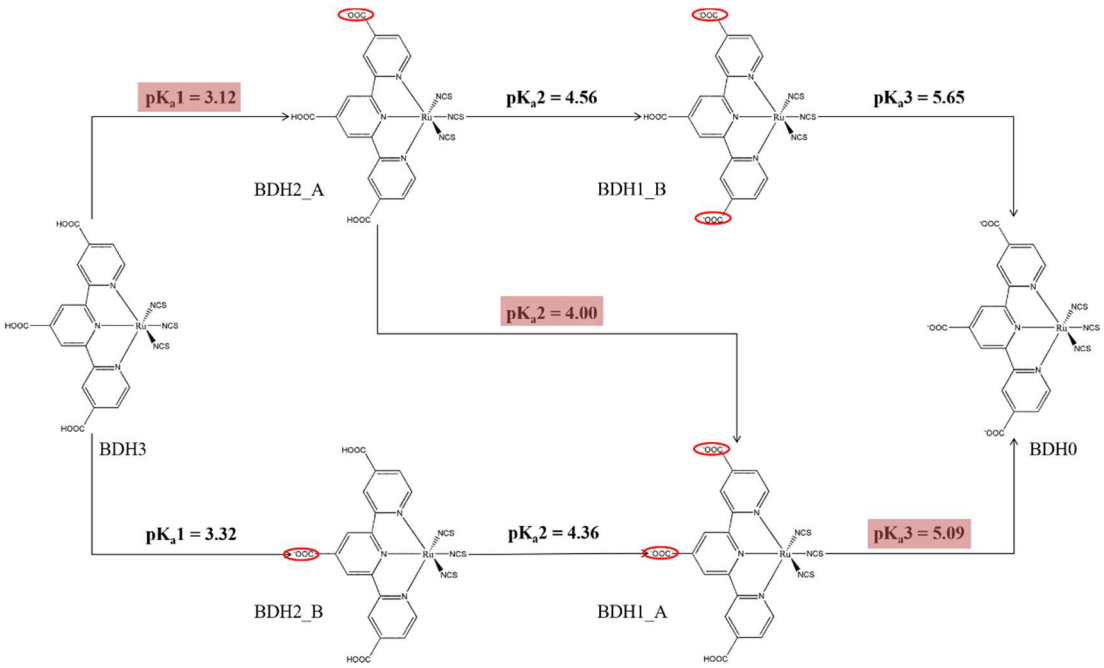

Figure 6.6. Schematic representation of the deprotonation pathways of **BDH3** with the corresponding DFT-derived pK_a values. The pathways with the lowest pK_a values are highlighted.

This calculated deprotonation pathway is not consistent with the path suggested on the basis of previously reported experimental results,[130] which include only two protonation equilibria. One is a simultaneous two-proton dissociation involving the peripheral pyridyl moieties, while the other describes the subsequent deprotonation of the central pyridyl moiety:

$$BDH3 \rightleftharpoons BDH1^{2-} + 2H^{+} \qquad pK_{a1\&2} = 3.3 \qquad \text{(eq. 5.13)}$$

$$BDH1^{2-} \rightleftharpoons BDH^{3-} + H^{+} \qquad pK_{a3} = 5.0 \qquad \text{(eq. 5.14)}$$

Scheme 6.2. Acid-base equilibria for the stepwise deprotonation of **N749** reported in reference 127.

However, in this previous study on another ruthenium-based dye, **N3**,[130] only two inflection points were found in the solution UV/vis spectrum (pH = 2-11); the first inflection point was assigned to the simultaneous dissociation of two protons, a notion that was also proposed by the results of a different study.[131] However, this hypothesis was disproved by a recent study using more advanced experimental and theoretical methods, which discovered four inflection points in the UV/vis spectrum and accordingly four pK_a values, which were feasibly embedded in a theoretically calculated model.[126a] Due to the limitations of the research methods at an early stage, and due to the similarity of **N3** and **N749**, it could be speculated that there may be a third inflection point in the UV/vis spectrum of **N749** that has not yet been discovered.

Furthermore, the experimental results for the second deprotonation of **N749** suggest that the deprotonation occurs at the lateral pyridyl moiety (**BDH2_A** → **BDH1_B**), while the calculations suggest a deprotonation of the COOH group of the central pyridyl moiety (**BDH2_A** → **BDH1_A**). Intuitively, **BDH1_B**, wherein only one carboxylic acid is connected to the central pyridyl moiety, should be more stable than **BDH1_A** on account of its symmetrical geometry, which is supported by theoretical calculations that suggest a lower energy for **BDH1_B** relative to **BDH1_A** in the gas phase and in aqueous solution. However, when the solvation free energy is considered, the formation of **BDH1_A** is favored (*vide supra*), which may be caused by the solvent effect of the polar solvent molecules.

Although the calculated pK_a1 (3.12) and pK_a2 (4.00) values differ from the

experimental results (pKa1&2 = 3.3 ± 1) less than one pK_a unit and the calculated pK_a3 value (5.09) is very closed to the experimental value (pKa3 = 5.0 ± 1), the calculation method is still very limited due to the discrepancy of deprotonation pathway between theoretical and experimental results.

6.5.2 Calculating the pK_a value of N3 in water

In **N3**, there are four carboxylic acid groups at which the deprotonation may occur, and therefore, four stepwise deprotonation equilibria may be formulated:

$$N3H4 \rightleftharpoons N3H3^- + H^+ \quad pK_a1$$

$$N3H3^- \rightleftharpoons N3H2^{2-} + H^+ \quad pK_a2$$

$$N3H2^{2-} \rightleftharpoons N3H1^{3-} + H^+ \quad pK_a3$$

$$N3H1^{3-} \rightleftharpoons N3H0^{4-} + H^+ \quad pK_a4$$

Scheme 5.3. Stepwise acid-base equilibria for **N3**.

The deprotonated forms of **N3** are denoted as **N3Hx** (x = 0-4; wherein x refers to the number of protons left in **N3**). **N3H3** consists of the two isomers **N3H3_A** and **N3H3_B**; **N3H2** consists of the four isomers **N3H2_A**, **N3H2_B**, **N3H2_C**, and **N3H2_D**; **N3nH1** consists of the two isomers **N3H1_A** and **N3H1_B**. Selected structures of these **N3** complexes in the deprotonation pathway are shown in Figure 6.7.

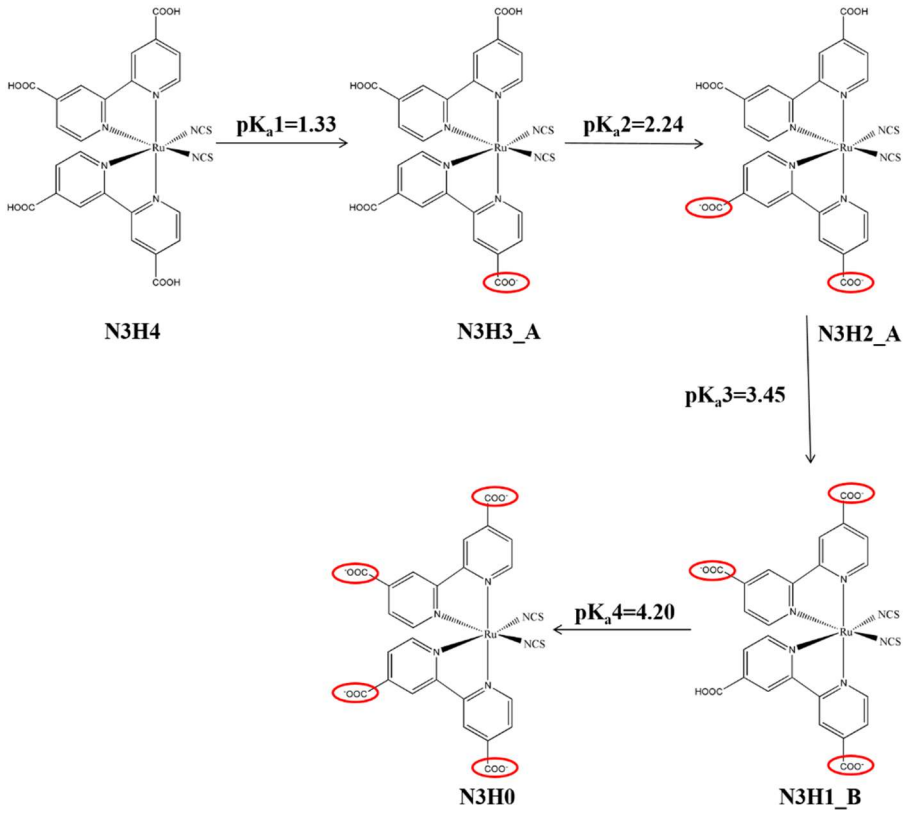

Figure 6.7. Schematic representation of the deprotonation pathway for **N3**, together with experimentally measured pK_a values.[126a]

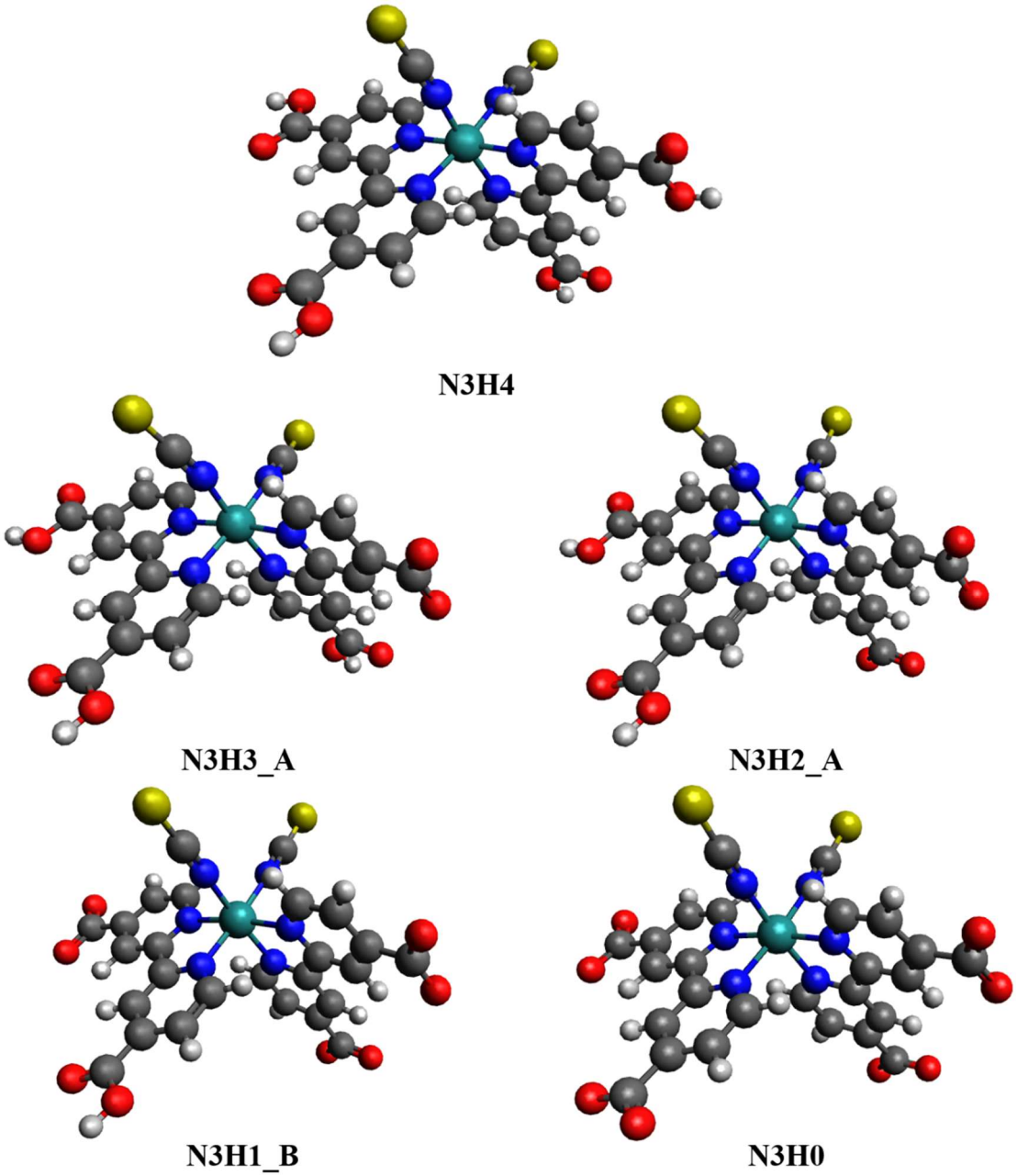

Figure 6.8 Optimized molecular structures for **N3Hx** (x = 0-4) complexes in the deprotonation pathway (*cf.* Figure 6.7).

The deprotonation pathway of **N3** has recently been determined in the context of a combined experimental and theoretical study.[126a]

In the context of this chapter, the implicit method with CPCM-UFF was used to calculate the pK_a values (Table 6.5) of the deprotonated forms of **N3** according to the pathway shown in Figure 6.7.

Table 6.5 Calculated pK_a values for the deprotonated forms shown in Figure 6.7 using the UFF model, together with the error between the calculated and experimental results.

	Exp.	**UFF**	**Err.**
pK_a1	1.33	2.06	0.73
pK_a2	2.24	3.16	0.92
pK_a3	3.45	4.43	0.98
pK_a4	4.20	5.68	1.48

Based on the deprotonation pathway (Figure 6.7), **N3H4** should lose its first proton (**N3H4** → **N3H3_A**) at the pyridyl moieties *cis* to the NCS ligands, which experience less electron donation from the anionic NCS ligands than the protons at the *trans* positions.[126a] The second deprotonation (**N3H3_A** → **N3H2_A**) should occur at the already deprotonated di-pyridine ligand. This could be explained in a similar fashion as for **N749**, i.e., the carboxylate formed during the first deprotonation may offer electron density to the pyridyl group at its *trans* positions, which would decrease the

acidity of the attached COOH group, leading to a higher pK_a value. The third deprotonation occurs, as the first, on the pyridyl ligand *cis* to the NCS ligand, before the last proton dissociates.

The theoretically calculated pK_a1, pK_a2, and pK_a3 values exhibit errors of less than 1 pK_a unit compared to the experimental results. However, pK_a4 is associated with a relatively large error of 1.48 pK_a units. The deviation relative to the experimental results seems to increase with increasing negative charge of the deprotonated species. This may be due to the use of the implicit model, which might underestimate the interactions between highly charged species and the water molecules. Thus, an explicit method may be required to more accurately describe the interactions between the solvent molecules and highly charged ions.

6.5.3 Calculating the pK_a value of N3 in organic solvents

Solvents may change the orientation or the binding mode of dye molecules during sensitization and aggregation.[131-132] Moreover, the performance of DSSC devices may depend on the dielectric constant of the solvent used during dye sensitization.[133] For dye sensitization, the OH bonds of the carboxylic acid groups play an important role for the dye···TiO_2 interface and intramolecular interactions, and accordingly, it should be important to evaluate the pK_a values of these COOH groups in solvents other than water.

The pK_a values of **N3** in MeOH, EtOH, MeCN, and DMSO (Table 6.6) were calculated using the same method as described in Section 6.5.2 under the assumption

that the deprotonation pathway remains unchanged.

Table 6.6. Calculated pK_a values of **N3** using the CPCM-UFF model in different solvents.

	EtOH	**MeOH**	**MeCN**	**DMSO**	**Water**
pK_a1	6.48	4.42	6.83	1.97	2.05
pK_a2	8.10	5.93	8.35	3.28	3.15
pK_a3	9.90	7.54	9.96	4.69	4.42
pK_a4	11.92	9.26	11.69	6.17	5.67
$\varepsilon^{72b,a}$	24.85	32.61	35.69	46.70	78.36
Polarity index[134]	4.0	5.1	5.8	7.2	10.2
$G_{solv,\ H+}$ [kcal/mol]	-261.23 [135]	-263.50 [135]	-260.20 [135]	-266.4 [136]	-265.90

[a] ε is the dielectric constant of the solvent.

The results show that for H_2O, MeOH, and EtOH, which share the common structure XOH (X = -H, -Me or -Et), the pK_a values decrease with increasing solvent polarity, since the electronegativity of the O atom changes from -H to -Et. MeCN and DMSO do not contain XOH bonds, and should thus exhibit different mechanisms of solute-solvent interactions, which should lead to a different trend in their pK_a values. Additionally, it should be noted that the calculated pK_a value in a specific solvent depends on the solvation free energy of the proton in that solvent.[135-136] Unfortunately, a unified way to determine the solvation free energy has not yet been developed, and therefore, the calculation will be associated with an error, *e.g.* for $G_{solv,H+}$ in DMSO, values of 266.4 and 268.64 kcal/mol have been obtained using different methods,[135-136] leading to an error of 0.91 pK_a units for the calculation of pK_a1. Thus, in a particular solvent, the specific interaction mechanism of solute and solvent needs to

be considered during the calculation to furnish more accurate pK_a values and deprotonation pathways.

6.6 Calculating the pK_a value of N3 in water using an implicit-explicit method

6.6.1 The thermodynamic cycle of dissociation in the explicit model

To more accurately describe the interactions between negatively charged ions and solvent molecules (*cf.* Sections 6.5.2 and 6.5.3), and to develop an explicit way to calculate pK_a values in solvents other than water, H_2O molecules were added explicitly to the COOH groups in the previously discussed implicit model. The direct thermodynamic circle should thus be modified according to:

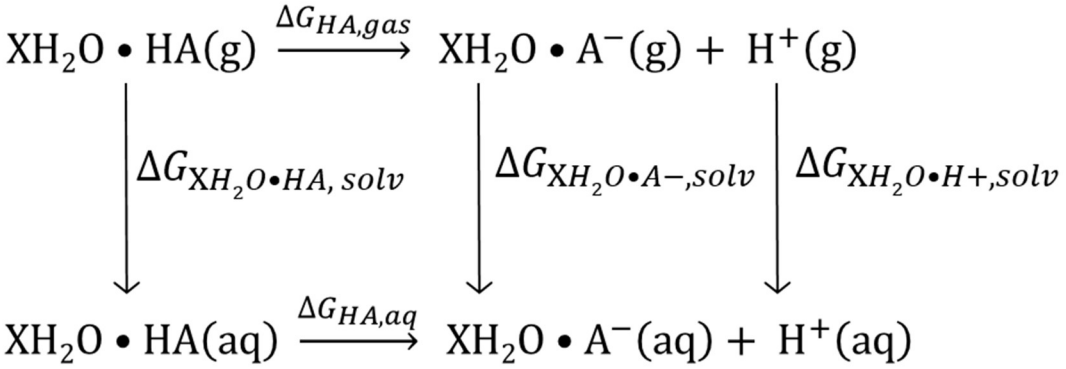

Figure 6.9 Direct thermodynamic cycle of the dissociation of HA using explicit solvent molecules on all COOH groups.

By analogy to the discussion of the thermodynamics in Section 6.4.1, the pK_a value can be calculated according to:

$$pK_a = \frac{G_{XH_2O\bullet A^-,gas} - G_{XH_2O\bullet HA,gas} + \Delta G_{XH_2O\bullet A^-,solv} - G_{XH_2O\bullet HA,solv} - 270.29}{1.3644} \qquad \text{(eq 6.13)}$$

However, for the calculations in the gas phase, errors may be induced, as the extra interactions of hydrogen bonds should not be considered in the calculation. Therefore, an explicit-assist method was adopted, i.e., the explicit model was used only to optimize the molecular geometry in solution, before the solvent molecules were removed for the subsequent calculations.

6.6.2 Calculating the pK_a value of N3 using the explicit-assist method

For these calculations, four water molecules were explicitly connected to the four COOH groups of **N3**. The optimized structures of the deprotonated forms in the deprotonation pathway (Figure 6.7) are shown in Figure 6.10.

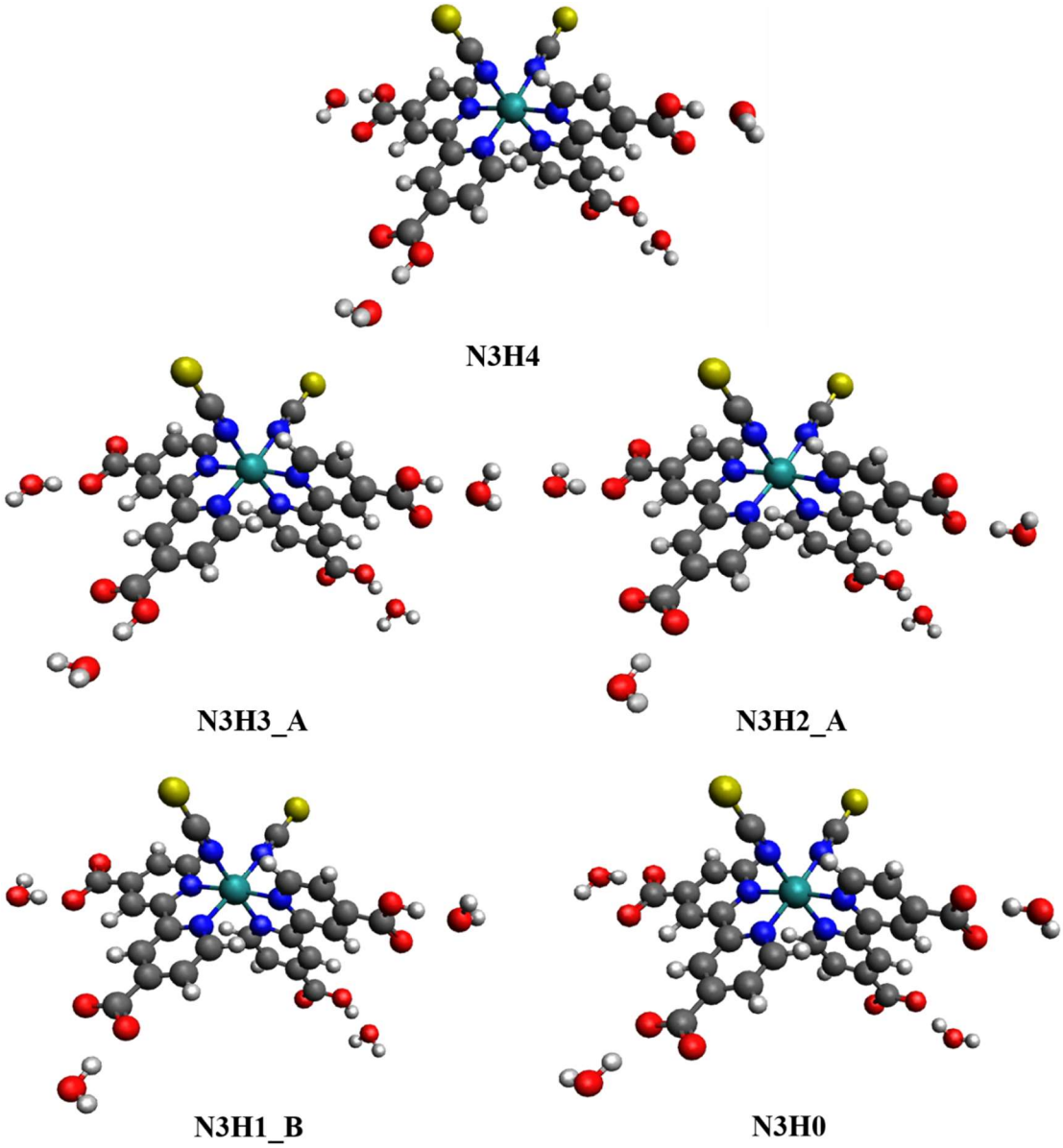

Figure 6.10. Optimized molecular structures of **N3Hx** (x = 0-4) containing four explicit water molecules in the deprotonation pathway (*cf.* Figure 6.7).

The calculated pK_a values using the explicit-assist methodology are summarized in Table 6.7. The results show that the addition of explicit water molecules affords a pK_a1 value that is much closer to the experimental result ($\Delta pK_a = 0.22$), which may be due to the modification of the geometry in solution by the explicit water molecule.

However, for the negatively charged forms **N3H2_A** and **N3H1_B**, the calculated results still deviate from the experimental results, and do not exhibit any improvement relative to those of the purely implicit method. The interactions of highly charged ions in solution therefore still require further theoretical studies to be described appropriately.

Table 6.7. Calculated pK_a values for **N3** using an explicit-assist method.

	Exp.	**Explicit-assist**	**Err.**
pK_a1	1.33	1.55	0.22
pK_a2	2.24	3.03	0.79
pK_a3	3.45	5.35	1.90
pK_a4	4.20	5.45	1.25

6.7 Conclusions

In this chapter, the deprotonation behavior of the two well-known Ru-based dyes **N3** and **N749** (Black Dye) was investigated theoretically. For **N749**, five anionic conformations were determined theoretically, which differ with respect to the deviation from linearity of the NCS ligands. Conformation **1** showed the most stable molecular structure in terms of energy, and should thus represent a good starting point for geometry optimizations. Conformations **2**-**5** show higher energies that are mainly due to the higher deviation from linearity of the N-C-S ligand, and the contraction of the N≡C bond in the NCS ligands. To investigate the deprotonation pathway of **N749**, pK_a values for all possible dissociation processes in water were calculated by DFT

methods based on an implicit model. The results show a lateral-central-lateral deprotonation pathway of the COOH groups attached to the pyridyl moieties. This pathway stands in contrast to previously reported experimental studies that have proposed a simultaneous deprotonation of two COOH groups at lateral pyridyl moieties. However, due to the limitations of the experimental conditions and the employed analysis methods, these results may not be sufficiently accurate, and therefore, more advanced experiments to measure the pK_a values of **N749** are required. Exclusively in terms of pK_a values, those calculated for **N749** in this chapter ($pK_a1 = 3.16$; $pK_a2 = 4.00$; $pK_a3 = 5.09$) are closed to the experimental results (pK_a1 and $pK_a2 = 3.3$; $pK_a3 = 5.0$).

For **N3**, based on the previously reported deprotonation pathway, five deprotonated species were theoretically studied, and their pK_a values were calculated by a purely implicit as well as an explicit-assist method. With the implicit method, the calculated pK_a values of mildly negatively charged species (**N3H4**, **N3H3_A**) show good agreement with the experimental results. However, for strongly negatively charged species (**N3H2_A** and **N3H1_B**), larger deviations were observed relative to the experimental results. With the explicit-assist method, the calculation of pK_a values of mildly negatively charged species were further improved and showed even smaller errors relative to the experimentally obtained values, whereas the pK_a values of strongly negatively charged species still require a further advanced method to describe the interactions that occur during the corresponding deprotonation processes.

Chapter 7

Conclusions and Future Work

7.1 Conclusions

This thesis has endeavored to examine structure-property relationships of dyes with respect to their application in dye-sensitized solar cells (DSSCs). Several organic and ruthenium-based dyes were investigated by experimental and computational methods.

Initially, a series of quinomethane-based dyes in solution and adsorbed on TiO_2 films was systematically investigated by means of spectroscopy, electrochemical measurements, and theoretical calculations. The investigated dyes revealed a strong intramolecular charge-transfer character and well-suited frontier molecular orbital energy values that should facilitate applications in DSSCs. Details of the dye$\cdots TiO_2$ interface were revealed by a hypsochromic shift of the major absorption peaks in the UV/vis spectrum, which indicates a deprotonation of the anchoring group during adsorption. Subsequently, this notion was further examined by DFT/TDDFT calculations, which demonstrated that the deprotonated bidentate-bridging (BB) mode is the most probable binding mode for both the carboxylic and cyanoacrylic acid

anchor groups in these dyes. Compound **2** showed the best performance in devices, and reached a conversion efficiency of 30% relative to that of the benchmark dye **N719**. This should be attributed to the dimethylaminophenyl ring, which is twisted in the excited state according to the corresponding fluorescence spectra and calculations.

Subsequently, two previously reported highly efficient carbazole-based organic dyes were investigated in order to determine the structure-property relationship that is responsible for their good performance. **MK-44**, which represents the basic building block for the MK dye series, was examined with respect to its electronic structure, potential anchoring modes, and alternative charge-transfer pathways. The computational results showed that the COO/CN (A2) anchoring mode is only slightly more stable than the BB mode, and that the anchoring modes can change from A2 to BB upon addition of Li^+ ions to the electrolyte. Furthermore, an additional charge-transfer pathway for the S···C≡N bond was reproduced by calculating bond-critical points and density of states. For the benzothiadiazole-based dye **RK-1**, the frontier molecular orbitals, intramolecular charge-transfer properties, excitation processes, and electrochemical properties were investigated. H-aggregation of **RK-1**, commensurate with a hypsochromic shift of the principal absorption peaks in the UV/vis spectra, was observed in solution and on TiO_2 films. The binding modes on TiO_2 film could not be determined unequivocally by calculations, given that the BB and the A2 modes exhibited very similar adsorption energy values.

Finally, two well-known Ru-based dyes **N3** and **N749** (Black Dye) were investigated theoretically. The most stable anionic conformation of **N749** was determined theoretically, and the energy difference between conformations was

ascribed predominantly to a twisting of the NCS ligands. Acid dissociation constants for all possible dissociation processes were calculated by DFT methods. Implicit models were adopted for **N749**, and the calculated values were closed to the experimental results, although the details of the dissociation processes require further experimental in order to draw unambiguous conclusions. For **N3**, both implicit and explicit-assistant methods were used. For species that contain moderate negative charges, calculated values with both methods showed good agreement with the experimental results, while the explicit-assist method afforded improved values. However, for the pK_a values of species that are more negatively charged, a more advanced method to describe the interactions that occur during the corresponding deprotonation processes is required.

7.2 Future work

Based on this thesis, several research avenues could be pursued to directly extend the results and conclusions obtained from this thesis.

Firstly, the performance of quinomethane-based dyes is still relatively low compared to that of Ru-based dyes. However, given that the results of the present thesis suggest that the twisting of the dimethylaminophenyl ring should be responsible for the good performance of **2**, this may offer an opportunity to design highly efficient organic dyes. A molecular engineering project based on this quinomethane structure should thus look at different combinations of donor and anchor groups that result in a similar twist of the aryl ring in the excited state, while maintaining the injection efficiency and improving the photovoltaic properties.

Secondly, the change of adsorption mode of **MK-44** upon adding Li^+ ions to the electrolyte is very unique and highly intriguing, even though the details of the underlying mechanism are still not fully understood. Furthermore, the change of adsorption mode in certain electrolytes is significant for the device performance due to its liquid working environment. Thus, to further clarify the mechanism of this process and to explore the potential application of this change, molecular dynamics calculations could be adopted to simulate this change of binding mode.

Thirdly, for calculating acid dissociation constants of **N749**, the details of the dissociation processes, i.e., the presence of a simultaneous two-proton and/or stepwise one-proton dissociations, are still unclear, and therefore, more accurate experimental measurements and more advanced data analysis methods are required. For the titration measurements, pH meters could be used to obtain more precise pH values in solution. Subsequently, a singular-value decomposition method could be used to identify absorption curves of different chromophores from the UV/vis spectra. Then, a reliable theoretical model could be developed, especially under consideration of explicit solvent molecules. As mentioned in Chapter 5, the NCS ligand *trans* to the central carboxylic acid group might play an important role for the dissociation, and explicit solvent molecules need to be connected not only to the three carboxylic acid groups, but also to the NCS ligands. Thus, a proper explicit model with solvent molecules connected to electronegative atoms is needed to calculate the acid-base properties of dye molecules.

REFERENCES

1. Chapin, D. M.; Fuller, C. S.; Pearson, G. L., A New Silicon p-n Junction Photocell for Converting Solar Radiation into Electrical Power. *Journal of Applied Physics* **1954,** *25* (5), 676-677.

2. Battaglia, C.; Cuevas, A.; De Wolf, S., High-efficiency crystalline silicon solar cells: status and perspectives. *Energy & Environmental Science* **2016,** *9* (5), 1552-1576.

3. Green, M. A.; Hishikawa, Y.; Warta, W.; Dunlop, E. D.; Levi, D. H.; Hohl-Ebinger, J.; Ho-Baillie, A. W. H., Solar cell efficiency tables (version 50). *Progress in Photovoltaics: Research and Applications* **2017,** *25* (7), 668-676.

4. Vogel, H. W., On the sensitiveness of bromide of silver to the chemically inactive colours. *Photographische Mitteilungen* **1873,** *117* (10), 233-237.

5. Terenin, A.; Putzeiko, E., Sensibilisation optique des semi-conducteurs par la chlorophylle et pigments apparentés. *J. Chim. Phys.* **1958,** *55*, 681-687.

6. Tributsch, H., Application of electrochemical kinetics to photosynthesis and oxidative phosphorylation: The redox element hypothesis and the principle of parametric energy coupling. *Journal of bioenergetics* **1971,** *2* (5), 249-273.

7. (a) Matsumura, M.; Nomura, Y.; Tsubomura, H., Dye-sensitization on the Photocurrent at Zinc Oxide Electrode in Aqueous Electrolyte Solution. *Bulletin of the Chemical Society of Japan* **1977,** *50* (10), 2533-2537; (b) Alonso V., N.; Beley, M.; Chartier, P.; Ern, V., Dye sensitization of ceramic semiconducting electrodes for photoelectrochemical conversion. *Rev. Phys. Appl. (Paris)* **1981,** *16* (1), 5-10.

8. O'Regan, B.; Grätzel, M., A low-cost, high-efficiency solar cell based on dye-sensitized colloidal TiO2 films. *Nature* **1991,** *353* (6346), 737-740.

9. (a) Mathew, S.; Yella, A.; Gao, P.; Humphry-Baker, R.; CurchodBasile, F. E.; Ashari-Astani, N.; Tavernelli, I.; Rothlisberger, U.; NazeeruddinMd, K.; Grätzel, M., Dye-sensitized solar cells with 13% efficiency achieved through the molecular engineering of porphyrin sensitizers. *Nat Chem* **2014,** *6* (3), 242-247; (b) Kakiage, K.; Aoyama, Y.; Yano, T.; Oya, K.; Fujisawa, J.-i.; Hanaya, M., Highly-efficient dye-sensitized solar cells with collaborative sensitization by silyl-anchor and carboxy-anchor dyes. *Chemical Communications* **2015,** *51* (88), 15894-15897.

10. Hagfeldt;, A.; Boschloo;, G.; Sun;, L.; Kloo;, L.; Pettersson;, H., Dye-Sensitized Solar Cells. *Chemical Reviews* **2010,** *110* (11), 6595-6663.

11. Gratzel, M., Photoelectrochemical cells. *Nature* **2001,** *414* (6861), 338-344.

12. Rowley, J.; Meyer, G. J., Reduction of I2/I3− by Titanium Dioxide. *The Journal of Physical Chemistry C* **2009,** *113* (43), 18444-18447.

13. (a) Jin, Z.; Masuda, H.; Yamanaka, N.; Minami, M.; Nakamura, T.; Nishikitani, Y., Efficient Electron Transfer Ruthenium Sensitizers for Dye-Sensitized Solar Cells. *The Journal of Physical Chemistry C* **2009,** *113* (6), 2618-2623; (b) Nazeeruddin, M. K.; Kay, A.; Rodicio, I.; Humphry-Baker, R.; Mueller, E.; Liska, P.; Vlachopoulos, N.; Graetzel, M., Conversion of light to electricity by cis-X2bis(2,2'-bipyridyl-4,4'-dicarboxylate)ruthenium(II) charge-transfer sensitizers (X = Cl-, Br-, I-, CN-, and SCN-) on nanocrystalline titanium dioxide electrodes. *Journal of the American Chemical Society* **1993,** *115* (14), 6382-6390; (c) K. Nazeeruddin, M.; Pechy, P.; Gratzel, M., Efficient panchromatic sensitization of nanocrystalline TiO2 films by a black dye based on a trithiocyanato-ruthenium complex. *Chemical Communications* **1997,** (18), 1705-1706; (d) Nazeeruddin, M. K.; De Angelis, F.; Fantacci, S.; Selloni, A.; Viscardi, G.; Liska, P.; Ito, S.; Takeru, B.; Grätzel, M., Combined Experimental and DFT-TDDFT Computational Study of Photoelectrochemical Cell Ruthenium Sensitizers. *Journal of the American Chemical Society* **2005,** *127* (48), 16835-16847.

14. (a) Xiang, W.; Huang, W.; Bach, U.; Spiccia, L., Stable high efficiency dye-sensitized solar cells based on a cobalt polymer gel electrolyte. *Chemical Communications* **2013,** *49* (79), 8997-8999; (b) El-Shafei, A.; Hussain, M.; Atiq, A.; Islam, A.; Han, L., A novel carbazole-based dye outperformed the benchmark dye

N719 for high efficiency dye-sensitized solar cells (DSSCs). *Journal of Materials Chemistry* **2012,** *22* (45), 24048-24056.

15. Thomas, K. R. J.; Lin, J. T.; Hsu, Y.-C.; Ho, K.-C., Organic dyes containing thienylfluorene conjugation for solar cells. *Chemical Communications* **2005,** (32), 4098-4100.

16. Koumura, N.; Wang, Z.-S.; Mori, S.; Miyashita, M.; Suzuki, E.; Hara, K., Alkyl-Functionalized Organic Dyes for Efficient Molecular Photovoltaics. *Journal of the American Chemical Society* **2006,** *128* (44), 14256-14257.

17. Liang, M.; Chen, J., Arylamine organic dyes for dye-sensitized solar cells. *Chemical Society Reviews* **2013,** *42* (8), 3453-3488.

18. Chen, C.-H.; Hsu, Y.-C.; Chou, H.-H.; Thomas, K. R. J.; Lin, J. T.; Hsu, C.-P., Dipolar Compounds Containing Fluorene and a Heteroaromatic Ring as the Conjugating Bridge for High-Performance Dye-Sensitized Solar Cells. *Chemistry – A European Journal* **2010,** *16* (10), 3184-3193.

19. Hara, K.; Sayama, K.; Ohga, Y.; Shinpo, A.; Suga, S.; Arakawa, H., A coumarin-derivative dye sensitized nanocrystalline TiO2 solar cell having a high solar-energy conversion efficiency up to 5.6%. *Chemical Communications* **2001,** (6), 569-570.

20. Ito, S.; Miura, H.; Uchida, S.; Takata, M.; Sumioka, K.; Liska, P.; Comte, P.; Pechy, P.; Gratzel, M., High-conversion-efficiency organic dye-sensitized solar cells with a novel indoline dye. *Chemical Communications* **2008,** (41), 5194-5196.

21. Sayama, K.; Tsukagoshi, S.; Mori, T.; Hara, K.; Ohga, Y.; Shinpou, A.; Abe, Y.; Suga, S.; Arakawa, H., Efficient sensitization of nanocrystalline TiO2 films with cyanine and merocyanine organic dyes. *Solar Energy Materials and Solar Cells* **2003,** *80* (1), 47-71.

22. Chen, Y.-S.; Li, C.; Zeng, Z.-H.; Wang, W.-B.; Wang, X.-S.; Zhang, B.-W., Efficient electron injection due to a special adsorbing group's combination of carboxyl and hydroxyl: dye-sensitized solar cells based on new hemicyanine dyes. *Journal of Materials Chemistry* **2005,** *15* (16), 1654-1661.

23. Cappel, U. B.; Karlsson, M. H.; Pschirer, N. G.; Eickemeyer, F.; Schöneboom, J.; Erk, P.; Boschloo, G.; Hagfeldt, A., A Broadly Absorbing Perylene Dye for Solid-

State Dye-Sensitized Solar Cells. *The Journal of Physical Chemistry C* **2009,** *113* (33), 14595-14597.

24. (a) Zeng, W.; Cao, Y.; Bai, Y.; Wang, Y.; Shi, Y.; Zhang, M.; Wang, F.; Pan, C.; Wang, P., Efficient Dye-Sensitized Solar Cells with an Organic Photosensitizer Featuring Orderly Conjugated Ethylenedioxythiophene and Dithienosilole Blocks. *Chemistry of Materials* **2010,** *22* (5), 1915-1925; (b) Tsao, H. N.; Burschka, J.; Yi, C.; Kessler, F.; Nazeeruddin, M. K.; Gratzel, M., Influence of the interfacial charge-transfer resistance at the counter electrode in dye-sensitized solar cells employing cobalt redox shuttles. *Energy & Environmental Science* **2011,** *4* (12), 4921-4924; (c) Wang, J.; Liu, K.; Ma, L.; Zhan, X., Triarylamine: Versatile Platform for Organic, Dye-Sensitized, and Perovskite Solar Cells. *Chemical Reviews* **2016,** *116* (23), 14675-14725.

25. Sharma, G. D.; Balraju, P.; Kumar, M.; Roy, M. S., Quasi solid state dye sensitized solar cells employing a polymer electrolyte and xanthene dyes. *Materials Science and Engineering: B* **2009,** *162* (1), 32-39.

26. Zhang, J.; Li, H.-B.; Sun, S.-L.; Geng, Y.; Wu, Y.; Su, Z.-M., Density functional theory characterization and design of high-performance diarylamine-fluorene dyes with different [small pi] spacers for dye-sensitized solar cells. *Journal of Materials Chemistry* **2012,** *22* (2), 568-576.

27. (a) Xu, M.; Wenger, S.; Bala, H.; Shi, D.; Li, R.; Zhou, Y.; Zakeeruddin, S. M.; Grätzel, M.; Wang, P., Tuning the Energy Level of Organic Sensitizers for High-Performance Dye-Sensitized Solar Cells. *The Journal of Physical Chemistry C* **2009,** *113* (7), 2966-2973; (b) Baheti, A.; Lee, C.-P.; Thomas, K. R. J.; Ho, K.-C., Pyrene-based organic dyes with thiophene containing [small pi]-linkers for dye-sensitized solar cells: optical, electrochemical and theoretical investigations. *Physical Chemistry Chemical Physics* **2011,** *13* (38), 17210-17221; (c) Hagberg, D. P.; Marinado, T.; Karlsson, K. M.; Nonomura, K.; Qin, P.; Boschloo, G.; Brinck, T.; Hagfeldt, A.; Sun, L., Tuning the HOMO and LUMO Energy Levels of Organic Chromophores for Dye Sensitized Solar Cells. *The Journal of Organic Chemistry* **2007,** *72* (25), 9550-9556.

28. Qu, S.; Wu, W.; Hua, J.; Kong, C.; Long, Y.; Tian, H., New Diketopyrrolopyrrole

(DPP) Dyes for Efficient Dye-Sensitized Solar Cells. *The Journal of Physical Chemistry C* **2010,** *114* (2), 1343-1349.

29. Wu, C.-G.; Chung, M.-F.; Tsai, H.-H. G.; Tan, C.-J.; Chen, S.-C.; Chang, C.-H.; Shih, T.-W., Fluorene-Containing Organic Photosensitizers for Dye-Sensitized Solar Cells. *ChemPlusChem* **2012,** *77* (9), 832-843.

30. Lin, J. T.; Chen, P.-C.; Yen, Y.-S.; Hsu, Y.-C.; Chou, H.-H.; Yeh, M.-C. P., Organic Dyes Containing Furan Moiety for High-Performance Dye-Sensitized Solar Cells. *Organic Letters* **2009,** *11* (1), 97-100.

31. Li, Q.; Shi, J.; Li, H.; Li, S.; Zhong, C.; Guo, F.; Peng, M.; Hua, J.; Qin, J.; Li, Z., Novel pyrrole-based dyes for dye-sensitized solar cells: From rod-shape to "H" type. *Journal of Materials Chemistry* **2012,** *22* (14), 6689-6696.

32. Bolisetty, M. N. K. P.; Li, C.-T.; Thomas, K. R. J.; Bodedla, G. B.; Ho, K.-C., Benzothiadiazole-based organic dyes with pyridine anchors for dye-sensitized solar cells: effect of donor on optical properties. *Tetrahedron* **2015,** *71* (24), 4203-4212.

33. Pei, K.; Wu, Y.; Islam, A.; Zhu, S.; Han, L.; Geng, Z.; Zhu, W., Dye-Sensitized Solar Cells Based on Quinoxaline Dyes: Effect of π-Linker on Absorption, Energy Levels, and Photovoltaic Performances. *The Journal of Physical Chemistry C* **2014,** *118* (30), 16552-16561.

34. Joly, D.; Pellejà, L.; Narbey, S.; Oswald, F.; Chiron, J.; Clifford, J. N.; Palomares, E.; Demadrille, R., A Robust Organic Dye for Dye Sensitized Solar Cells Based on Iodine/Iodide Electrolytes Combining High Efficiency and Outstanding Stability. **2014,** *4*, 4033.

35. Qu, S.; Tian, H., Diketopyrrolopyrrole (DPP)-based materials for organic photovoltaics. *Chemical Communications* **2012,** *48* (25), 3039-3051.

36. Kim, J.; Shim, H.-S.; Lee, H.; Choi, M.-S.; Kim, J.-J.; Seo, Y., Highly Efficient Vacuum-Processed Organic Solar Cells Containing Thieno[3,2-b]thiophene-thiazole. *The Journal of Physical Chemistry C* **2014,** *118* (22), 11559-11565.

37. (a) Li, R.; Lv, X.; Shi, D.; Zhou, D.; Cheng, Y.; Zhang, G.; Wang, P., Dye-Sensitized Solar Cells Based on Organic Sensitizers with Different Conjugated Linkers: Furan, Bifuran, Thiophene, Bithiophene, Selenophene, and Biselenophene.

The Journal of Physical Chemistry C **2009,** *113* (17), 7469-7479; (b) Zhang, G.; Bai, Y.; Li, R.; Shi, D.; Wenger, S.; Zakeeruddin, S. M.; Gratzel, M.; Wang, P., Employ a bisthienothiophene linker to construct an organic chromophore for efficient and stable dye-sensitized solar cells. *Energy & Environmental Science* **2009,** *2* (1), 92-95; (c) Zhang, G.; Bala, H.; Cheng, Y.; Shi, D.; Lv, X.; Yu, Q.; Wang, P., High efficiency and stable dye-sensitized solar cells with an organic chromophore featuring a binary [small pi]-conjugated spacer. *Chemical Communications* **2009,** (16), 2198-2200.

38. (a) Velusamy, M.; Justin Thomas, K. R.; Lin, J. T.; Hsu, Y.-C.; Ho, K.-C., Organic Dyes Incorporating Low-Band-Gap Chromophores for Dye-Sensitized Solar Cells. *Organic Letters* **2005,** *7* (10), 1899-1902; (b) Lu, F.; Qi, S.; Zhang, J.; Yang, G.; Zhang, B.; Feng, Y., New benzoselenadiazole-based D–A–π–A type triarylamine sensitizers for highly efficient dye-sensitized solar cells. *Dyes and Pigments* **2017,** *141*, 161-168.

39. Lee, C.-P.; Lin, R. Y.-Y.; Lin, L.-Y.; Li, C.-T.; Chu, T.-C.; Sun, S.-S.; Lin, J. T.; Ho, K.-C., Recent progress in organic sensitizers for dye-sensitized solar cells. *RSC Advances* **2015,** *5* (30), 23810-23825.

40. Zhang, L.; Cole, J. M., Anchoring Groups for Dye-Sensitized Solar Cells. *ACS Applied Materials & Interfaces* **2015,** *7* (6), 3427-3455.

41. Wiberg, J.; Marinado, T.; Hagberg, D. P.; Sun, L.; Hagfeldt, A.; Albinsson, B., Effect of Anchoring Group on Electron Injection and Recombination Dynamics in Organic Dye-Sensitized Solar Cells. *The Journal of Physical Chemistry C* **2009,** *113* (9), 3881-3886.

42. Fan, K.; Yu, J.; Ho, W., Improving photoanodes to obtain highly efficient dye-sensitized solar cells: a brief review. *Materials Horizons* **2017,** *4* (3), 319-344.

43. Mor, G. K.; Shankar, K.; Paulose, M.; Varghese, O. K.; Grimes, C. A., Use of Highly-Ordered TiO2 Nanotube Arrays in Dye-Sensitized Solar Cells. *Nano Letters* **2006,** *6* (2), 215-218.

44. Law, M.; Greene, L. E.; Johnson, J. C.; Saykally, R.; Yang, P., Nanowire dye-sensitized solar cells. *Nat Mater* **2005,** *4* (6), 455-459.

45. Yang, M.; Ding, B.; Lee, S.; Lee, J.-K., Carrier Transport in Dye-Sensitized Solar

Cells Using Single Crystalline TiO2 Nanorods Grown by a Microwave-Assisted Hydrothermal Reaction. *The Journal of Physical Chemistry C* **2011,** *115* (30), 14534-14541.

46. Liao, J.-Y.; Lin, H.-P.; Chen, H.-Y.; Kuang, D.-B.; Su, C.-Y., High-performance dye-sensitized solar cells based on hierarchical yolk-shell anatase TiO2 beads. *Journal of Materials Chemistry* **2012,** *22* (4), 1627-1633.

47. Wu, J.; Lan, Z.; Lin, J.; Huang, M.; Huang, Y.; Fan, L.; Luo, G., Electrolytes in Dye-Sensitized Solar Cells. *Chemical Reviews* **2015,** *115* (5), 2136-2173.

48. Thomas, S.; Deepak, T. G.; Anjusree, G. S.; Arun, T. A.; Nair, S. V.; Nair, A. S., A review on counter electrode materials in dye-sensitized solar cells. *Journal of Materials Chemistry A* **2014,** *2* (13), 4474-4490.

49. Beer, Bestimmung der Absorption des rothen Lichts in farbigen Flüssigkeiten. *Annalen der Physik* **1852,** *162* (5), 78-88.

50. Gagne, R. R.; Koval, C. A.; Lisensky, G. C., Ferrocene as an internal standard for electrochemical measurements. *Inorganic Chemistry* **1980,** *19* (9), 2854-2855.

51. Nyquist, H., Regeneration theory. *The Bell System Technical Journal* **1932,** *11* (1), 126-147.

52. Sarker, S.; Ahammad, A. J. S.; Seo, H. W.; Kim, D. M., Electrochemical Impedance Spectra of Dye-Sensitized Solar Cells: Fundamentals and Spreadsheet Calculation. *International Journal of Photoenergy* **2014,** *2014*, 17.

53. Wang, Q.; Moser, J.-E.; Grätzel, M., Electrochemical Impedance Spectroscopic Analysis of Dye-Sensitized Solar Cells. *The Journal of Physical Chemistry B* **2005,** *109* (31), 14945-14953.

54. Hohenberg, P.; Kohn, W., Inhomogeneous Electron Gas. *Physical Review* **1964,** *136* (3B), B864-B871.

55. (a) Levy, M., Universal variational functionals of electron densities, first-order density matrices, and natural spin-orbitals and solution of the v-representability problem. *Proceedings of the National Academy of Sciences* **1979,** *76* (12), 6062-6065; (b) Vignale, G.; Rasolt, M., Density-functional theory in strong magnetic fields. *Physical Review Letters* **1987,** *59* (20), 2360-2363.

56. Kohn, W.; Sham, L. J., Self-Consistent Equations Including Exchange and Correlation Effects. *Physical Review* **1965,** *140* (4A), A1133-A1138.

57. Perdew, J. P.; Chevary, J. A.; Vosko, S. H.; Jackson, K. A.; Pederson, M. R.; Singh, D. J.; Fiolhais, C., Atoms, molecules, solids, and surfaces: Applications of the generalized gradient approximation for exchange and correlation. *Physical Review B* **1992,** *46* (11), 6671-6687.

58. Morris, A. J.; Meyer, G. J.; Fujita, E., Molecular Approaches to the Photocatalytic Reduction of Carbon Dioxide for Solar Fuels. *Accounts of Chemical Research* **2009,** *42* (12), 1983-1994.

59. (a) Becke, A. D., Density-functional thermochemistry. III. The role of exact exchange. *The Journal of Chemical Physics* **1993,** *98* (7), 5648-5652; (b) Lee, C.; Yang, W.; Parr, R. G., Development of the Colle-Salvetti correlation-energy formula into a functional of the electron density. *Physical Review B* **1988,** *37* (2), 785-789.

60. Yanai, T.; Tew, D. P.; Handy, N. C., A new hybrid exchange–correlation functional using the Coulomb-attenuating method (CAM-B3LYP). *Chemical Physics Letters* **2004,** *393* (1), 51-57.

61. (a) Zhao, Y.; Truhlar, D. G., The M06 suite of density functionals for main group thermochemistry, thermochemical kinetics, noncovalent interactions, excited states, and transition elements: two new functionals and systematic testing of four M06-class functionals and 12 other functionals. *Theoretical Chemistry Accounts* **2008,** *120* (1), 215-241; (b) Zhao, Y.; Truhlar, D. G., Density Functionals with Broad Applicability in Chemistry. *Accounts of Chemical Research* **2008,** *41* (2), 157-167.

62. Slater, J. C., Atomic Shielding Constants. *Physical Review* **1930,** *36* (1), 57-64.

63. Gill, P. M. W., Molecular integrals Over Gaussian Basis Functions. *Advances in Quantum Chemistry* **1994,** *25*, 141-205.

64. Ditchfield, R.; Hehre, W. J.; Pople, J. A., Self-Consistent Molecular-Orbital Methods. IX. An Extended Gaussian-Type Basis for Molecular-Orbital Studies of Organic Molecules. *The Journal of Chemical Physics* **1971,** *54* (2), 724-728.

65. Dunning, T. H., Gaussian basis sets for use in correlated molecular calculations. I. The atoms boron through neon and hydrogen. *The Journal of Chemical Physics* **1989,**

90 (2), 1007-1023.

66. Runge, E.; Gross, E. K. U., Density-Functional Theory for Time-Dependent Systems. *Physical Review Letters* **1984,** *52* (12), 997-1000.

67. van Leeuwen, R., Causality and Symmetry in Time-Dependent Density-Functional Theory. *Physical Review Letters* **1998,** *80* (6), 1280-1283.

68. Cole, J. M.; Low, K. S.; Ozoe, H.; Stathi, P.; Kitamura, C.; Kurata, H.; Rudolf, P.; Kawase, T., Data mining with molecular design rules identifies new class of dyes for dye-sensitised solar cells. *Physical Chemistry Chemical Physics* **2014,** *16* (48), 26684-26690.

69. O'Regan, B.; Xiaoe, L.; Ghaddar, T., Dye adsorption, desorption, and distribution in mesoporous TiO2 films, and its effects on recombination losses in dye sensitized solar cells. *Energy & Environmental Science* **2012,** *5* (5), 7203-7215.

70. M. J. Frisch, G. W. T., H. B. Schlegel, G. E. Scuseria, M. A. Robb, J. R. Cheeseman, G. Scalmani, V. Barone, G. A. Petersson, H. Nakatsuji, X. Li, M. Caricato, A. Marenich, J. Bloino, B. G. Janesko, R. Gomperts, B. Mennucci, H. P. Hratchian, J. V. Ortiz, A. F. Izmaylov, J. L. Sonnenberg, D. Williams-Young, F. Ding, F. Lipparini, F. Egidi, J. Goings, B. Peng, A. Petrone, T. Henderson, D. Ranasinghe, V. G. Zakrzewski, J. Gao, N. Rega, G. Zheng, W. Liang, M. Hada, M. Ehara, K. Toyota, R. Fukuda, J. Hasegawa, M. Ishida, T. Nakajima, Y. Honda, O. Kitao, H. Nakai, T. Vreven, K. Throssell, J. A. Montgomery, Jr., J. E. Peralta, F. Ogliaro, M. Bearpark, J. J. Heyd, E. Brothers, K. N. Kudin, V. N. Staroverov, T. Keith, R. Kobayashi, J. Normand, K. Raghavachari, A. Rendell, J. C. Burant, S. S. Iyengar, J. Tomasi, M. Cossi, J. M. Millam, M. Klene, C. Adamo, R. Cammi, J. W. Ochterski, R. L. Martin, K. Morokuma, O. Farkas, J. B. Foresman, D. J. Fox,, *Gaussian, Inc., Wallingford CT* **2016,** *Gaussian 09, Revision A.02*.

71. Hariharan, P. C.; Pople, J. A., The influence of polarization functions on molecular orbital hydrogenation energies. *Theoretica chimica acta* **1973,** *28* (3), 213-222.

72. (a) Chipman, D. M., Reaction field treatment of charge penetration. *The Journal of Chemical Physics* **2000,** *112* (13), 5558-5565; (b) Miertuš, S.; Scrocco, E.; Tomasi,

J., Electrostatic interaction of a solute with a continuum. A direct utilizaion of AB initio molecular potentials for the prevision of solvent effects. *Chemical Physics* **1981,** *55* (1), 117-129.

73. Sanchez-de-Armas, R.; San Miguel, M. A.; Oviedo, J.; Sanz, J. F., Coumarin derivatives for dye sensitized solar cells: a TD-DFT study. *Physical Chemistry Chemical Physics* **2012,** *14* (1), 225-233.

74. Galoppini, E., Linkers for anchoring sensitizers to semiconductor nanoparticles. *Coordination Chemistry Reviews* **2004,** *248* (13), 1283-1297.

75. (a) Haid, S.; Marszalek, M.; Mishra, A.; Wielopolski, M.; Teuscher, J.; Moser, J.-E.; Humphry-Baker, R.; Zakeeruddin, S. M.; Grätzel, M.; Bäuerle, P., Significant Improvement of Dye-Sensitized Solar Cell Performance by Small Structural Modification in π-Conjugated Donor–Acceptor Dyes. *Advanced Functional Materials* **2012,** *22* (6), 1291-1302; (b) Ma, W.; Jiao, Y.; Meng, S., Modeling charge recombination in dye-sensitized solar cells using first-principles electron dynamics: effects of structural modification. *Physical Chemistry Chemical Physics* **2013,** *15* (40), 17187-17194.

76. Allen, F. H.; Kennard, O.; Watson, D. G.; Brammer, L.; Orpen, A. G.; Taylor, R., Tables of bond lengths determined by X-ray and neutron diffraction. Part 1. Bond lengths in organic compounds. *Journal of the Chemical Society, Perkin Transactions 2* **1987,** (12), S1-S19.

77. Malagoli, M.; Brédas, J. L., Density functional theory study of the geometric structure and energetics of triphenylamine-based hole-transporting molecules. *Chemical Physics Letters* **2000,** *327* (1–2), 13-17.

78. Zhang, G.; Musgrave, C. B., Comparison of DFT Methods for Molecular Orbital Eigenvalue Calculations. *The Journal of Physical Chemistry A* **2007,** *111* (8), 1554-1561.

79. Gorman, C. B.; Marder, S. R., An investigation of the interrelationships between linear and nonlinear polarizabilities and bond-length alternation in conjugated organic molecules. *Proceedings of the National Academy of Sciences of the United States of America* **1993,** *90* (23), 11297-11301.

80. Jacquemin, D.; Perpète, E. A.; Scalmani, G.; Frisch, M. J.; Assfeld, X.; Ciofini, I.; Adamo, C., Time-dependent density functional theory investigation of the absorption, fluorescence, and phosphorescence spectra of solvated coumarins. *The Journal of Chemical Physics* **2006,** *125* (16), 164324.

81. Kim, S.; Lee, J. K.; Kang, S. O.; Ko, J.; Yum, J. H.; Fantacci, S.; De Angelis, F.; Di Censo, D.; Nazeeruddin, M. K.; Grätzel, M., Molecular Engineering of Organic Sensitizers for Solar Cell Applications. *Journal of the American Chemical Society* **2006,** *128* (51), 16701-16707.

82. Lu, T.; Chen, F., Multiwfn: A multifunctional wavefunction analyzer. *Journal of Computational Chemistry* **2012,** *33* (5), 580-592.

83. Zhang, F.; Ma, W.; Jiao, Y.; Wang, J.; Shan, X.; Li, H.; Lu, X.; Meng, S., Precise Identification and Manipulation of Adsorption Geometry of Donor−π–Acceptor Dye on Nanocrystalline TiO2 Films for Improved Photovoltaics. *ACS Applied Materials & Interfaces* **2014,** *6* (24), 22359-22369.

84. Sasaki, S.; Drummen, G. P. C.; Konishi, G.-i., Recent advances in twisted intramolecular charge transfer (TICT) fluorescence and related phenomena in materials chemistry. *Journal of Materials Chemistry C* **2016,** *4* (14), 2731-2743.

85. Wang, Z.-S.; Koumura, N.; Cui, Y.; Takahashi, M.; Sekiguchi, H.; Mori, A.; Kubo, T.; Furube, A.; Hara, K., Hexylthiophene-Functionalized Carbazole Dyes for Efficient Molecular Photovoltaics: Tuning of Solar-Cell Performance by Structural Modification. *Chemistry of Materials* **2008,** *20* (12), 3993-4003.

86. Miyashita, M.; Sunahara, K.; Nishikawa, T.; Uemura, Y.; Koumura, N.; Hara, K.; Mori, A.; Abe, T.; Suzuki, E.; Mori, S., Interfacial Electron-Transfer Kinetics in Metal-Free Organic Dye-Sensitized Solar Cells: Combined Effects of Molecular Structure of Dyes and Electrolytes. *Journal of the American Chemical Society* **2008,** *130* (52), 17874-17881.

87. Hara, K.; Wang, Z.-S.; Cui, Y.; Furube, A.; Koumura, N., Long-term stability of organic-dye-sensitized solar cells based on an alkyl-functionalized carbazole dye. *Energy & Environmental Science* **2009,** *2* (10), 1109-1114.

88. (a) Kashif, M. K.; Axelson, J. C.; Duffy, N. W.; Forsyth, C. M.; Chang, C. J.;

Long, J. R.; Spiccia, L.; Bach, U., A New Direction in Dye-Sensitized Solar Cells Redox Mediator Development: In Situ Fine-Tuning of the Cobalt(II)/(III) Redox Potential through Lewis Base Interactions. *Journal of the American Chemical Society* **2012,** *134* (40), 16646-16653; (b) Kashif, M. K.; Nippe, M.; Duffy, N. W.; Forsyth, C. M.; Chang, C. J.; Long, J. R.; Spiccia, L.; Bach, U., Stable Dye-Sensitized Solar Cell Electrolytes Based on Cobalt(II)/(III) Complexes of a Hexadentate Pyridyl Ligand. *Angewandte Chemie International Edition* **2013,** *52* (21), 5527-5531; (c) Murakami, T. N.; Koumura, N.; Uchiyama, T.; Uemura, Y.; Obuchi, K.; Masaki, N.; Kimura, M.; Mori, S., Recombination inhibitive structure of organic dyes for cobalt complex redox electrolytes in dye-sensitised solar cells. *Journal of Materials Chemistry A* **2013,** *1* (3), 792-798.

89. Daeneke, T.; Uemura, Y.; Duffy, N. W.; Mozer, A. J.; Koumura, N.; Bach, U.; Spiccia, L., Aqueous Dye-Sensitized Solar Cell Electrolytes Based on the Ferricyanide–Ferrocyanide Redox Couple. *Advanced Materials* **2012,** *24* (9), 1222-1225.

90. Frisch, M. J. T., G. W.; Schlegel, H. B.; Scuseria, G. E.; Robb, M. A.; Cheeseman, J. R.; Scalmani, G.; Barone, V.; Mennucci, B.; Petersson, G. A.; Nakatsuji, H.; Caricato, M.; Li, X.; Hratchian, H. P.; Izmaylov, A. F.; Bloino, J.; Zheng, G.; Sonnenberg, J. L.; Hada, M.; Ehara, M.; Toyota, K.; Fukuda, R.; Hasegawa, J.; Ishida, M.; Nakajima, T.; Honda, Y.; Kitao, O.; Nakai, H.; Vreven, T.; Montgomery, Jr., J. A.; Peralta, J. E.; Ogliaro, F.; Bearpark, M.; Heyd, J. J.; Brothers, E.; Kudin, K. N.; Staroverov, V. N.; Kobayashi, R.; Normand, J.; Raghavachari, K.; Rendell, A.; Burant, J. C.; Iyengar, S. S.; Tomasi, J.; Cossi, M.; Rega, N.; Millam, J. M.; Klene, M.; Knox, J. E.; Cross, J. B.; Bakken, V.; Adamo, C.; Jaramillo, J.; Gomperts, R.; Stratmann, R. E.; Yazyev, O.; Austin, A. J.; Cammi, R.; Pomelli, C.; Ochterski, J. W.; Martin, R. L.; Morokuma, K.; Zakrzewski, V. G.; Voth, G. A.; Salvador, P.; Dannenberg, J. J.; Dapprich, S.; Daniels, A. D.; Farkas, Ö ; Foresman, J. B.; Ortiz, J. V.; Cioslowski, J.; Fox, D. J. Gaussian, Inc., Wallingford CT, Gaussian, version Gaussian.09W (accessed 2009).

91. Zhang, L.; Cole, J. M., Adsorption Properties of p-Methyl Red Monomeric-to-

Pentameric Dye Aggregates on Anatase (101) Titania Surfaces: First-Principles Calculations of Dye/TiO2 Photoanode Interfaces for Dye-Sensitized Solar Cells. *ACS Applied Materials & Interfaces* **2014,** *6* (18), 15760-15766.

92. Chai, J.-D.; Head-Gordon, M., Systematic optimization of long-range corrected hybrid density functionals. *The Journal of Chemical Physics* **2008,** *128* (8), 084106.

93. Chai, J.-D.; Head-Gordon, M., Long-range corrected hybrid density functionals with damped atom-atom dispersion corrections. *Physical Chemistry Chemical Physics* **2008,** *10* (44), 6615-6620.

94. Iikura, H.; Tsuneda, T.; Yanai, T.; Hirao, K., A long-range correction scheme for generalized-gradient-approximation exchange functionals. *The Journal of Chemical Physics* **2001,** *115* (8), 3540-3544.

95. Perdew, J. P.; Burke, K.; Ernzerhof, M., Generalized Gradient Approximation Made Simple. *Physical Review Letters* **1996,** *77* (18), 3865-3868.

96. Vydrov, O. A.; Scuseria, G. E., Assessment of a long-range corrected hybrid functional. *The Journal of Chemical Physics* **2006,** *125* (23), 234109.

97. Liechtenstein, A. I.; Katsnelson, M. I.; Antropov, V. P.; Gubanov, V. A., Local spin density functional approach to the theory of exchange interactions in ferromagnetic metals and alloys. *Journal of Magnetism and Magnetic Materials* **1987,** *67* (1), 65-74.

98. Adamo, C.; Barone, V., Exchange functionals with improved long-range behavior and adiabatic connection methods without adjustable parameters: The mPW and mPW1PW models. *The Journal of Chemical Physics* **1998,** *108* (2), 664-675.

99. Heyd, J.; Scuseria, G. E., Efficient hybrid density functional calculations in solids: Assessment of the Heyd–Scuseria–Ernzerhof screened Coulomb hybrid functional. *The Journal of Chemical Physics* **2004,** *121* (3), 1187-1192.

100. Hamprecht, F. A.; Cohen, A. J.; Tozer, D. J.; Handy, N. C., Development and assessment of new exchange-correlation functionals. *The Journal of Chemical Physics* **1998,** *109* (15), 6264-6271.

101. Tao, J.; Perdew, J. P.; Staroverov, V. N.; Scuseria, G. E., Climbing the Density Functional Ladder: Nonempirical Meta\char21{}Generalized Gradient

Approximation Designed for Molecules and Solids. *Physical Review Letters* **2003,** *91* (14), 146401.

102. Valiev, M.; Bylaska, E. J.; Govind, N.; Kowalski, K.; Straatsma, T. P.; Van Dam, H. J. J.; Wang, D.; Nieplocha, J.; Apra, E.; Windus, T. L.; de Jong, W. A., NWChem: A comprehensive and scalable open-source solution for large scale molecular simulations. *Computer Physics Communications* **2010,** *181* (9), 1477-1489.

103. Ronca, E.; Pastore, M.; Belpassi, L.; Tarantelli, F.; De Angelis, F., Influence of the dye molecular structure on the TiO2 conduction band in dye-sensitized solar cells: disentangling charge transfer and electrostatic effects. *Energy & Environmental Science* **2013,** *6* (1), 183-193.

104. Collins, J. B.; von R. Schleyer, P.; Binkley, J. S.; Pople, J. A., Self-consistent molecular orbital methods. XVII. Geometries and binding energies of second-row molecules. A comparison of three basis sets. *The Journal of Chemical Physics* **1976,** *64* (12), 5142-5151.

105. Goerigk, L.; Grimme, S., Assessment of TD-DFT methods and of various spin scaled CIS(D) and CC2 versions for the treatment of low-lying valence excitations of large organic dyes. *The Journal of Chemical Physics* **2010,** *132* (18), 184103.

106. (a) Lu, X.; Feng, Q.; Lan, T.; Zhou, G.; Wang, Z.-S., Molecular Engineering of Quinoxaline-Based Organic Sensitizers for Highly Efficient and Stable Dye-Sensitized Solar Cells. *Chemistry of Materials* **2012,** *24* (16), 3179-3187; (b) Lu, X.; Jia, X.; Wang, Z.-S.; Zhou, G., X-shaped organic dyes with a quinoxaline bridge for use in dye-sensitized solar cells. *Journal of Materials Chemistry A* **2013,** *1* (34), 9697-9706.

107. McCree-Grey, J.; Cole, J.; Holt, S.; Evans, P. J.; Gong, Y., Dye...TiO2 Interfacial Structure of Dye-Sensitised Solar Cell Working Electrodes Buried under a Solution of I-/I3- Redox Electrolyte. *Nanoscale* **2017**.

108. Furube, A.; Katoh, R.; Hara, K.; Sato, T.; Murata, S.; Arakawa, H.; Tachiya, M., Lithium Ion Effect on Electron Injection from a Photoexcited Coumarin Derivative into a TiO2 Nanocrystalline Film Investigated by Visible-to-IR Ultrafast

Spectroscopy. *The Journal of Physical Chemistry B* **2005,** *109* (34), 16406-16414.

109. Cole, J. M.; Blood-Forsythe, M. A.; Lin, T.-C.; Pattison, P.; Gong, Y.; Vázquez-Mayagoitia, Á.; Waddell, P. G.; Zhang, L.; Koumura, N.; Mori, S., Discovery of S···C≡N Intramolecular Bonding in a Thiophenylcyanoacrylate-Based Dye: Realizing Charge Transfer Pathways and Dye···TiO2 Anchoring Characteristics for Dye-Sensitized Solar Cells. *ACS Applied Materials & Interfaces* **2017,** *9* (31), 25952-25961.

110.(a) Bader, R. F. W., A quantum theory of molecular structure and its applications. *Chemical Reviews* **1991,** *91* (5), 893-928; (b) Bader, R. F. W., The Quantum Mechanical Basis of Conceptual Chemistry. *Monatshefte für Chemie / Chemical Monthly* **2005,** *136* (6), 819-854.

111. Idigoras, J.; Godfroy, M.; Joly, D.; Todinova, A.; Maldivi, P.; Oskam, G.; Demadrille, R.; Anta, J. A., Organic dyes for the sensitization of nanostructured ZnO photoanodes: effect of the anchoring functions. *RSC Advances* **2015,** *5* (84), 68929-68938.

112. Eisfeld, A.; Briggs, J. S., The J- and H-bands of organic dye aggregates. *Chemical Physics* **2006,** *324* (2), 376-384.

113.(a) O'Regan, B.; Gratzel, M., A low-cost, high-efficiency solar cell based on dye-sensitized colloidal TiO2 films. *Nature* **1991,** *353* (6346), 737-740; (b) Nazeeruddin, M. K.; Baranoff, E.; Grätzel, M., Dye-sensitized solar cells: A brief overview. *Solar Energy* **2011,** *85* (6), 1172-1178.

114. Grätzel, M., Recent Advances in Sensitized Mesoscopic Solar Cells. *Accounts of Chemical Research* **2009,** *42* (11), 1788-1798.

115.(a) Yin, J.-F.; Velayudham, M.; Bhattacharya, D.; Lin, H.-C.; Lu, K.-L., Structure optimization of ruthenium photosensitizers for efficient dye-sensitized solar cells – A goal toward a “bright” future. *Coordination Chemistry Reviews* **2012,** *256* (23), 3008-3035; (b) Zhang, C.-R.; Han, L.-H.; Zhe, J.-W.; Jin, N.-Z.; Wang, D.-B.; Wang, X.; Wu, Y.-Z.; Chen, Y.-H.; Liu, Z.-J.; Chen, H.-S., Tuning the electronic structures and related properties of Ruthenium-based dye sensitizers by ligands: A theoretical study and design. *Computational and Theoretical Chemistry* **2013,** *1017*, 99-108.

116.(a) Lee, K. E.; Gomez, M. A.; Elouatik, S.; Demopoulos, G. P., Further Understanding of the Adsorption Mechanism of N719 Sensitizer on Anatase TiO2 Films for DSSC Applications Using Vibrational Spectroscopy and Confocal Raman Imaging. *Langmuir* **2010,** *26* (12), 9575-9583; (b) De Angelis, F.; Fantacci, S.; Selloni, A.; Nazeeruddin, M. K.; Grätzel, M., First-Principles Modeling of the Adsorption Geometry and Electronic Structure of Ru(II) Dyes on Extended TiO2 Substrates for Dye-Sensitized Solar Cell Applications. *The Journal of Physical Chemistry C* **2010,** *114* (13), 6054-6061; (c) Hirose, F.; Kuribayashi, K.; Shikaku, M.; Narita, Y., In Situ Observation of N719 on TiO2 in Dye-Sensitized Solar Cells by IR Absorption Spectroscopy. *Electrochemical and Solid-State Letters* **2009,** *12* (12), B167-B170; (d) Schiffmann, F.; VandeVondele, J.; Hutter, J.; Wirz, R.; Urakawa, A.; Baiker, A., Protonation-Dependent Binding of Ruthenium Bipyridyl Complexes to the Anatase(101) Surface. *The Journal of Physical Chemistry C* **2010,** *114* (18), 8398-8404; (e) Zuleta, M.; Edvinsson, T.; Yu, S.; Ahmadi, S.; Boschloo, G.; Gothelid, M.; Hagfeldt, A., Light-induced rearrangements of chemisorbed dyes on anatase(101). *Physical Chemistry Chemical Physics* **2012,** *14* (30), 10780-10788.

117.Cole, J. M.; Low, K. S.; Gong, Y., Discovery of Black Dye Crystal Structure Polymorphs: Implications for Dye Conformational Variation in Dye-Sensitized Solar Cells. *ACS Applied Materials & Interfaces* **2015,** *7* (50), 27646-27653.

118.(a) McCree-Grey, J.; Cole, J. M.; Evans, P. J., Preferred Molecular Orientation of Coumarin 343 on TiO2 Surfaces: Application to Dye-Sensitized Solar Cells. *ACS Applied Materials & Interfaces* **2015,** *7* (30), 16404-16409; (b) McCree-Grey, J.; Cole, J. M.; Holt, S. A.; Evans, P. J.; Gong, Y., Dye[three dots, centered]TiO2 interfacial structure of dye-sensitised solar cell working electrodes buried under a solution of I-/I3- redox electrolyte. *Nanoscale* **2017,** *9* (32), 11793-11805.

119.Hay, P. J.; Wadt, W. R., Ab initio effective core potentials for molecular calculations. Potentials for K to Au including the outermost core orbitals. *The Journal of Chemical Physics* **1985,** *82* (1), 299-310.

120. Marenich, A. V.; Cramer, C. J.; Truhlar, D. G., Universal Solvation Model Based on Solute Electron Density and on a Continuum Model of the Solvent Defined

by the Bulk Dielectric Constant and Atomic Surface Tensions. *The Journal of Physical Chemistry B* **2009,** *113* (18), 6378-6396.

121. Cossi, M.; Barone, V.; Cammi, R.; Tomasi, J., Ab initio study of solvated molecules: a new implementation of the polarizable continuum model. *Chemical Physics Letters* **1996,** *255* (4), 327-335.

122. Hagfeldt, A.; Boschloo, G.; Sun, L.; Kloo, L.; Pettersson, H., Dye-Sensitized Solar Cells. *Chemical Reviews* **2010,** *110* (11), 6595-6663.

123. Shklover, V.; Nazeeruddin, M. K.; Grätzel, M.; Ovchinnikov, Y. E., Packing of ruthenium sensitizer molecules on mostly exposed faces of nanocrystalline TiO2: crystal structure of (NBu4+)2[Ru(H2tctterpy)(NCS)3]2−·0.5 DMSO. *Applied Organometallic Chemistry* **2002,** *16* (11), 635-642.

124. Ghosh, S.; Chaitanya, G. K.; Bhanuprakash, K.; Nazeeruddin, M. K.; Grätzel, M.; Reddy, P. Y., Electronic Structures and Absorption Spectra of Linkage Isomers of Trithiocyanato (4,4‘,4‘ ‘-Tricarboxy-2,2‘:6,2‘ ‘-terpyridine) Ruthenium(II) Complexes: A DFT Study. *Inorganic Chemistry* **2006,** *45* (19), 7600-7611.

125. Sutton, C. C. R.; Franks, G. V.; da Silva, G., First Principles pKa Calculations on Carboxylic Acids Using the SMD Solvation Model: Effect of Thermodynamic Cycle, Model Chemistry, and Explicit Solvent Molecules. *The Journal of Physical Chemistry B* **2012,** *116* (39), 11999-12006.

126. (a) Pizzoli, G.; Lobello, M. G.; Carlotti, B.; Elisei, F.; Nazeeruddin, M. K.; Vitillaro, G.; De Angelis, F., Acid-base properties of the N3 ruthenium(ii) solar cell sensitizer: a combined experimental and computational analysis. *Dalton Transactions* **2012,** *41* (38), 11841-11848; (b) Fantacci, S.; Lobello, M. G.; De Angelis, F., Everything you always wanted to Know about Black Dye (but Were Afraid to Ask): A DFT/TDDFT Investigation. *CHIMIA International Journal for Chemistry* **2013,** *67* (3), 121-128.

127. Thapa, B.; Schlegel, H. B., Calculations of pKa’s and Redox Potentials of Nucleobases with Explicit Waters and Polarizable Continuum Solvation. *The Journal of Physical Chemistry A* **2015,** *119* (21), 5134-5144.

128. Topol, I. A.; Tawa, G. J.; Burt, S. K.; Rashin, A. A., On the structure and

thermodynamics of solvated monoatomic ions using a hybrid solvation model. *The Journal of Chemical Physics* **1999,** *111* (24), 10998-11014.

129. Ho, J.; Klamt, A.; Coote, M. L., Comment on the Correct Use of Continuum Solvent Models. *The Journal of Physical Chemistry A* **2010,** *114* (51), 13442-13444.

130. Nazeeruddin, M. K.; Péchy, P.; Renouard, T.; Zakeeruddin, S. M.; Humphry-Baker, R.; Comte, P.; Liska, P.; Cevey, L.; Costa, E.; Shklover, V.; Spiccia, L.; Deacon, G. B.; Bignozzi, C. A.; Grätzel, M., Engineering of Efficient Panchromatic Sensitizers for Nanocrystalline TiO2-Based Solar Cells. *Journal of the American Chemical Society* **2001,** *123* (8), 1613-1624.

131. Nazeeruddin, M. K.; Zakeeruddin, S. M.; Humphry-Baker, R.; Jirousek, M.; Liska, P.; Vlachopoulos, N.; Shklover, V.; Fischer, C.-H.; Grätzel, M., Acid−Base Equilibria of (2,2‘-Bipyridyl-4,4‘-dicarboxylic acid)ruthenium(II) Complexes and the Effect of Protonation on Charge-Transfer Sensitization of Nanocrystalline Titania. *Inorganic Chemistry* **1999,** *38* (26), 6298-6305.

132. Mosconi, E.; Selloni, A.; De Angelis, F., Solvent Effects on the Adsorption Geometry and Electronic Structure of Dye-Sensitized TiO2: A First-Principles Investigation. *The Journal of Physical Chemistry C* **2012,** *116* (9), 5932-5940.

133. Ozawa, H.; Awa, M.; Ono, T.; Arakawa, H., Effects of Dye-Adsorption Solvent on the Performances of the Dye-Sensitized Solar Cells Based on Black Dye. *Chemistry – An Asian Journal* **2012,** *7* (1), 156-162.

134. Balaban, A. T., Book Review of Solvents and Solvent Effects in Organic Chemistry, 4th ed. *Journal of the American Chemical Society* **2011,** *133* (20), 8058-8058.

135. Kelly, C. P.; Cramer, C. J.; Truhlar, D. G., Single-Ion Solvation Free Energies and the Normal Hydrogen Electrode Potential in Methanol, Acetonitrile, and Dimethyl Sulfoxide. *The Journal of Physical Chemistry B* **2007,** *111* (2), 408-422.

136. Rossini, E.; Knapp, E.-W., Proton solvation in protic and aprotic solvents. *Journal of Computational Chemistry* **2016,** *37* (12), 1082-1091.

APPENDIX

A Fabrication of Dye-Sensitized Solar Cell devices

A1 Unsealed Fabrication

A1.1 Preparation Method

(I) Glass cutting and marking

(i) The expected photoanode size is ~1.5 cm × 1.0 cm, with an inner active area of 1 cm × 1 cm. Initially, the FTO glass is cut into pieces of 3.0 cm × 4.0 cm, before Scotch tape is added (*cf.* Figure 2.2) and every electrode is numbered.

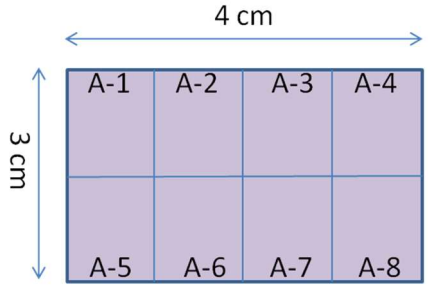

Figure A1. Scheme for the Scotch taping of 3.0 cm × 4.0 cm FTO glass.

(ii) The counter electrode size is ~1.5 cm × 1.75 cm, with an inner active area of 1.5 cm × 1.75 cm. As in step 1, the FTO glass is cut into parts of 3.0 cm × 7.0 cm, before Scotch taping this part slightly (Figure 2.2), and numbering every electrode.

(iii) Before cutting, a multimeter is used to ensure that the FTO is face down. Any contact with e.g. metal rulers or metal tweezers with the FTO should be avoided, as this may compromise the surface. Special care should be taken with tiny shards of

FTO glass on the desk surface, as these may damage and the FTO conductive layer and/or yourself.

(II) Glass Cleaning

(i) The glass pieces are placed in an detergent solution (2 L) that contains 10 mL Decon and deionised (DI) water, and sonicated for ~15 min.

(ii) The glass pieces are washed with DI water, placed in more DI water, and sonicated again for ~15 min.

(iii) The glass is put in ethanol and sonicated for ~15 min.

A1.2 Fabrication of Photoanodes

(I). Doctor-blading and Sintering TiO_2 Paste

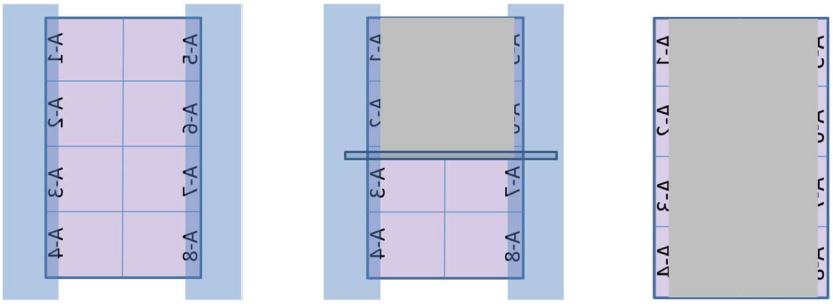

(a) (b) (c)

Figure A2. Schematic illustration of the doctor-blading process. (a) Fixing the FTO glass with 3M tape. (b) Doctor-blading the titania paste on the exposed are. (c) Removing the tape after doctor-blading is finished.

(i) A multimeter was used to ensure that the FTO side of the glass was facing upwards.

(ii) Two strips of 3M magic tape were deposited at the left/right side of the FTO glass surface for masking purposes (Figure A2a), and the tapes were pressed down with a stirring rod to expunge air bubbles.

(iii) TiO_2 paste was deposited with a cocktail stick onto the upward facing surface of the fixed FTO glass.

(iv) A stirring rod was used to doctor-blade the TiO_2 layer, sliding the paste down the glass smoothly (Figure A2b to A2c). And then remove 3M strip.
(v) The FTO glass with TiO_2 paste was loaded into an oven, and the temperature was increased from room temperature to 500 °C (temperature gradient: ca. 8 °C/min), where it was for 30 min for sintering purposes.
(vi) After cooling the electrode, (i)-(v) were repeated to increase the number of layers of TiO_2.

(II). Sensitization

(1) Dye solutions (0.5 mM) in a suitable solvent (MeOH for Ru-based dyes N3/N719) were prepared.
(2) The dye solution was transferred into a petri dish, before the TiO_2-coated FTO glass was fully immersed in the solution. The petri dish was sealed with parafilm and left overnight.

A1.3 Fabrication of Pt Counter Electrodes

(I) Preparation of H_2PtCl_6 Solutions

(i) Chloroplatinic acid hexahydrate ($H_2PtCl_6 \cdot 6H_2O$) was dissolved in isopropanol to reach a final concentration of 52 mM.

(II) Doctor-blading and sintering H_2PtCl_6 Solution

(i) A multimeter was used to ensure that the FTO side of the glass was facing upwards.
(ii) Two strips of 3M magic tape were deposited at the left/right side of the FTO glass surface for masking purposes (Figure A2a), and the tapes were pressed down with a stirring rod to expunge air bubbles.
(iii) Chloroplatinic acid was deposited along the top edge on the coated side of the FTO glass. A glass pipette was used to spread the material in a downward motion on the surface. The glass was subsequently heated slowly to avoid cracking.
(iv) The FTO glass was slowly heated (15 ºC/min) to 385 ºC, where it was kept for 30 min.

A1.4 Assembling DSSCs

(I) One or two drops of electrolyte were deposited onto the sensitized photoanodes.

(II) Bulldog clips were used to press the mask, photoanode and counter electrode from both sides (Figure A3).

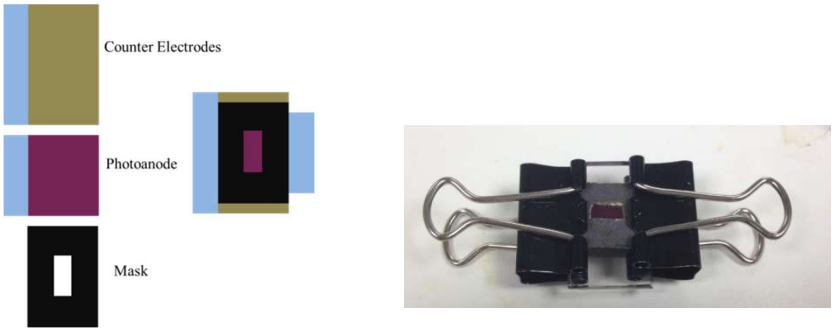

Figure A3. Schematic illustration of the assembling of DSSCs.

A2 Sealed Fabrication

A2.1 Preparation

(I) Glass cutting and hole drilling.

(i) An electrode (~2 cm x 1.5 cm; inner active area size: 1 cm x 1 cm) was used.

(ii) Holes were drilled from both sides of the FTO glass to avoid breaking.

(II) Glass cleaning

The same as step in A1.1, Preparation, (II).

A2.2 Fabrication of Photoanodes

(I) Doctor-blading and Sintering TiO_2 Paste

(i) Use a multimeter to make sure the FTO side of the glass is face up.

(ii) Put two strips of 3M magic tape at the left/right side of the FTO glass for masking purposes.

(iii) Transfer TiO_2 paste onto the top of the electrode.

(iv) Use a pipette to doctor-blade the TiO_2 layer sliding the TiO_2 paste down the glass

smoothly.

(v) Put in the oven. Ramping rate ca. 8 °C/min from room temperature to 500 °C and maintain for 30 min for sintering purposes.

(II) Sensitization

Identical to A1.2, Sensitization (II).

A2.3 Fabrication of Pt counter electrodes

(i) A multimeter was used to ensure that the FTO side of the glass was facing upwards.

(ii) Two strips of 3M magic tape were deposited at the left/right side of the FTO glass surface for masking purposes (Figure A2a), and the tapes were pressed down with a stirring rod to expunge air bubbles.

(iii) Chloroplatinic acid was deposited along the top edge on the coated side of the FTO glass. A glass pipette was used to spread the material in a downward motion on the surface. The glass was subsequently heated slowly to avoid cracking.

(iv) The FTO glass was slowly heated to (15 ºC/min) 400 ºC, where it was kept for 30 min.

(iv) The FTO glass was immersed in the dye solution overnight.

A2.4 Assembling DSSCs

(i) Thermoplastics (known as Surlyn) were cut into suitable pieces (~ 1.5 cm x 1.5 cm; inner area: 1 cm x 1 cm).

(ii) Clean plastic tweezers were used to dip the Surlyn in acetonitrile in order to improve the contact with the electrodes.

(iii) The thermoplastics were placed between the two electrodes and hot pressed (~ 120 ºC) firmly on the top.

(iv) The thermoplastics has to melt and a nitrogen gun can be used for cooling.

(v) A syringe with a sharp tip was used to inject electrolyte through the holes. Vacuum can be used to distribute the electrolyte over the entire active area.

(vi) Mix double bubble and seal the holes to avoid electrolyte evaporation.

(vii) Add silver paste (in acetone) to afford better contact;

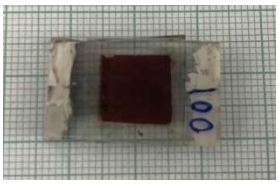

Figure A4. A sealed DSSC device.

B Calculated pK_a values in water of N3 by SMD model.

	ΔG_{solv}	Calculated pKa	Experimental pKa
N3H4	-60.94 kcal/mol	52.31	1.33
N3H3_A	-33.24 kcal/mol	58.74	2.24
N3H2_A	-35.91 kcal/mol	62.15	3.45
N3H1_B	-66.04 kcal/mol	67.30	4.20
N3H0	-133.59 kcal/mol		